Reducing Radiation Dose to the Female Breast During Conventional and Dedicated Breast Computed Tomography

Franco Rupcich
Marquette University

REDUCING RADIATION DOSE TO THE FEMALE BREAST DURING CONVENTIONAL AND DEDICATED BREAST COMPUTED TOMOGRAPHY

by

Franco John Rupcich

A Dissertation submitted to the Faculty of the Graduate School,
Marquette University,
in Partial Fulfillment of the Requirements for
the Degree of Doctor of Philosophy

Milwaukee, Wisconsin

May 2013

ABSTRACT
REDUCING RADIATION DOSE TO THE FEMALE BREAST DURING CONVENTIONAL AND DEDICATED BREAST COMPUTED TOMOGRAPHY

Franco John Rupcich

Marquette University, 2013

The purpose of this study was to quantify the effectiveness of techniques intended to reduce dose to the breast during CT coronary angiography (CTCA) scans with respect to task-based image quality, and to evaluate the effectiveness of optimal energy weighting in improving contrast-to-noise ratio (CNR), and thus the potential for reducing breast dose, during energy-resolved dedicated breast CT.

A database quantifying organ dose for several radiosensitive organs irradiated during CTCA, including the breast, was generated using Monte Carlo simulations. This database facilitates estimation of organ-specific dose deposited during CTCA protocols using arbitrary x-ray spectra or tube-current modulation schemes without the need to run Monte Carlo simulations. The database was used to estimate breast dose for simulated CT images acquired for a reference protocol and five protocols intended to reduce breast dose. For each protocol, the performance of two tasks (detection of signals with unknown locations) was compared over a range of breast dose levels using a task-based, signal-detectability metric: the estimator of the area under the exponential free-response relative operating characteristic curve, $\hat{A}_{FE}$. For large-diameter/medium-contrast signals, when maintaining equivalent $\hat{A}_{FE}$, the 80 kV partial, 80 kV, 120 kV partial, and 120 kV tube-current modulated protocols reduced breast dose by 85%, 81%, 18%, and 6%, respectively, while the shielded protocol increased breast dose by 68%. Results for the small-diameter/high-contrast signal followed similar trends, but with smaller magnitude of the percent changes in dose. The 80 kV protocols demonstrated the greatest reduction to breast dose, however, the subsequent increase in noise may be clinically unacceptable. Tube output for these protocols can be adjusted to achieve more desirable noise levels with lesser dose reduction.

The improvement in CNR of optimally projection-based and image-based weighted images relative to photon-counting was investigated for six different energy bin combinations using a bench-top energy-resolving CT system with a cadmium zinc telluride (CZT) detector. The non-ideal spectral response reduced the CNR for the projection-based weighted images, while image-based weighting improved CNR for five out of the six investigated bin combinations, despite this non-ideal response, indicating potential for image-based weighting to reduce breast dose during dedicated breast CT.

"*Sick*? ...Why haven't we fixed *sick* yet? You scientists there — put down those starfish and *help* us. I hereby demand that all the people who are good at math make the world free of illness. The rest of us will write you epic poems and staple them together into a booklet."

Daniel Handler, *Adverbs*

For my dad, who always knew I would one day graduate from law school.

ACKNOWLEDGEMENTS

Franco John Rupcich

For so many reasons, including first sparking my interest in the field of medical imaging, I must express my deepest gratitude and thanks to my advisor, Dr. Taly Gilat Schmidt, without whose patience, guidance, and, above all, willingness to spend valuable time discussing ideas, concepts, results, and questions this work would not have been possible.

For their constant consultancy along the way, especially their helpful responses to so many questions regarding Monte Carlo simulations and image quality metrics, I thank my friends and mentors at the FDA — Jake Kyprianou, Andreu Badal, and Lucretiu Popescu. I would like to thank Dr. Lars Olson and David Herzfeld for their assistance with the computing cluster and for teaching me how to do a million things at once. For providing valuable guidance, especially that which is in the form of a six-year-old binder of notes on the mathematics and statistics of computed tomography, which I referred to countless times throughout my research, I thank Dr. Anne Clough. I would also like to thank Dominic Crotty for his insight on our work involving energy-resolved CT.

Dr. Kristina Ropella has my sincere gratitude, not only for the kindness and considerateness she has constantly shown throughout my tenure as a student at Marquette, but also for a fateful lunch in Boston that would eventually lead me here.

I want to thank all of my committee members once again for taking the time to serve as my mentors.

Nothing I ever accomplish could be done without the unwavering love and support of my family and friends, to whom I want to express my heartfelt thanks for, among so many other things, making me laugh and keeping me insane. In particular, I want to thank Nana for her (constant) humbling words of wisdom — that no matter how much I know, I still *non capisco niente*. And finally, I want to thank both my mother and my father, to whom I have always and will always look up to, in more ways than one.

This work was supported in part by an appointment to the Research Participation Program at the FDA Center for Devices and Radiological Health administered by the Oak Ridge Institute for Science and Education through an interagency agreement between the United States Department of Energy and the Food and Drug Administration, Office of Women's Health. Computer simulations were performed on the Marquette University High Performance Computing Cluster, *Pére*, which was funded in part by NSF awards OCI-0923037 and CBET-0521602.

TABLE OF CONTENTS

LIST OF TABLES

LIST OF FIGURES

LIST OF ACRONYMS AND SYMBOLS

AAPM American Association of Physicists in Medicine

ALARA as low as reasonably achievable

AP anterioposterior

AUC area under the curve

AUC EFROC area under the EFROC curve

AUC LROC area under the LROC curve

AUC ROC area under the ROC curve

BEIR Biological Effects of Ionizing Radiation

CNR contrast-to-noise ratio

CNVR contrast-to-noise-variance ratio

CT computed tomography

CTCA CT coronary angiography

CTDI computed tomography dose index

CZT cadmium zinc telluride

DNA deoxyribonucleic acid

EFROC exponential free-response ROC

EM electromagnetic

EMR electromagnetic radiation

ERR excess relative risk

eV electron-volt

FDA Food and Drug Administration

FN False negative

FNF false negative fraction

FOV field-of-view

FP False positive

FPF false positive fraction

FROC free-response ROC

GPUs graphical processing units

Gy gray

HO Hotelling observer

HU Hounsfield unit

IBO optimal image-based

ICRP International Commission on Radiological Protection

ICRU International Commission on Radiological Units

IO ideal observer

IOSNR ideal observer SNR

keV kilo-electronvolt

kV kilovolt

kVp kilovolt peak

LAR lifetime attributable risk

LNT linear no-threshold

LROC localization ROC

mAs milliamp seconds

MRI magnetic resonance imaging

MTF modulation transfer function

NPS noise power spectrum

NPWMF non-prewhitening matched filter

PA posterioanterior

PBO optimal projection-based

PMMA polymethyl methacrylate

ROC relative operating characteristic

ROI region of interest

SNR signal-to-noise ratio

Sv sievert

TCM tube-current modulation

TN True negative

TNF true negative fraction

TP True positive

TPF true positive fraction

λ wavelength

ν frequency

E energy

$E_{\lambda,\mathrm{sc}}$ energy of scattered photon

$E_{\lambda,0}$ energy of incident photon

E_{e^-} energy of ejected electron

Z atomic number

E_{pe} energy of photoelectron

E_{binding} binding energy

μ linear attenuation coefficient

I_0 initial beam intensity

I attenuated beam intensity

ℓ line integral

p projection measurement

$Q_{\mathrm{D}}(k)$ probability of detecting k photons given N transmitted photons

N_0 number of incident photons

N number of transmitted photons

N_{tot} total number of photons that passed through a pixel and were detected

m mass

D absorbed dose

H equivalent dose

w_{R} radiation weighting factor

H_{E} effective dose

w_{T} tissue weighting factor

M_{dose} radiation-induced cancer mortality rate

M_{natural} natural cancer mortality rate

H_1 signal-absent hypothesis

H_2 signal-present hypothesis

$\mathbf{g}$ image data

$T(\cdot)$ discriminant function

t test statistic

t_{c} threshold value of test statistic

D_1 decision that signal-absent hypothesis is true

D_2 decision that signal-present hypothesis is true

σ standard deviation

SNR^2_{ideal} ideal observer signal-to-noise ratio

$\mathbf{\Delta s}$ noise-free, signal-only image

$\mathbf{K_n}$ noise covariance matrix

$Q_{\mathrm{O}}(\theta, E)$ table of normalized dose deposition quantifying dose to organ, O, in mGy per photon emitted from the source for each projection angle, theta, and energy level, E

μ_{en}/ρ mass energy absorption coefficient

D_{O} Dose to organ, O

$N_0(\theta)$ number of emitted photons at each projection angle

$\Phi(\theta, E)$ input x-ray spectrum at each projection angle and energy level

R_{t} radius of signal template disk

z_i scan score for the i-th pixel

$\{z_i\}$ scan image

$\{X_i\}$ set of scan scores for true signals present

$\{Y_j\}$ set of scan scores for false signals

$\hat{A}_{FE}$ estimator for area under the exponentially transformed free-response relative operating characteristic curve

$\hat{A}_L$ estimator for area under the localization relative operating characteristic curve

Ω reference image size

Ω_{T} total searched area for false signals

$w_{\mathrm{PB}}(E)$ energy-dependent optimal projection-based weight

$w_{\mathrm{IB}}(E)$ energy-dependent optimal image-based weight

$\tilde{\ell}_{\mathrm{PB}}$ projection-based weighted line-integral

$\tilde{\ell}_{\mathrm{IB}}$ image-based weighted line-integral

Chapter 1

Introduction

1.1 Motivation

Breast cancer is the most commonly diagnosed cancer among women, excluding cancers of the skin, and only lung cancer accounts for more cancer deaths [1]. The American Cancer Society estimates that in 2013 approximately 232,340 new cases of invasive breast cancer will be diagnosed among women, from which 39,620 women are expected to die [2]. While some of the major predisposing factors for breast cancer are unavoidable by nature (increasing age, dense breast composition, inherited genetic mutations, etc.), many environmental risk factors can be mitigated ("environmental" is broadly defined to encompass all factors that are not inherited through DNA, including exogenous hormones, diet, physical activity, tobacco and alcohol consumption, and exposure to various metals, industrial and consumer chemicals, and ionizing and non-ionizing forms of radiation). A recent report published by the Institute of Medicine concluded that exposure to ionizing radiation is one of the environmental factors most clearly associated with an increased risk of breast cancer incidence [3].

As of 2010, it is estimated that approximately 10% of the United States population undergoes a CT scan each year, with a total of 75 million scans being conducted, half of which are on women. Further, the number of scans performed continues to increase each year by approximately 10% [4]. While these scans can be

crucial in diagnosing disease, they can impart from ten to several hundred times the dose received during a typical chest x-ray or mammographic screening, depending on the protocol [5]. Although no large-scale epidemiological study has established specific levels of cancer risk associated with CT scans per se for adults, risk projections in general for radiation-attributable cancer incidence resulting from exposure to low levels of ionizing radiation (similar to those procured during a typical CT examination) have been estimated largely on the basis of radiation epidemiology studies of atomic bomb survivors, and to a lesser extent, populations living near nuclear accident sites and workers with occupational exposures. In particular, Tokunaga et al. report a higher incidence of breast cancer among the cohort of atomic bomb survivors [6], and the Biological Effects of Ionizing Radiation (BEIR) VII Phase 2 Report, which considers data from all of the aforementioned cohorts, further indicates that women exposed to radiation at any age suffer a higher lifetime attributable risk (LAR) of general cancer incidence and mortality than men exposed at the same age [7]. Using epidemiological risk models proposed in the BEIR VII report, Einstein et al. have estimated the LAR of general cancer incidence associated with a single CT coronary angiography (CTCA) scan to be 1 in 143 for a 20-year-old female and 1 in 284 for a 40-year-old female, with the primary contributors to the overall risk being breast and lung cancer specifically [8]. Similarly, Smith-Bindman et. al have estimated the LAR of general cancer incidence associated with a single CTCA scan to be 1 in 150 for a 20-year-old female and 1 in 270 for a 40-year-old female, again with the primary contributors to the overall risk being breast and lung cancer [9]. Further, other studies have shown increased incidence of breast cancer for women that have undergone multiple fluoroscopic examinations [10] or have been treated by radiotherapy [11].

Considering the evidence of higher breast cancer incidence following exposure to low levels of ionizing radiation, recent recommendations from the International

Commission on Radiological Protection (ICRP) have increased the tissue weighting factor of the breast such that it is now considered one of the most highly radiosensitive organs [12]. This recommendation, along with the data from the above mentioned studies, has motivated clinicians and researchers to seek methods of reducing dose to the breast during computed tomography (CT) examinations in which it is directly irradiated.

1.1.1 CT Coronary Angiography

CT coronary angiography scans accounted for approximately 12.8% of the collective dose from all CT examinations in the United States in 2006, even though they accounted for only 6.4% of all CT procedures performed [13]. Further, it was estimated in 2007 that 2.3 million CTCA exams would be performed, from which a projected 2200 women would develop cancer during their lifetime. While the breast is often directly irradiated during CTCA protocols, it is rarely an organ of primary diagnostic interest, suggesting that there is opportunity to reduce breast dose by decreasing the amount of direct radiation exposure it receives. The recent increase in the tissue weighting factor of the breast proposed by the ICRP [12], as well as the previously mentioned studies indicating higher breast cancer incidence following radiation exposure specifically during CTCA protocols, has motivated researchers to investigate and optimize new and existing methods of reducing dose to the breast during such scans.

1.1.2 Dedicated Breast CT

Because the pathological severity of breast cancer is strongly influenced by the stage of the disease, early detection is paramount in reducing morbidity and mortality. According to the American Cancer Society, mammography is the most

common and most effective form of screening [1], however, it is not without its limitations. Mammography has been associated with a high percentage of false positives, leading to an undesirably large number of patients receiving unnecessary biopsies [14]. Moreover, mammography is known to have reduced sensitivity in detecting lesions in patients with denser breast tissue, particularly those patients of younger age [15, 16]. Alternate forms of (radiation-free) screening, such as magnetic resonance imaging (MRI) and ultrasound, have demonstrated higher sensitivity [16], yet remain costly and time consuming relative to mammography. Digital breast tomosynthesis, which has recently been approved by the United States Food and Drug Administration (FDA), has demonstrated increased sensitivity and specificity as well [17, 18] and is cheaper than MRI, however, the duration of breast compression, which many patients find painful or uncomfortable, can be longer than in conventional mammographic procedures. In recent years, dedicated breast CT has received attention as a viable breast imaging modality [19–25], due to its wider accessibility (i.e., lower costs) than MRI, higher sensitivity than mammography, and lack of breast compression. One early study has demonstrated the potential for obtaining high signal-to-noise ratio (SNR) images using dedicated breast CT at dose levels comparable to those used in mammography [19]. In addition, recent advances in photon-counting detector technology have motivated some researchers to investigate the ability of methods such as energy-resolved CT [22–24] to produce high-contrast diagnostic images, which could subsequently lead to reduced breast dose during screening and/or follow-up procedures.

1.2 Problem Statement

In CT, dose and image quality are inextricably linked. If all other parameters remain constant (e.g., patient size, reconstruction method and kernel,

etc.), a decrease in dose results in an increase in image noise, and hence a decrease in image quality. Therefore, any scan technique that can be shown to improve image quality has the potential for reducing dose. As we are concerned primarily with dose to the breast, we pose the following two research questions:

1. What is the effectiveness of CTCA dose-reduction techniques in reducing breast dose without reducing image quality?
2. What is the effectiveness of optimally-weighted energy-resolved breast CT in increasing contrast-to-noise ratio (CNR), and thus reducing breast dose, compared to photon-counting breast CT?

1.3 Purpose

The purpose of this study was to investigate and evaluate the following:

1. the relative effectiveness of several dose-reduction techniques in reducing breast dose during CTCA with respect to a task-based image quality metric
2. the effectiveness of optimally-weighted energy-resolved breast CT in increasing CNR, and thus reducing breast dose

These investigations were organized into the following three specific aims.

1.3.1 Specific Aim 1: Creation of Dose Database for CT Coronary Angiography

We created a database using Monte Carlo methods that quantifies organ dose for several different radiosensitive organs irradiated during CTCA. The database facilitates the estimation of organ-specific dose (including breast) deposited during CTCA protocols that use arbitrary x-ray spectra or tube current

modulation schemes without the need to run Monte Carlo simulations. Because this database contains dose tables for organs other than the breast, it may also prove useful in CT dose related studies that are beyond the scope of this project.

1.3.2 Specific Aim 2: Objective Assessment of Image Quality for CT Protocols Intended to Reduce Dose to the Breast during CT Coronary Angiography

We simulated several CT protocols intended to reduce breast dose during CTCA, including reduced kV, partial-angle scanning, tube current modulation, and bismuth shielding, with respect to image quality, which was quantified using an objective, task-dependent metric — area under the exponential free response relative operating characteristic curve (AUC EFROC). AUC EFROC is a signal-detectability performance indicator for cases in which the image contains multiple signals at unknown locations. Breast dose for each protocol, excluding the shielded scan, was estimated using the dose database described in Section 1.3.1, while breast dose for the shielded protocol was estimated by performing a Monte Carlo simulation. For each protocol, we plotted AUC EFROC as a function of breast dose and compared the signal detectability between protocols at a given breast dose.

1.3.3 Specific Aim 3: Quantification of the Effects of Energy-weighting on the Depiction of Calcium in Energy-resolved Breast CT

The effects of optimal image and projection-based energy weighting on the CNR of calcium were investigated through experiments on a bench-top energy-resolving CT system.

Chapter 2

Background

This chapter provides the relevant background material required for understanding the motivation, principles, procedures, and technologies presented in this dissertation.

2.1 Interaction of Radiation with Matter

Radiation is energy that travels through space or matter. There are two basic types of radiation: *particulate* and *electromagnetic (EM)*. Particulate radiation refers to energy in the form of charged or uncharged particles, such as alpha particles, electrons, protons, and neutrons. EM radiation is a massless form of energy composed of oscillating electric and magnetic field components. EM radiation can be characterized by wavelength (λ), frequency (ν), and energy per photon (E), and the range of frequencies (or equivalently, wavelengths or energies) spanned is known as the EM spectrum (Figure 2.1). When the energy of particulate or EM radiation is high enough to eject an orbiting electron from an atom, it is referred to as *ionizing* radiation.

X-rays are a form of ionizing, EM radiation with frequencies ranging from approximately 3×10^{16} Hz to 3×10^{19} Hz, corresponding to energies in the range of 100 eV to 150 keV. The various ways in which x-rays interact with matter play a fundamental role in CT image formation. In addition, these interactions can lead to

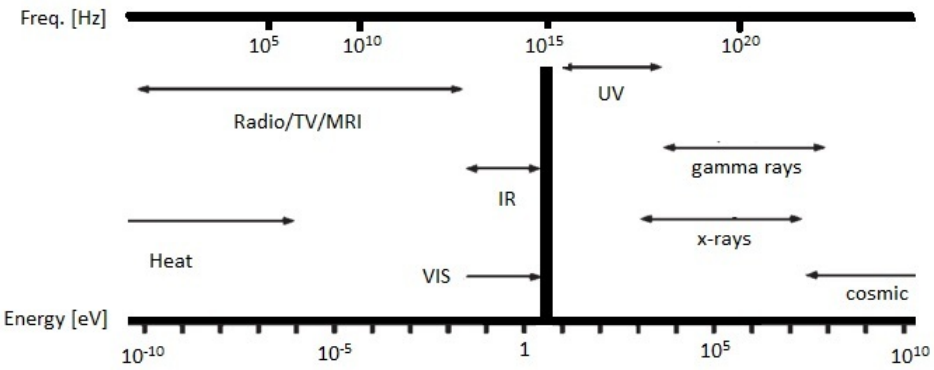

Figure 2.1: Electromagnetic spectrum. EM to the left of the black vertical line is considered non-ionizing, while that to the right is considered ionizing.

partial or complete transfer of the incident x-ray energy to kinetic energy of electrons (ionizing, particulate radiation), which in turn deposit some or all of their energy in the surrounding medium. The energy deposited by these energetic electrons is essentially what is commonly referred to as "radiation dose," or simply "dose." Radiation dose and its associated health risks will be discussed in further detail in Sec. 2.3. The remainder of this section deals with the types of interactions between particulate and x-ray radiation with matter.

2.1.1 Particle Interactions with Matter

There are several particles of ionizing radiation, including uncharged particles, such as neutrons, and charged particles, such as alpha particles, beta particles, positrons, protons, and electrons. In the context of CT, we are primarily concerned with electrons and two types of interactions they may undergo: *excitation* and *ionization*. Both interactions result in a loss of kinetic energy of the incident electron.

Excitation

Excitation refers to the transfer of some of the incident electron's energy to orbiting electrons of an atom, thereby promoting them to a higher energy level (i.e., an outer shell with a lower binding energy). A promoted electron will eventually return to its original lower energy level in a process known as *de-excitation*. When an electron moves from a higher to a lower energy level (i.e., from an outer to an inner shell), the difference in binding energies between the shells is either emitted as a photon (known as a *characteristic x-ray*) or transferred to another orbiting electron, which is subsequently ejected from the atom (known as an *Auger electron*).

Ioniziation

When the energy transferred from the incident electron exceeds the binding energy of the orbiting electron, then the orbiting electron is ejected from the atom, resulting in ionization. Ions play an important role in radiation-induced damage, as discussed in Sec. 2.3.

2.1.2 X-ray Interactions with Matter

In the energy range used in diagnostic radiology ($\approx$ 15–150 keV), there are three primary types of interactions of x-ray photons with matter: (1) Rayleigh scattering, (2) Compton scattering, and (3) photoelectric absorption.

Rayleigh Scattering

Rayleigh (or coherent) scattering occurs when the electric field of an incident photon expends energy, causing the electrons within an atom to oscillate in phase. The energy from the oscillating electron cloud is instantaneously released in the

form of an emitted photon with energy equivalent to that of the incident photon but with a slightly different (i.e., "scattered") direction (Figure 2.2). Rayleigh scattering occurs mainly with relatively low-energy photons (≈ 15–30 keV) and with a relatively low probability of occurrence (≈ 5–10%). Unlike the other types of interaction, Rayleigh scattering does not cause ionization of the atom.

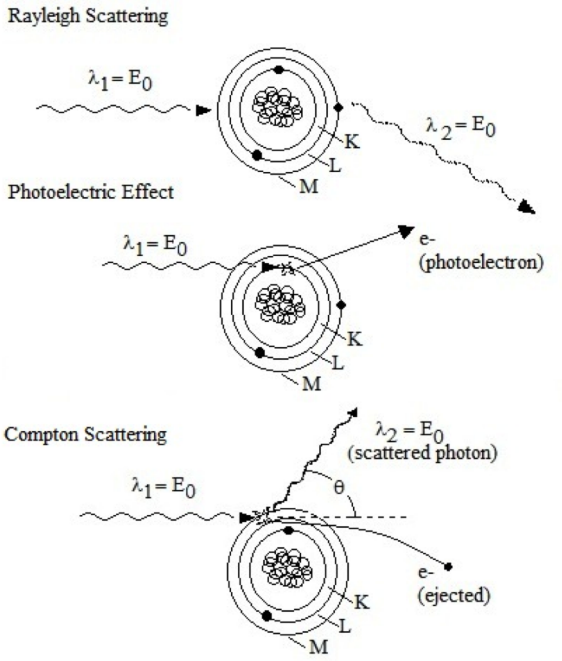

Figure 2.2: X-ray interactions with matter. E_0 is the energy of the incident photon, λ_1. λ_2 is the scattered photon, and e^- is an electron.

Compton Scattering

Compton scattering occurs when an incident photon interacts with an electron that is bound to an atom with a binding energy that is substantially less than the incident photon's energy. Thus, Compton scattering mostly occurs with outer-shell electrons, which generally have low binding energies. The electron is ejected from the atom, and the incident x-ray photon is scattered with a partial loss in energy (Figure 2.2). The energy of the scattered photon, $E_{\lambda,\mathrm{sc}}$ can be calculated

from the energy of the incident photon, $E_{\lambda,0}$, and the scattering angle, θ:

$$E_{\lambda,\mathrm{sc}} = \frac{E_{\lambda,0}}{1 + \frac{E_{\lambda,0}}{511\ \mathrm{keV}}(1 - \cos\theta)} \tag{2.1}$$

Eq. 2.1 implies that incident photons of low energy are more likely to back-scatter (θ = 90–180°), while those of high energy are more likely to forward-scatter (θ = 0–90°).

Due to the law of conservation of energy, we can calculate the energy that is transferred to the ejected electron, E_{e^-}, assuming that the binding energy is negligible:

$$E_{\mathrm{e}^-} = E_{\lambda,0} - E_{\lambda,\mathrm{sc}} \tag{2.2}$$

For the lower x-ray energies used in diagnostic imaging, most of the incident photon's energy is retained by the scattered photon, and thus only a small amount of that energy is locally absorbed (i.e., transferred into kinetic energy of a charged particle, such as the ejected electron, which in turn deposits its energy in the medium via excitation or ionization of local atoms) compared to photoelectric absorption.

Because the incident photon energy must be considerably greater than the electron's binding energy before a Compton interaction is likely to occur, the relative probability of occurrence of Compton scattering increases with increasing incident photon energy, compared to Rayleigh scatter and photoelectric absorption. In addition, the probability of occurrence of Compton scattering is proportional to electron density. However, it is nearly independent of the atomic number, Z**!**. Thus, since there is little variation in electron density within soft tissues, Compton scattering provides little contrast information between materials of biological interest. Compton scattering is the predominant interaction of x-rays with soft

tissue for energies above 26 keV.

Photoelectric Absorption

Photoelectric absorption, also known as the photoelectric effect, occurs when the energy of the incoming photon is greater than or equal to the binding energy of an orbiting electron. The photon gives up all of its incident energy (i.e., it is absorbed) to the ejected electron, which is called a *photoelectron*. The kinetic energy of the photoelectron, E_{pe}, is given by the following equation:

$$E_{\text{pe}} = E_{\lambda,0} - E_{\text{binding}} \tag{2.3}$$

where $E_{\lambda,0}$ is the energy of the incident photon, and E_{binding} is the binding energy of the electron. Photoelectric absorption is most likely to occur with an orbiting electron whose binding energy is closest to, but still less than, that of the incident photon. In other words, the effect is most likely to occur within the innermost shell whose binding energy is less than that of the incident photon. The vacancy caused by the ejection of the photoelectron from an inner shell is filled by an electron from a lower binding energy shell, which in turn is filled by an electron from an even lower binding energy shell. This process is known as an electron cascade, and it results in either the emission of characteristic x-rays or Auger electrons, as described in Sec. 2.1.1.

The probability of occurrence of photoelectric absorption is proportional to Z^3/E^3. Thus, photoelectric absorption is the predominant interaction of x-rays with low energies (below 26 keV) in materials with high Z. Further, because the probability of occurrence depends so highly on Z, the photoelectric effect can provide contrast information between tissues with only slightly different atomic numbers.

2.2 CT Physics and Image Formation

Computed tomography is a widely used medical imaging modality used for both the screening and diagnosis of several diseases. In CT, an x-ray projection is acquired at each of several thousand angles about the patient. These projections are then processed in a mathematical algorithm known as *reconstruction* to produce high-contrast, high-spatial resolution, two-dimensional slices of the internal patient anatomy or three-dimensional volume images. The following sections briefly describe the fundamental steps of CT image formation.

2.2.1 X-ray Attenuation and the Beer-Lambert Law

When a photon travels through a length of matter, there are three possible outcomes: (1) it will interact with the matter and *scatter* (via Compton or Rayleigh scattering), (2) it will interact with the matter and be *absorbed* (via photoelectric absorption), or (3) it will pass through the matter without undergoing any interaction. The first two outcomes, both of which effectively remove some or all of the incident photon's energy, are collectively referred to as *attenuation*. X-ray attenuation is the fundamental physical process underlying CT image formation.

The attenuation properties of a homogenous material can be described by that material's energy-dependent *linear attenuation coefficient*, $\mu(E)$. For a monoenergetic beam of initial intensity, I_0, traveling in a straight line of length, L, through an object composed of homogenous material with linear attenuation coefficient, $\mu(E) = \mu$ (since our beam contains only a single energy), the attenuated beam intensity, I, after passing through the object is given by a simplified form of the Beer-Lambert Law:

$$I = I_0 \, \mathrm{e}^{-\mu L} \tag{2.4}$$

We assume that both I and I_0 are known (i.e., they can be measured).

In CT, the object of interest is usually a patient and thus is composed of heterogenous material. Eliminating the homogeneity assumption above causes μ to become dependent upon the position along the line, s, and the Beer-Lambert Law becomes:

$$I = I_0 \, \mathrm{e}^{-\int_L \mu(s)\mathrm{d}s} \tag{2.5}$$

The exponent in Eq. 2.5 is known as the *line integral*, ℓ, along the line, s, and in general is defined as:

$$\ell \equiv \int_L \mu(E, s) \, \mathrm{d}s \tag{2.6}$$

Image formation via reconstruction requires the line integral at each angle (over at least 180°) about the object. We have assumed we can measure I_0 and I, thus an estimate of the line integral, also referred to as the *projection measurement*, p, can be obtained by substituting Eq. 2.6 into Eq. 2.5 and rearranging:

$$p = -\ln \frac{I}{I_0} \tag{2.7}$$

In the case in which we have assumed a monoenergetic x-ray beam, $p = \ell$. However, as will be discussed in Sec. 2.2.2, in practice x-ray beams are polyenergetic, thus:

$$I_0 = \int_E I_0(E) \, \mathrm{d}E \tag{2.8}$$

and the Beer-Lambert Law becomes:

$$I = \int_E I_0(E) \, \mathrm{e}^{-\int_L \mu(E,s)\mathrm{d}s} \, \mathrm{d}E \tag{2.9}$$

Substituting Eq. 2.8 and Eq. 2.9 into Eq. 2.7, the projection measurement assuming

a polyenergetic x-ray beam is:

$$p = -\ln\left[\frac{\int_E I_0(E)\ \mathrm{e}^{-\int_L \mu(E,s)\mathrm{d}s}\ \mathrm{d}E}{\int_E I_0(E)\ \mathrm{d}E}\right] \tag{2.10}$$

The filtered backprojection reconstruction algorithm (discussed in Sec. 2.2.3) does not take into account the energy dependence of μ, but instead relies on a single "effective" value of μ. Along a given path through the object, the lower energy photons of the polyenergetic beam will be preferentially attenuated relative to the high energy photons, resulting in the beam containing a greater proportion of high energy photons, i.e., the beam becomes "hardened." This results in an upward shift of the average x-ray energy and a corresponding downward shift in the effective value of μ along that path-length. The magnitude of the shift in μ is greater for more attenuating path-lengths, resulting in artifacts in the reconstructed image due to lower values of μ for pixels that lie along longer path-lengths or along path-lengths containing dense materials, such as bone. These artifacts are referred to as *beam hardening* artifacts, which can be reduced using correction algorithms.

2.2.2 Acquiring X-ray Projections

During CT, the object of interest is positioned between an x-ray source and detector, which are affixed to a gantry that rotates about the object. The x-ray source consists of a tube containing a cathode and an anode, usually composed of tungsten. An electric potential can be applied across the tube, causing electrons to accelerate from the cathode to the anode. When these electrons come near or directly interact with the nucleus of an atom, they lose part or all of their energy, resulting in the emission of an x-ray photon, referred to as *bremsstrahlung* radiation. The energy of the bremsstrahlung photon is determined by the proximity of the electron to the nucleus when the energy transfer occurs. Thus, the x-ray source

produces an x-ray beam that is polyenergetic (i.e., consisting of a *spectrum* of energies). The tube potential, measured in kilovolt (kV), can be used to control the quality of the beam energy, while the tube current, measured in mA, can be used to control the quantity (i.e., intensity) of the beam. The intensity is also often referred to as the tube-current time-product, which is the product of the tube-current and the duration of time during which the x-ray source is on. The tube-current time-product is measured in milliamp seconds (mAs).

The detector measures the intensity of the x-ray beam incident upon it. The projection of an object, I, is the signal measured by the detector in the presence of the object. Assuming the attenuation through air is negligible, we can estimate I_0 as the signal at the detector when no object is present. Thus, we can obtain the projection measurement, p, of the object at each angle using Eq. 2.7 with the measured projections, I and I_0.

2.2.3 Reconstruction

Once we have estimated the line integral for each angle over at least 180° about the object, a two-dimensional slice through the object can be formed via a process known as *reconstruction*. Traditionally, images have been reconstructed using an algorithm known as *filtered backprojection*, in which the projection data (line integrals) are Fourier transformed into the spatial frequency domain, high-pass filtered, inverse-transformed back to the spatial domain, and finally "backprojected" over a grid to form the image. More recently, iterative reconstruction algorithms are being investigated and used to reconstruct images, whereby maximum likelihood estimation methods are used to estimate the object that is most likely to have produced the measured data. Iterative methods incorporate models of the system and noise. Thus, while such algorithms are more computationally demanding than filtered backprojection, they have been shown to produce less noisy images.

Immediately following reconstruction, the value of a pixel at a particular location in a CT image is an estimate of the linear attenuation coefficient value, μ, at the corresponding location within the object being scanned. The pixel values are typically linearly transformed to a standardized scale, measured in *Hounsfield unit (HU)*, according to Eq. 2.11:

$$H(x,y) = \frac{\mu(x,y) - \mu_{\text{water}}}{\mu_{\text{water}}} \times 1000 \tag{2.11}$$

where $H(x,y)$ is the value of the pixel located at (x,y) in HU.

2.2.4 Image Noise and Contrast Considerations

Noise

Assuming an ideal detector, the probability, $Q_{\text{D}}(k)$, of detecting k photons after transmitting through an object is:

$$Q_{\text{D}}(k) = \frac{N^k \ \text{e}^N}{k!} \tag{2.12}$$

where N is the expected number of photons transmitted through the object, which in turn is dependent upon the number of photons incident upon the object, N_0 (as governed by the Beer-Lambert Law). $Q_{\text{D}}(k)$ is a Poisson process with rate, N. Thus, the expected number of photons detected and the variance in the number of photons detected are both N. For images reconstructed using filtered backprojection, this leads to the following proportionality [26]:

$$\sigma \propto 1/\sqrt{N_{\text{tot}}} \tag{2.13}$$

where σ is the standard deviation (noise) of the value of an image pixel, and N_{tot} is the total number of photons that passed through that pixel and were detected.

Here, the pixel value is considered to be a random variable for which we can collect many samples from which we can estimate its expected value and variance. In a CT image, the expected value of an image pixel is the actual value of the linear attenuation coefficient, μ, at that location in the object. Thus, the relationship between the signal-to-noise ratio of an image pixel and the total number of photons passing through that pixel that are detected is given by:

$$SNR \propto \frac{\mu}{1/\sqrt{N_{\text{tot}}}} \propto \sqrt{N_{\text{tot}}} \tag{2.14}$$

It is apparent that an increase in the number of detected photons leads to a decrease in image noise, or equivalently, an increase in SNR. Because dose is directly proportional to the number of photons used in a CT scan (i.e., the tube-current), the proportionalities given in Eq. 2.13 and Eq. 2.14 represent the fundamental tradeoff between dose and image quality in CT. Note that the SNR given by Eq. 2.14 is not the same as the SNR metric discussed in later sections.

Contrast

As mentioned in Sec. 2.2.1, μ is energy-dependent. In the diagnostic energy range used in CT, there is a greater difference between the μ values of two biological tissues at a lower energy than than at a higher energy (Figure 2.3). Thus, lower energies provide greater contrast between tissues in the image. However, lower energy photons are also more likely to be absorbed via photoelectric absorption, resulting in less detected photons, and thus increased image noise. While higher energy photons provide lesser contrast information, they are more likely to transmit through the object and be detected, thereby decreasing image noise. As discussed in Sec. 2.2.2, the energy spectrum of the x-ray photons incident upon the object is controlled via the tube potential. Thus, there is generally a tradeoff between image

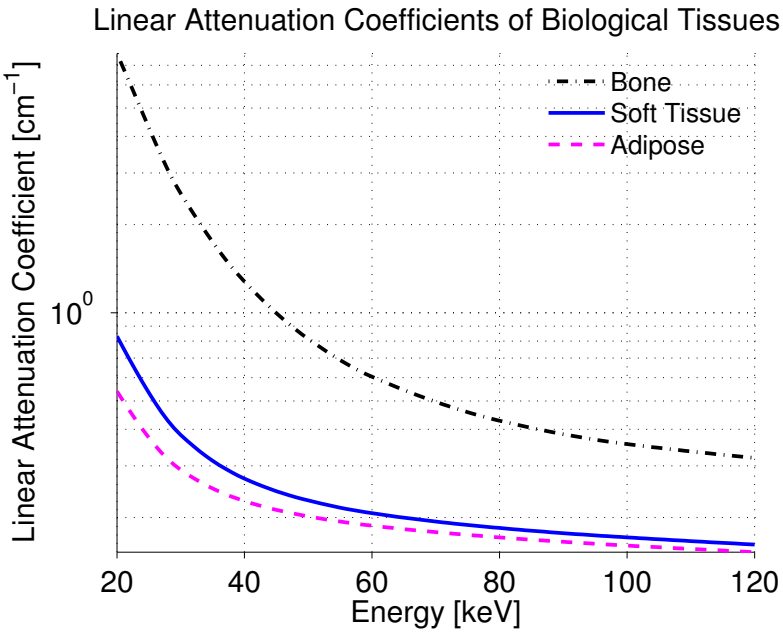

Figure 2.3: Linear attenuation coefficient values for biological tissues in the diagnostic energy range [27].

contrast and image noise with respect to the chosen kV of the scan.

2.3 Radiation Dose and Associated Health Effects and Risks

The ionizing radiation that a patient is exposed to during a CT scan (be it the x-ray photons or the electrons ejected from atoms as a result of photoelectric absorption and Compton scattering) has the potential to cause biological changes, such as deoxyribonucleic acid (DNA) strand breaks or other molecular or cellular damage. A biological change is said to be *direct* if a photon or electron directly damages a biologically important macromolecule through excitation or ionization. A biological change is said to be *indirect* if the photon or electron ionizes other (non-biologic) molecules (usually water), which results in the creation of chemically reactive species that can lead to the formation of free radicals, which in turn damage biologic macromolecules. (Most radiation-induced damage to DNA is

caused by free radicals). Barring cases of severe overexposure, only a fraction of the radiation energy deposited during a CT scan brings about biological changes, and some of the damage that does occur can be repaired. Still, the risk of adverse health effects from exposure to low levels of ionizing radiation does exist. While the risk of effects such as carcinogenesis resulting from exposure to radiation during CT procedures may be small, the fact that tens of millions of such procedures are performed each year warrants cause for concern.

2.3.1 Dose Definitions, Quantities, and Units

Before we begin our discussion of the health effects and risks of radiation dose, it is important to understand exactly what is meant by the term "dose." In fact, this term on its own can imply several different definitions, including *absorbed dose*, *equivalent dose*, or *effective dose*.

Absorbed Dose

When the term "radiation dose" or "organ dose" is used, often what is implied is *absorbed dose*. The absorbed dose, D, for a given material is the energy, E, imparted by ionizing radiation per unit mass, m, of irradiated material:

$$D = \frac{E}{m} \tag{2.15}$$

"Energy imparted" refers to the energy transferred by the incident photon to the kinetic energy of charged particles (i.e., electrons) that remain in the volume of interest. The SI unit for absorbed dose is the gray (Gy), where 1 Gy = 1 J/kg.

Equivalent Dose

Different types of ionizing radiation can lead to more severe biological damage per unit absorbed dose than others. For example, alpha particles are estimated to be 20 times more damaging per Gy than x-rays. To account for the relative severity of biologic damage produced, each type of ionizing radiation has been assigned a *radiation weighting factor*, w_{R}, by the ICRP (Table 2.1). The

Table 2.1: ICRP recommended radiation weighting factors.

Type of radiation	Radiation weighting factor, w_{R}
X-rays, gamma rays, beta particles, electrons	1
Protons	2
Neutrons (energy dependent)	2.5–20
Alpha particles	20

Source: ICRP Publication 103 *The 2007 Recommendations of the International Commission on Radiological Protection. Ann. ICRP 37 (2–4),* Elsevier, 2008.

equivalent dose, H, is the absorbed dose, D, multiplied by the radiation weighting factor, w_{R}

$$H = D\ w_{\mathrm{R}} \tag{2.16}$$

The SI unit for equivalent dose is the /acSv, where 1 sievert (Sv) = 1 J/kg. X-rays and electrons both have a w_{R} of 1, and so 1 Sv = 1 Gy in the context of CT.

Effective Dose

As will be discussed in further detail in following sections, there has been a significant amount of research devoted to investigating the biological effects of ionizing radiation. One observation has been that different biological tissues vary in sensitivity to the effects of ionizing radiation. Thus, the ICRP has also established a *tissue weighting factor*, w_{T}, for each type of tissue in the body (Table 2.2). The value of w_{T} assigned to a particular tissue is meant to reflect the proportion of the

Table 2.2: ICRP recommended tissue weighting factors.

Tissue	Tissue weighting factor, w_T	Sum of w_T values
Breast, red bone-marrow, colon, lung, stomach, remainder tissues[a]	0.12	0.72
Gonads	0.08	0.08
Bladder, esophagus, liver, thyroid	0.04	0.16
Bone surface, brain, salivary glands, skin	0.01	0.04
TOTAL		1.0

[a]Remainder tissues: adrenals, extrathoracic region, gall bladder, heart, kidneys, lymphatic nodes, muscle, oral mucosa, pancreas, prostate (♂), small intestine, spleen, thymus, uterus/cervix (♀).
Source: ICRP Publication 103 *The 2007 Recommendations of the International Commission on Radiological Protection. Ann. ICRP 37 (2–4),* Elsevier, 2008.

detriment from stochastic effects resulting from radiation-induced damage to that tissue compared to a uniform whole-body exposure. The *effective dose*, H_E is the sum of the products of the equivalent dose to each tissue, H_T, multiplied by the corresponding tissue's weighting factor, w_T:

$$H_E = \sum_T H_T \cdot w_T \tag{2.17}$$

The effective dose can be thought of as *the mean absorbed dose from a uniform whole-body irradiation that results in the same total radiation detriment as from the nonuniform, partial-body irradiation in question* [28]. Like equivalent dose, effective dose is measured in sieverts.

2.3.2 Biological Effects of Ionizing Radiation

The clinical manifestations of biological changes brought about by ionizing radiation are referred to as *biological effects* and are classified as either *deterministic* or *stochastic*. Deterministic effects are those for which the severity of the effect increases with radiation dose. For example, at very high exposures, the predominant deterministic effect is the death of cells, which results in degeneration of the exposed

tissue. Stochastic effects, on the other hand, are those for which the probability of the effect increases with radiation dose. As mentioned above, free radicals may damage DNA. If not properly repaired, the damaged DNA may mutate, potentially leading to impaired cell function, cell death, or, if the mutation occurs at a location responsible for controlling the rate of cell division, carcinogenesis. Thus, cancer formation is a stochastic effect of exposure to ionizing radiation.

2.3.3 Risk of Cancer Incidence from CT

The *risk* of radiation-induced cancer formation has recently become of particular concern in the medical imaging community due to the rapid increase in CT procedures being performed over the past several decades (the United States has gone from performing less than 5 million CT scans a year in 1980 to 75 million a year in 2010, with the number of CT scans performed each year increasing by approximately 10% [4, 29]). Most of the epidemiological data available for estimating the risk of general cancer incidence resulting from exposure to low levels of ionizing radiation, such as those typically procured during radiologic imaging procedures, comes from a large cohort (86,572 people) of atomic bomb survivors. Analysis of this data has led to two particularly important observations: (1) there is a statistically significant increase in the excess relative risk (ERR) of mortality for solid cancers among atomic bomb survivors that were exposed to doses as low as ≈125 mSv, and (2) there is a statistically significant linear relationship between dose and ERR for doses as low as ≈125 mSv. (ERR $= (M_{\text{dose}} - M_{\text{natural}})/M_{\text{natural}}$, where M_{dose} is the radiation-induced cancer mortality rate, while M_{natural} is the natural cancer mortality rate). Based on these observations, as well as other data from the cohort study, the prevailing theory regarding radiation dose and cancer incidence is that *the risk of cancer incidence from exposure to low levels of ionizing radiation increases linearly with cumulative dose, and there is no threshold dose*

below which the magnitude of the risk is zero. This model is referred to as the *linear no-threshold (LNT)* model, and is the driving motivation behind the concerted effort among clinicians, radiologists, researchers, government agencies, and manufacturers of radiologic imaging systems to reduce the radiation dose to patients as low as reasonably achievable (ALARA).

Based on the data from the atomic bomb survivors, as well as from populations living near nuclear accident sites and workers with occupational exposures, and under the assumption of the LNT model, the BEIR VII Phase 2 Report has proposed epidemiological risk models that can be used to estimate the LAR of cancer incidence for a given radiation dose, where LAR is typically given as the number of cancer cases per a given exposed population. Several studies [8, 9, 30–32] have since used the proposed risk models to estimate the LAR of cancer incidence resulting from doses received during CT exams. In general, the results of these studies suggest non-negligible LAR of cancer incidence associated with dose levels received during several types of protocols, including head and neck, chest, and abdominal CT procedures (typical organ doses for different radiological procedures are shown in Table 2.3). Additionally, data from these studies suggest that women generally show a higher LAR of cancer incidence than men. For example, Einstein et. al have reported an LAR of cancer incidence of 1 in 143 for a 20-year-old female compared to an LAR of 1 in 686 for a 20-year-old male for a CTCA protocol [8].

A recent retrospective cohort study assessing cancer risk from CT scans taken during childhood found that when cumulative doses reach 50 mGy, the risk of leukemia almost triples, and when cumulative doses reach 60 mGy, the risk of brain cancer almost triples, although the cumulative absolute risks are small (within ten years of the first scan for patients under ten years of age, one excess case of leukemia and one excess case of brain cancer per 10,000 head CT scans is estimated to occur) [32]. This is the first study to provide direct evidence of a link between

Table 2.3: Typical absorbed organ doses procured during radiologic imaging procedures.

Procedure	Organ	Organ dose [mSv]
PA chest radiography	Lung	0.01
Mammography	Breast	3.5
CT chest	Breast	21.4
CT coronary angiography	Breast	51.0
Abdominal radiography	Stomach	0.25
CT abdomen	Stomach	10.0
CT abdomen	Colon	4.0
Barium enema	Colon	15.0

PA = posterio-anterior
Source: Davies HE, et. al, *Risks of exposure to radiological imaging and how to minimise them*, BMJ, 2011

exposure to radiation from CT and cancer risk for children. However, there has yet to be a similar cohort study for adult patients. Thus, most estimates of LAR of cancer incidence from CT rely on the risk models proposed by the BEIR VII report.

Overall, evidence suggests that the LAR of cancer incidence resulting from exposure to dose during a single CT procedure is significant, albeit relatively small. However, considering (1) the growing number of scans being performed each year, and (2) the assumption that risk is proportional to the cumulative dose received coupled with the fact that many patients receive multiple scans, it has recently become a goal of the medical imaging community to minimize radiation dose, especially during CT, while maintaining diagnostic image quality. In addition, particular attention is being given toward efforts to reduce dose to the female breast due in part to (1) the relatively high amount of dose it receives during some CT procedures, such as CTCA (Table 2.3), despite it not being the organ of interest, coupled with (2) the fact that for a given radiation dose, the LAR of breast cancer incidence is among the highest of all cancer types [7].

2.4 Dose Reduction Techniques

The following sections discuss a few techniques intended to reduce dose to the breast.

2.4.1 Reduced kV

Reducing the kV during a CT acquisition eliminates from the incident x-ray beam some of the higher energy photons that are capable of depositing more energy within the patient. Due to the presence of more lower energy photons, this technique generally increases both image contrast and noise. Studies have indicated that reducing the kV has the potential of reducing dose to the breast by 27 – 50% while maintaining equivalent image quality [33, 34].

2.4.2 Bismuth Shielding

Similar to reducing the kV, bismuth shielding placed over the breast acts to filter out high energy photons before they can enter the patient. Numerous studies [33, 35–39] have indicated potential for dose savings to the breast (29 – 57%). However, a number of disadvantages associated with shielding, including its misuse in conjunction with automatic exposure control or tube-current modulation settings in place on most scanners and streak artifacts in the resulting image, has led the Board of Directors of the American Association of Physicists in Medicine (AAPM) to recently release a position statement advocating the use of alternative dose-reduction methods over bismuth shielding [40].

2.4.3 Angular Tube-current Modulation

The level of noise in a CT image is governed by the projection containing the highest level of noise. Thus, for a scan in which each projection angle receives the same number of incident photons, those with lesser attenuating path-lengths are effectively receiving "wasted" dose. Angular tube-current modulation aims to reduce tube-current during certain angles so as to optimize the dose. Almost all scanners are equipped with tube-current modulation algorithms, which have been shown [33, 35, 36, 41] to reduce dose to the breast by 10 – 64% while maintaining equivalent image quality.

2.4.4 Partial Angle Scanning

Partial angle scanning involves drastically reducing or completely turning off the tube-current during the range of angles in which the breast is directly exposed. At least one study has shown the potential for breast dose savings up to 50% [35].

2.5 Image Quality

In medical diagnostic imaging, *image quality* must express the effectiveness with which the image can be used for a specific diagnostic task (e.g., detection of a lesion or estimation of the degree of stenosis). Accordingly, the International Commission on Radiological Units (ICRU) recommends the *objective assessment of image quality*, and more specifically, the use of task-dependent metrics over task-independent metrics, as the latter may not always be directly indicative of the diagnostic performance of the intended task and thus may not fully accurately represent the true "quality" of an image [42].

The objective assessment of image quality comprises four main elements: the

diagnostic *task* (e.g., detection of an object or signal), a *description of the statistical properties of the data* (e.g., a set of images from each class from which statistical properties can be derived), the *observer* (a mathematical model or human that performs the given task), and the *figure of merit* (a scalar summary metric estimated from the output of the observer that indicates how well the observer performed the given task) [43].

The following sections discuss these four components in more detail. In addition, some commonly used task-independent metrics are discussed.

2.5.1 The Task, Observer, and Data Statistics

Many tasks in diagnostic medical imaging can be simplified to a binary decision problem, in which an observer must decide if the image belongs to one of two classes or hypotheses: H_1 and H_2, corresponding to signal absent and signal present, respectively. The signal, in this case, refers to an anatomical abnormality, e.g., a lesion or microcalcification. The observer's decision is based on the value of a test statistic, t, which is computed from the image data, $\mathbf{g}$ via a *discriminant function*, $T(\cdot)$:

$$t = T(\mathbf{g}) \tag{2.18}$$

The observer then classifies the given image under one of the two hypotheses by comparing the value of the t to a *decision threshold*, t_c:

$$t \underset{D_1}{\overset{D_2}{\gtrless}} t_c \tag{2.19}$$

where D_1 denotes the decision that H_1 is true, and D_2 denotes the decision that H_2 is true. The notation of the above inequality reads "decide hypothesis H_2 whenever the greater-than sign holds; decide hypothesis H_1 whenever the less-than sign holds." Because it is dependent on the data, t is a random variable with a

probability density function that depends on the underlying hypothesis:

$$\text{pr}(t|H_j) = \int \text{pr}(t\ |\mathbf{g})\ \text{pr}(\mathbf{g}\ |H_j)\ \text{d}g \tag{2.20}$$

where $\text{pr}(\cdot)$ is the probability density function. In Sec. 2.5.2, we will see how Eq. 2.19 and Eq. 2.20 are used in computing various measures of the task performance.

Model Observers

The discriminant function can take on many forms, both linear and non-linear. One form of the discriminant function that is of particular interest is:

$$T(\mathbf{g}) = \frac{\text{pr}(\mathbf{g}\ |H_2)}{\text{pr}(\mathbf{g}\ |H_1)} \tag{2.21}$$

This test statistic is known as the *likelihood ratio*, and it can be shown that any observer that uses the likelihood ratio as its test statistic makes optimal use of all available information in the data to achieve the highest possible performance for the given task [44]. Thus, such observers are referred to as optimal or *ideal observers*.

From Eq. 2.21, it is apparent that an ideal observer requires full knowledge of the probability distribution function of the data under both the signal-absent and signal-present hypothesis. Because this information is rarely known, simplifying assumptions about the statistics of the data are typically made. For example, if the data is assumed to be normally distributed under both hypotheses, then only the mean and variance are required, which can usually be estimated by collecting several samples of the data.

Other forms of the discriminant function lead to various other model observers, which are generally classified as either *optimal* or *suboptimal* and as either *linear* or *non-linear*. Model observers and their associated figures of merit (discussed in Sec. 2.5.2) are extremely useful tools in the objective assessment of

image quality. For example, in CT, a model observer that operates on the projection data (i.e., before reconstruction) obtained for a particular system is useful in evaluating and optimizing that system. Similarly, a model observer operating on a CT image is useful for evaluating the particular reconstruction algorithm or acquisition technique used. In addition, some observers, such as the channelized Hotelling observer, have been shown to correlate well with human observer performance for certain tasks in CT [44, 45]. Thus, model observers can be used in lieu of lengthy human observer studies.

2.5.2 Measures of Task Performance

The fourth and final component of the objective assessment of image quality is the *figure of merit*, which is a computable and scalar measure summarizing the performance of the observer for the given task. Before we begin our discussion of a few particular figures of merit, it is first important to understand the concept of the relative operating characteristic (ROC) curve.

Relative Operating Characteristic Curves

There are four possible outcomes of a binary decision problem, as shown in Table 2.4. Given knowledge of the probability density function of t under each

Table 2.4: Binary decision outcomes

1.	True positive (TP)	H_2 is true; observer decides H_2 is true (D_2)
2.	False positive (FP)	H_1 is true; observer decides H_2 is true (D_2)
3.	True negative (TN)	H_1 is true; observer decides H_1 is true (D_1)
4.	False negative (FN)	H_2 is true; observer decides H_1 is true (D_1)

hypothesis (Eq. 2.20), we can compute the *true positive fraction (TPF)* and *false*

positive fraction (FPF) for a specified decision threshold, t_c:

$$\text{TPF} = \Pr(t \geq t_c | H_2) = \int_{t_c}^{\infty} \text{pr}(t|H_2)\ \text{d}t \tag{2.22}$$

$$\text{FPF} = \Pr(t \geq t_c | H_1) = \int_{t_c}^{\infty} \text{pr}(t|H_1)\ \text{d}t \tag{2.23}$$

These fractions, as well as the true negative fraction (TNF) and false negative fraction (FNF), which can be calculated similarly, are the areas under the appropriate probability density function on t for the specified threshold, t_c, as shown in Figure 2.4.

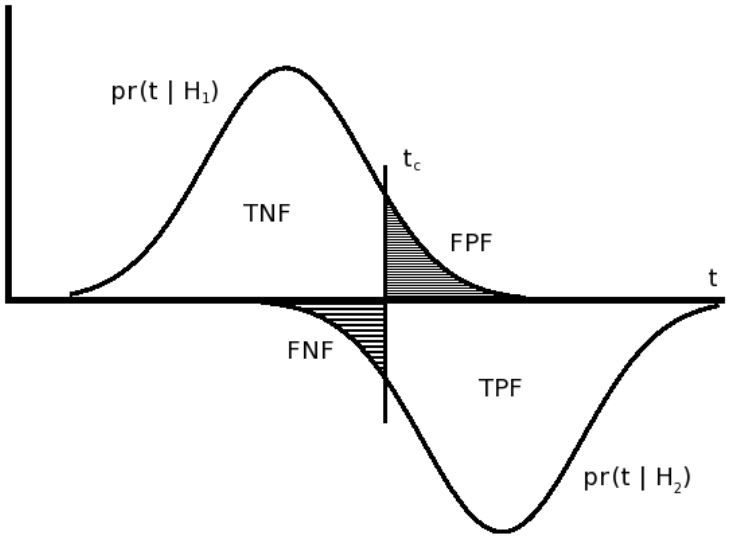

Figure 2.4: Probability density function of the test statistic under the competing hypotheses for a binary decision problem. Shown are the TPF, TNF, FPF, and FNF for a specified threshold setting, t_c.

From Eq. 2.22, Eq. 2.23, and Figure 2.4, it is apparent that the TPF and FPF depend on the decision threshold, t_c. Thus, as the threshold is varied, we obtain corresponding pairs of values for the TPF and FPF, which can be plotted in what is called an *ROC curve* (Figure 2.5). Points further down the curve (toward

the lower left) correspond to strict decision criteria, i.e., those resulting in relatively few positive decisions, while points further up the curve (toward the upper right) correspond to lax decision criteria, i.e., those resulting in a relatively high number of positive decisions. Overall, the ROC curve makes apparent the tradeoff between the sensitivity and specificity (equivalent to 1 minus the FPF) of the given image acquisition system and parameters (via the data they produce), task, and observer.

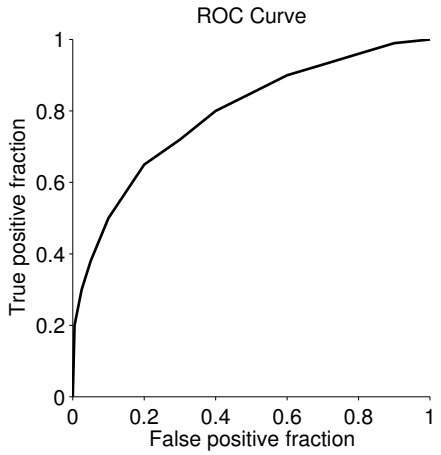

Figure 2.5: Example of an ROC curve.

The standard ROC curve is used for binary detection tasks in which the signal location is known exactly. For more complex tasks, alternative forms of the ROC curve exist. For example, the *localization ROC (LROC)* curve is used for detection tasks in which the signal location is unknown. The LROC curve plots the fraction of positive images in which the signal is correctly localized versus the false positive fraction (Figure 2.6a). In cases in which there are multiple signals, the *free-response ROC (FROC)* curve is used, which plots the fraction of signals correctly detected and localized versus the average number of false positives detected per image (Figure 2.6b).

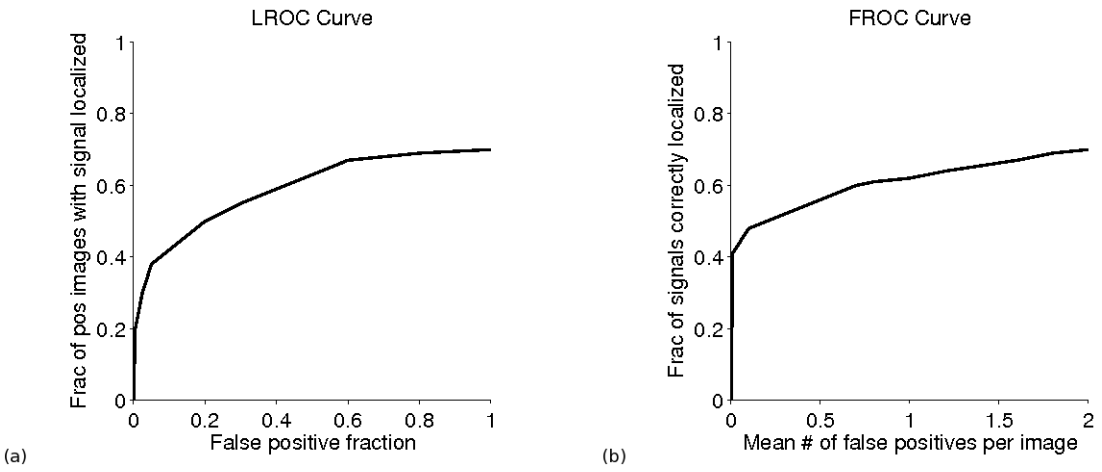

Figure 2.6: Example of (a) LROC and (b) FROC curves.

Figures of Merit

The ROC curve gives information about the performance of an observer for a particular task and system over a wide range of operating points (decision thresholds). *Figures of merit* are measures aimed at summarizing the observer's task-performance, thereby providing a more practical means of comparing the performance between different observers, systems, image-acquisition techniques, etc.

The degree of overlap of the probability density functions of the test statistic under the competing hypotheses (signal-present and signal-absent) determines the separability of the hypotheses. In other words, this overlap determines the detectability of the signal [44]. Two particular figures of merit, SNR_t and the area under the ROC curve (AUC ROC), are measures of this overlap, and hence are considered signal-detectability metrics.

Model Observer Signal-to-noise Ratios

SNR is one of the most often used figures of merit. The SNR associated with the test statistic, t, is:

$$\mathrm{SNR}_t = \frac{\langle t \rangle_2 - \langle t \rangle_1}{\sqrt{\frac{1}{2}\sigma_1^2 + \frac{1}{2}\sigma_2^2}} \tag{2.24}$$

where $\langle t \rangle_2$ and σ_2^2 denote the expected value and variance of the test statistic under the signal-present hypothesis, and $\langle t \rangle_1$ and σ_1^2 denote the expected value and variance of the test statistic under the signal-absent hypothesis. If the variance of the distribution of t is the same under each hypothesis, then Eq. 2.24 can be simplified to:

$$\mathrm{SNR}_t = \frac{\langle t \rangle_2 - \langle t \rangle_1}{\sigma} \tag{2.25}$$

An important note about SNR_t is that it may not be a useful figure of merit when the test statistic is not normally distributed under both hypotheses, since then the variance may not be an accurate measure of the spread of the distributions. However, Zeng et. al have shown that, due to the central limit theorem, this is a reasonable assumption for regions-of-interest (ROIs) in a CT image [46].

As an example of how SNR_t is used, let us return to the ideal observer in the particular case for which the signal location is known exactly. Assuming that the data is normally distributed under both hypotheses results in the ideal observer test statistic being normally distributed under both hypotheses as well, and so Eq. 2.24 can be confidently used to determine SNR_t. This SNR is given a special name, the *ideal observer SNR (IOSNR)*, and is given by:

$$SNR^2_{\text{ideal}} = \mathbf{\Delta s^T K_n^{-1} \Delta s} \tag{2.26}$$

where $\mathbf{K_n}$ is the noise covariance matrix, and $\mathbf{\Delta s}$ is the mean (i.e., noise-free) signal-only image.

If we assume the *noise is uncorrelated*, then the noise covariance matrix is

diagonal, and Eq. 2.26 can be simplified to:

$$SNR^2_{ideal} = \sum_{m=1}^{M} \frac{\mathbf{\Delta s}_m^2}{\sigma_m^2} \tag{2.27}$$

where M is the number of pixels in the image.

If we further assume the *noise is stationary*, then $\sigma_m = \sigma$ for all m, and the IOSNR further simplifies to:

$$SNR^2_{ideal} = \frac{||\mathbf{\Delta s}||^2}{\sigma^2} \tag{2.28}$$

Noise in CT images is neither stationary, nor uncorrelated. The degree of non-stationarity in the noise of CT images as well as the effects that both of these assumptions have on the performance of the observer are ongoing subjects of investigation [46–50]. Nonetheless, Eq. 2.28, for which both of these assumptions are implicit, is often used in estimating SNR.

Area under the ROC curve

The AUC ROC is defined as:

$$\text{AUC ROC} = \int_0^1 \text{TPF(FPF)}\ d\text{FPF} \tag{2.29}$$

Because the TPF and FPF both range from 0 to 1, so does the AUC ROC. In general, higher values of AUC ROC indicate a higher average level of performance with respect to the given signal-detectability task.

When the test statistic is normally distributed under both hypotheses, the

AUC ROC can be derived from SNR_t:

$$\text{AUC ROC} = \frac{1}{2} + \frac{1}{2}\,\text{erf}\left(\frac{\text{SNR}_t}{2}\right) \tag{2.30}$$

where erf$(\cdot)$ is the error function. This is often how the AUC ROC is estimated in image quality studies. Analogous area under the curve (AUC) metrics exist for other types of ROC curves. We use one such metric, the area under the free-response exponential ROC curve (AUC EFROC), for investigating task-based image quality of CT dose-reduction techniques. AUC EFROC will be discussed in more detail in Chapter 4.

2.5.3 Commonly Used Task-independent Metrics

While it is recommended to use objective, task-based metrics when assessing image quality, there are a number of commonly used task-independent metrics used as well. While they may not provide a measure of performance for the specific task, the information they do offer can still prove useful. Image *noise* and *CNR* are two such metrics.

Noise

Image noise is most often quantified as the standard deviation in a homogenous background ROI. Noise quantified in this fashion ignores the spatial correlations of the data. The noise power spectrum (NPS) quantifies the magnitude of the noise at each spatial frequency, thus providing information about the spatial correlations in the image. However, the NPS implicitly assumes stationarity of the data, and thus may be an inaccurate measure in CT [47, 48]. The noise covariance matrix quantifies the noise covariance between all pixels and makes no assumptions

about the data. Thus, it provides the most accurate and complete information regarding the magnitude of the noise and its spatial correlations.

Contrast-to-noise Ratio

CNR in an image is:

$$\mathrm{CNR} = \frac{|\mu_{\mathrm{s}} - \mu_{\mathrm{bg}}|}{\sigma} \tag{2.31}$$

where μ_c is the mean of an ROI within the signal or contrast element, and μ_{bg} and σ are the mean and standard deviation of a background ROI. Whereas the SNR operates on an image or ROI in which the signal is fully contained, the CNR only considers an ROI within the signal itself. Thus, the CNR is not dependent on the task.

2.6 Energy-resolved CT

Conventional CT detectors are solid-state scintillators. Scintillating detectors operate by absorbing incoming x-rays and converting them to visible light photons, which are in turn converted to current flow, amplified, and digitized via photo-multiplier tubes and electronic circuits. While scintillating detectors have high detection efficiency, they exhibit poor energy resolution, meaning they are unable to determine the energy of an incident photon with good accuracy. Further, while they are able to count individual photons (*pulse mode*), the very high flux rates experienced by detectors in CT necessitates *current mode* operation. Thus, during CT, scintillating detectors operate by integrating the incoming charges and disregarding the charge amplitudes, which are proportional to the incident photons' individual energies. Scintillating detectors operating in this manner are often

referred to as *charge-integrating detectors*.

Photon-counting detectors are capable of counting the individual photons incident upon them. Recent advancements in solid-state semiconductor technology have led to development of state-of-the-art *energy-resolving* photon-counting detectors, which are additionally able to determine the energy of each incident photon.

Because the contrast between biological tissues is generally greater at lower energies, an ideal detector is one that would assign more weight to lower-energy photons. Thus, conventional energy-integrating detectors, which assign more weight to higher-energy photons, and non-energy-resolving photon-counting detectors, which assign equal weights to all photons, are sub-optimal. Energy-resolving CT detectors, on the other hand, are capable of sorting photons into discrete energy bins based on specified energy thresholds. This additional spectral information can then be used to produce optimally energy-weighted images. While photon count-rate limitations generally restrict their use during conventional CT protocols, energy-resolving detectors may be practical for protocols requiring lower flux rates, such as dedicated breast CT.

2.7 Dedicated Breast CT

In recent years, dedicated breast CT has received attention as a viable screening modality, due to its wider accessibility (i.e., lower costs) than MRI, higher sensitivity than mammography, and lack of breast compression. During dedicated breast CT, the patient lies prone on a table containing a hole through which the pendant breast is placed. The x-ray source and detector, located beneath the table, rotate to collect projections through the breast for which images may then be reconstructed. Because the breast is the only object through which the x-ray

photons are transmitted, lower tube-currents compared to conventional CT may be used. Thus, energy-resolving detectors, which generally have low count-rates, may be well suited for this application.

2.8 Monte Carlo Radiation Transport Simulations

Monte Carlo algorithms use random sampling methods to obtain numerical results for a given application. In the field of medical physics, they are often used to simulate the transport of photons or energetic particles through matter by modeling the underlying physical interaction mechanisms (Compton and Rayleigh scattering, photoelectric absorption, etc.), which are stochastic processes by nature. Throughout the simulation, user-specified *tallies* are updated periodically, ultimately resulting in an estimate of one or more useful physical quantities (e.g., the energy deposited in a specified material) based on a set of input parameters. Because Monte Carlo algorithms rely on statistical methods, the variance of the estimated physical quantity is dependent upon the number of simulated events. Achieving a sufficiently low statistical uncertainty in estimates for radiation transport simulations often requires simulating the numerous interactions undergone by hundreds of millions of individual particles, which can take hours to days and even up to weeks to complete, depending on the computing resources available. Thus, while useful, Monte Carlo algorithms can also be computationally demanding, often requiring graphical processing units (GPUs) or high-performance computing clusters to be able to run quickly and efficiently.

Chapter 3

Database for Estimating Organ Dose for Coronary Angiography and Brain Perfusion CT Scans

3.1 Introduction

Several groups have evaluated methods of reducing dose to radiosensitive organs such as the breast, including reduced kV and tube-current modulated scans [33, 35, 41, 51, 52]. In addition to developing new protocols for dose reduction, studies are also required to optimize dual-kV protocols, which involve two kV settings, novel filtration materials, tube current modulation, and angular kV switching methods. Many of these studies rely on organ dose data obtained from experimental measurements or Monte Carlo simulations. Because each proposed scan protocol may include unique scan parameters (kV, mAs, etc.), a separate measurement or Monte Carlo simulation is required for each dose reduction scheme, which can be both costly and time-consuming. Monte Carlo simulations generally require computing resources that may not always be readily available and can take an extensive amount of time to complete depending on the scan protocol, phantom resolution, and statistical uncertainty required.

One commonly used dosimetry software tool, ImPACT's CTDosimetry Calculator [53], enables scanner-specific organ dose estimation. However, the tool

cannot estimate organ dose for scan protocols involving angular tube current modulation, partial angular scanning, or arbitrary spectra. This study developed a database for estimating organ dose for a single-rotation axial coronary angiography or brain perfusion CT scan with any spectral shape and angular tube-current/voltage modulation settings. The proposed database quantifies dose to a number of radiosensitive organs as a function of both projection angle and incident photon energy so that novel acquisition methods can be investigated. The database was created using tens of thousands of Monte Carlo simulations requiring high-performance computing resources and several weeks of running time. Users of the database are able to take advantage of the pre-calculated data to estimate organ dose for both existing and novel acquisition techniques without requiring Monte Carlo simulations. The database includes tables quantifying $CTDI_{vol}$ in head and body computed tomography dose index (CTDI) phantoms in order to provide approximate conversion factors to reflect the tube output of conventional CT scanners. Overall, the proposed database is intended to facilitate the development of dose reduction methods and optimized single and multiple kV acquisitions, especially for researchers without the resources required to perform Monte Carlo simulations.

3.2 Materials and Methods

3.2.1 Overview

Monte Carlo simulations were performed to obtain organ dose estimates for several energy levels and projection angles through anthropomorphic chest and thorax and CTDI head and body phantoms. The dose data was then organized into a set of dose deposition tables, which quantify the organ dose per photon emitted from the source. Finally, we present examples demonstrating how to use the tables

to estimate the percent change in organ dose between protocols.

3.2.2 Monte Carlo Software

Monte Carlo simulations in this study were performed with the penImaging software package [54–56], which relies on the previously validated PENELOPE Monte Carlo radiation transport routines [57].

3.2.3 Phantoms

Five separate phantoms were used in this study: (1) anthropomorphic chest, (2) anthropomorphic head, (3) anthropomorphic head tilted 30° about the coronal plane, (4) CTDI body, and (5) CTDI head.

Anthropomorphic Chest and Head Phantoms

This study used the 0.5 mm voxelized anthropomorphic female phantom, Ella, from the Virtual Family [58], representing an average-sized 26 year old (height: 1.63 m, weight: 58.7 kg). To relax computational memory requirements, we cropped the phantom for the head and chest simulations. For the chest simulation, the phantom was cropped to the thorax, measuring 31 cm by 22 cm in the lateral and anteroposterior directions, respectively, and 30 cm in the axial direction. For the non-tilted head simulation, the phantom was cropped to the head, measuring 18 cm by 23 cm in the lateral and anteroposterior directions, respectively, and 25 cm in the axial direction. For the tilted head simulation, the cropped head phantom was tilted 30° about the coronal plane, as if the patient were to tuck their chin toward their chest. Topograms of the whole body and cropped phantoms are shown in Figure 3.1. To assure that the axial lengths of the cropped phantoms were sufficient to capture most scattered radiation dose, we compared organ doses between the

cropped phantoms and the full phantom for a single simulated projection. Relative to the organ doses calculated when simulating the full phantom, the cropped phantoms capture 94% of the dose for bone and muscle, and 99% of the dose for all other organs.

The breast was modeled as two separate parts: an internal glandular mass and an external 1 cm thick surrounding layer of adipose. Thus, voxels representing the internal glandular mass were modeled as 100% glandular tissue, while the surrounding layer of voxels were modeled as 100% adipose. As such, "dose to breast" in the context of this study refers to dose to the 100% glandular material. Voxels representing the following organs/tissues were modeled according to their respective atomic compositions and densities as given by ICRP publication 110 [59]: fat (adipose), glandular tissue, adrenals, blood, cartilage, esophagus, eye lens, stomach, heart, kidney, liver, muscle, pancreas, skin, spleen, teeth, thyroid, and soft tissue. Voxels representing the following organs/tissues were modeled according to their respective atomic compositions and densities as given by Woodard & White [60]: lung (blood filled, 50% inflated, 50% deflated, density: 0.655 g/cm^3), cerebrospinal fluid, connective tissue. The brain was divided into three organs with slightly different atomic compositions and densities: "brain (grey matter)" including grey matter, the hippocampus and the thalamus were modeled as grey matter according to the composition given by Woodard & White [60]; "brain (white matter)" including white matter, the commissura anterior, and the commissura posterior were modeled as white matter according to the composition given by Woodard & White [60]; and "brain (mean grey/white matter)" including the cerebellum, medulla, midbrain, and pons were modeled as a 50/50 mixture of grey and white matter as defined in ICRP Publication 110 [59]. The diaphragm, larynx, and tongue were modeled as muscle. All skeletal voxels were modeled as homogenous bone (density: 1.4 g/cm^3) as given by Cristy & Eckerman [61]. This study quantified dose

only in the organs listed in Table 3.1. Most of these organs were fully included in the cropped phantoms except those listed in Table 3.2, which gives the ratio of the organ mass in the cropped phantoms to the organ mass in the full phantom.

Table 3.1: Dose deposition tables. Shown are the dose deposition tables generated for each of the five phantoms.

Phantom	Dose Tables Generated
Chest	lung breast esophagus heart bone red marrow skin muscle
Head	brain (grey matter) brain (white matter) brain (mean grey/white matter) eye lens
Head (30° tilt)	bone red marrow skin muscle
CTDI body	$CTDI_{vol}$
CTDI head	

Table 3.2: Fractional organ masses. Shown are the fractional organ masses (ratio of organ mass in cropped phantom to full phantom). Those organs not listed in the table have a fractional mass of 1.0 (i.e., they are completely included in the cropped phantoms).

Phantom	Organ	Fractional Mass
Chest	esophagus	0.92
	bone	0.18
	red marrow	0.16
	skin	0.17
	muscle	0.18
Head	bone	0.19
	red marrow	0.09
Head (30° tilt)	skin	0.09
	muscle	0.04

CTDI Body and Head Phantoms

A 32-cm-diameter virtual CTDI body phantom [62] was created using simple cylindrical and planar mathematical quadrics. The five holes in which the ion chambers are placed were 100 mm long and 12.4 mm in diameter and located at the phantom center and at the 12 o'clock, 3 o'clock, 6 o'clock and 9 o'clock positions, 1 cm interior from the surface of the phantom. The phantom was made of polymethyl methacrylate (PMMA) material (density: 1.19 g/cm^3). Each of the five ion chamber holes was also modeled as PMMA material (i.e., as if PMMA filled the holes). Dose-to-PMMA was converted to dose-to-air in order to calculate CTDI_{vol}, which is explained in Sec. 3.2.6. A virtual CTDI head phantom [62] measuring 16 cm in diameter was similarly created. Both CTDI phantoms were 15 cm in height.

3.2.4 Simulation Geometry

The source-to-detector distance for each simulation was 100 cm, with a source-to-isocenter distance of 50 cm. We modeled a single-rotation stationary cone-beam system with no table translation and a beam width at isocenter of 8 cm, which was chosen to represent the volume scanning capabilities of 320 detector row CT scanners during brain perfusion and coronary angiography scans [63, 64]. We modeled a point source with a fan angle of 53.13°, which was wide enough to cover the entire width of each phantom.

3.2.5 Energy Deposition Simulations

The transport of monoenergetic photons through each of the five phantoms was simulated between 5 and 150 keV in 1 keV increments for 1000 projections in 0.36 degree increments. Monoenergetic simulations were performed for two reasons: (1) so that results may be used to investigate the effects of specific incident photon

energy levels on organ dose, and (2) so that organ dose may be calculated for any polyenergetic spectral shape, as will be explained in detail in Sec. 3.2.7. For each photon energy at each projection angle, 10^7 photons emitted from the source within the collimated beam (henceforth referred to simply as "emitted photons") were tracked through the anthropomorphic and CTDI phantoms, and the energy deposited in each organ or material of interest for each phantom was tallied. A bowtie filter corresponding to that used for head protocols of a Toshiba Aquilion 64 scanner [65], and a bowtie filter corresponding to that used for body protocols of a Siemens AS+ scanner [66] were modeled by calculating the fan-angle dependent transmission spectra at each incident photon energy for the same materials and thicknesses representative of the physical bowtie attenuation characteristics described in Abboud et al. [65] and McKenney et al. [66]. These head and body bowtie spectra were then used for the radiation-transport simulations respective of the head and chest phantoms of this study (Sec. 3.2.3).

3.2.6 Organ Dose Tables

A table of normalized dose deposition, $Q_{\mathrm{O}}(\theta, E)$, quantifying the dose to organ, O, per emitted photon (mGy/emitted photon) for each incident photon energy, E, and projection angle, θ, was generated for the organs of the phantoms listed in Table 3.1. Figure 3.1 shows the scan field-of-view (FOV) for the simulations of the anthropomorphic chest and head phantoms. The following three subsections describe how the tables were generated.

Non-skeletal Dosimetry

For each organ of interest except the bone and red bone marrow (explained separately in Sec. 3.2.6), the energy deposited (reported in eV per emitted photon),

was converted to dose by converting eV to Joules and dividing by the mass of the organ in the respective cropped phantom. These calculations resulted in tables of normalized dose deposition, $Q_{\mathrm{O}}(\theta, E)$, quantifying the dose to organ, O, per emitted photon (mGy/emitted photon) for each incident photon energy, E, and projection angle, θ.

Skeletal Dosimetry

Due to the difficulty in accurately modeling the anatomical microstructure of trabecular spongiosa, doses to the radiosensitive red marrow cells and bone surface cells contained within the skeletal tissue are often approximated using one of several widely accepted techniques [67]. We approximated dose to bone as dose to the homogenous bone material described in Sec. 3.2.3, using the same method of converting from energy deposited to dose as described in Sec. 3.2.6, and using the mass of bone in the respective cropped phantoms. These calculations resulted in a table of normalized dose deposition for homogenous bone, $Q_{\mathrm{HB}}(\theta, E)$.

We used Eq. 3.1, originally proposed by Rosenstein [68] and employed by Turner et al. [69], to estimate the dose to red bone marrow from the dose to homogenous bone:

$$D_{\mathrm{RBM}} = D_{\mathrm{HB}} \cdot \frac{(\mu_{\mathrm{en}}/\rho)_{\mathrm{RBM}}}{(\mu_{\mathrm{en}}/\rho)_{\mathrm{HB}}} \tag{3.1}$$

where D_{RBM} and D_{HB} are the doses to red bone marrow and homogenous bone, respectively, and $(\mu_{\mathrm{en}}/\rho)_{\mathrm{RBM}}$ and $(\mu_{\mathrm{en}}/\rho)_{\mathrm{HB}}$ are the mass energy absorption coefficients of red bone marrow and homogenous bone. We created the table of normalized dose deposition for red bone marrow by using Eq. 3.1 and the table of normalized dose deposition for homogenous bone. To calculate the table of normalized dose deposition for homogenous bone for each phantom, we divided the

energy deposited by the mass of the homogenous bone in the cropped phantoms. The mass energy absorption coefficients of both materials were calculated using Eq. 3.2:

$$(\mu_{\text{en}}/\rho)_{\text{material}} = \sum_i w_i \cdot (\mu_{\text{en}}/\rho)_i \tag{3.2}$$

where w_i is the percent composition by mass and $(\mu_{\text{en}}/\rho)_i$ the mass energy absorption coefficient of the ith element comprising the material. Elemental percent compositions for red bone marrow were taken from Woodard & White [60], while those for homogenous bone were taken from Cristy & Eckerman [61]. Elemental mass energy absorption coefficients were obtained from tables published by Hubbell & Seltzer [27].

$CTDI_{\text{vol}}$ Tables

We also created tables quantifying the CTDI_{vol} in mGy per emitted photon for both the head and body CTDI phantoms. First, the CTDI_{100} at each incident photon energy for both the center and peripheral chambers of the CTDI phantoms were obtained using Eq. 3.3:

$$CTDI_{\text{x,100}} = \frac{E_{\text{x}} \cdot e \cdot L}{m \cdot N \cdot T} \cdot 1000 \cdot \frac{(\mu_{en}/\rho)_{\text{AIR}}}{(\mu_{\text{en}}/\rho)_{\text{PMMA}}} \tag{3.3}$$

where $\text{CTDI}_{\text{x,100}}$ is the CTDI_{100} at the center ($\text{CTDI}_{\text{c,100}}$) or periphery ($\text{CTDI}_{\text{p,100}}$) chamber of the CTDI phantom, E_{x} is the total energy deposited in the center or peripheral chamber (eV/emitted photon), e is the electron charge constant (conversion factor from eV to Joules), L is the active length of the chamber (10 cm), N is the number of slices, T is the tomographic section thickness, ($N \cdot T$ is the nominal beam width [8 cm]), m is the mass of PMMA in the chamber, the factor of 1000 is used to convert from Gy to mGy, and $(\mu_{\text{en}}/\rho)_{\text{AIR}}$ and $(\mu_{\text{en}}/\rho)_{\text{PMMA}}$ are the

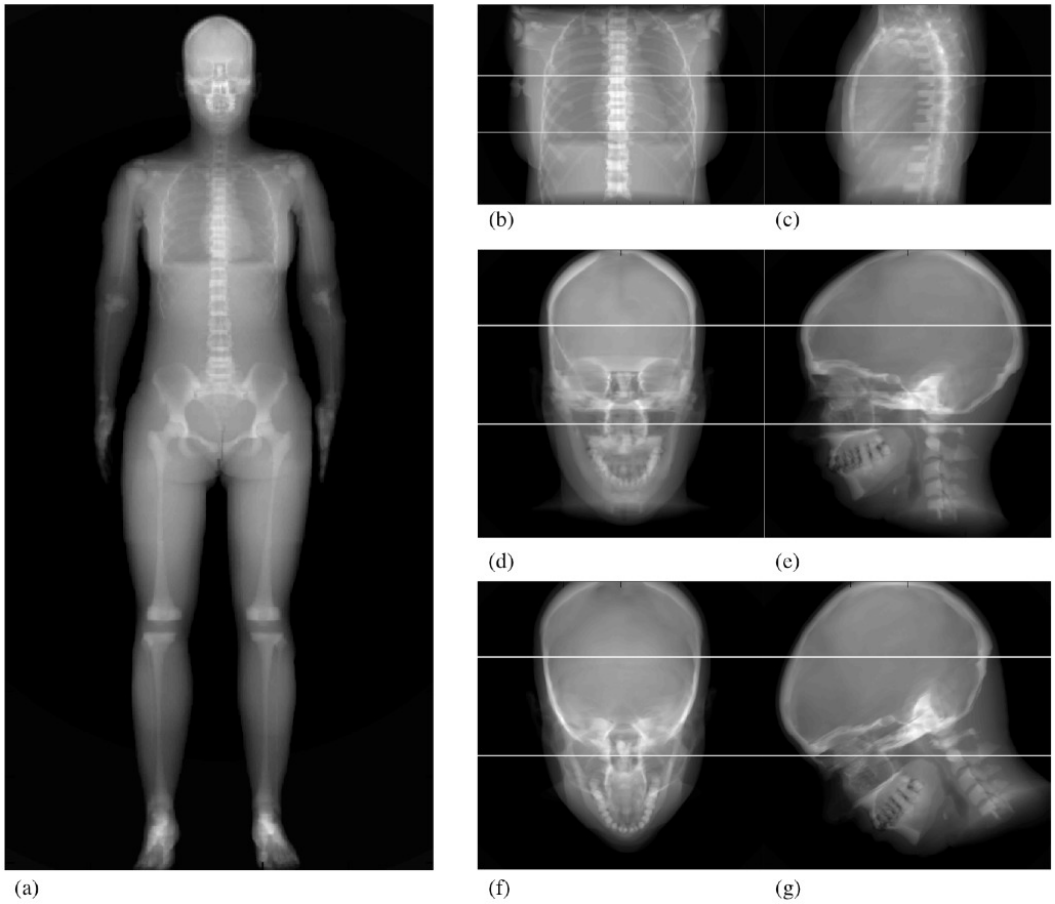

Figure 3.1: Topograms of female phantom. Topogram of the whole- body (non-cropped) female phantom (a). Anterioposterior and lateral topograms of the cropped chest phantom, (b) and (c); non-tilted head phantom, (d) and (e); and the tilted head phantom, (f) and (g). The scan field of view for each of the cropped phantoms is represented by the space between the white horizontal lines and corresponds to a coronary angiography scan for (b) and (c) and a brain perfusion scan for (d)-(g).

mass energy absorption coefficients for air and PMMA, respectively. Multiplying by the ratio of the mass energy absorption coefficients converts dose-to-PMMA to dose-to-air. The method of modeling the ion chambers as PMMA and converting to dose-to-air has been previously validated [70]. Mass energy absorption coefficient values for air and PMMA were obtained from Hubbell & Seltzer [27].

$CTDI_w$ was then calculated using Eq. 3.4 [71]:

$$CTDI_{\mathrm{w}} = 1/3 \cdot CTDI_{\mathrm{c,100}} + 2/3 \cdot CTDI_{\mathrm{p,100}} \tag{3.4}$$

Because $\mathrm{CTDI_{vol}}$ is equal to $\mathrm{CTDI_w}$ divided by the pitch, and since we used a pitch of one, our $\mathrm{CTDI_{vol}}$ is equivalent to $\mathrm{CTDI_w}$.

3.2.7 Using the Database to Estimate Dose

The total dose to an organ, D_{O}, for a scan can be calculated using Eq. 3.5.

$$D_{\mathrm{O}} = \sum_{\theta} N_0(\theta) \sum_{E} \Phi(\theta, E) Q_{\mathrm{O}}(\theta, E) \tag{3.5}$$

where $N_0(\theta)$ is the number of emitted photons at projection angle, θ; $\Phi(\theta, E)$ is the fraction of photons incident at projection angle, θ, with energy, E (i.e., the spectral distribution at projection angle, θ); and $Q_{\mathrm{O}}(\theta, E)$ is the table of normalized dose deposition (i.e., dose to organ, O, per emitted photon at angle, θ, and energy, E, as described in Sec. 3.2.6). As seen in Eq. 3.5, the total organ dose is a linear combination of the values in the table of normalized dose deposition for that organ with the weights dependent on the spectrum and number of emitted photons at each projection angle.

The table of normalized dose deposition, $Q_{\mathrm{O}}(\theta, E)$, for each organ is the output of the presented Monte Carlo simulations for the specific CT geometry we have described, while $N_0(\theta)$ and $\Phi(\theta, E)$ are user-modifiable parameters. Together, $N_0(\theta)$ and $\Phi(\theta, E)$ represent an input x-ray spectrum. Modifying these two parameters allows for calculating total organ dose for various acquisition methods, filtration schemes, and scan parameters. For example, tube voltage settings and spectra filtration can be changed by properly modifying $\Phi(\theta, E)$. While our method does not allow a user to directly specify an mAs value when calculating organ dose, a relative change in mAs by a certain factor between protocols is represented by the same relative change in $N_0(\theta)$ in Eq. 3.5, since the number of incident photons is proportional to the tube-current time-product. In this manner, $N_0(\theta)$ can be

modified across rotation angle, θ, to model angular tube current modulation. As described in Sec. 3.2.9, the database includes information about the phantoms' attenuation as a function of angle and energy to facilitate calculation of tube current modulation settings, as will be performed in Sec. 3.2.10. In addition, setting $N_0(\theta)$ to zero at desired angles represents partial-angle scanning. Angularly interlaced dual-kV protocols can be modeled by changing $N_0(\theta)$ and $\Phi(\theta, E)$ at alternating angles.

While Eq. 3.5 gives an organ dose in units of mGy, this estimate depends on the selected $N_0(\theta)$ and is not indicative of organ dose from a specific scanner. Thus, Eq. 3.5 can be used to compare the change in organ doses between protocols, which depends on the change in $N_0(\theta)$ across protocols rather than the specific value of $N_0(\theta)$. Secs. 3.2.10 and 3.2.11 demonstrate examples of using the database for studying changes in dose between protocols.

If the mAs-to-photon-fluence conversion factor for a specific scanner is known or measured, a realistic $N_0(\theta)$ could be determined and used with the database to obtain a dose estimate that reflects typical tube output. For example, the IPEM Report 78 software provides an estimate of these conversion factors [72]. Another approach for obtaining dose estimates for a specific scanner's output is to calculate a scaling factor using $\mathrm{CTDI_{vol}}$ normalization, as described in Eq. 3.6:

$$D_{\text{scanner}} = D_{\text{database}} \cdot \frac{CTDI_{\text{vol,scanner}}}{CTDI_{\text{vol,database}}} \tag{3.6}$$

where D_{database} and $CTDI_{\text{vol,database}}$ are the organ dose and $\mathrm{CTDI_{vol}}$, respectively, calculated using the dose tables. $CTDI_{\text{vol,scanner}}$ is the $\mathrm{CTDI_{vol}}$ measured on the scanner of interest using the same spectrum, $\Phi(\theta, E)$, as that used from the dose table estimations. This scaling factor adjusts for differences in scanner output and has been previously validated by Turner et al. for fully irradiated organs in abdominal scans with constant tube current [69, 73]. Our database, however,

presents organ dose data for coronary angiography and brain perfusion scans and for partially irradiated organs, therefore the conversion presented in Eq. 3.6 is expected to provide an approximate estimate of scanner-specific organ dose. A preliminary validation of the organ dose estimates normalized by $\mathrm{CTDI}_{\mathrm{vol}}$ is presented in Sec. 3.2.8.

As explained in Sec. 3.2.6, we estimated the organ dose in the dose deposition tables by dividing energy deposited in an organ by the mass of the organ in the cropped phantom. For those organs that are not completely included in the cropped phantoms (see Table 3.2), this method of evaluation can lead to an overestimate of the *whole*-organ dose. If whole-organ dose is desired, then the organ dose estimate obtained using Eq. 3.5 should be adjusted using the fractional mass values of Table 3.2.

3.2.8 Validation

PENELOPE's Monte Carlo routines have been previously validated [57]. To validate that the linear combination of database values (Eq. 3.5) does not introduce additional biases, we compared organ doses estimated by the database to those estimated by Monte Carlo simulations of the cropped head and chest phantoms, each consisting of 1000 views, 10^9 emitted photons per view, and a 120 kV polyenergetic spectrum generated using the IPEM Report 78 software [72] (tungsten target, 12° anode angle, 0% voltage ripple, and 6 mm aluminum filtration). The scan geometry was identical to that used to generate the tables of normalized dose deposition, $Q_{\mathrm{O}}(\theta, E)$, described in Sec. 3.2.4. The total dose to each organ output from these simulations was compared to that calculated using Eq. 3.5 assuming the 120 kV spectrum and 10^9 emitted photons per view.

A study was also performed to validate the organ dose estimates normalized by the $\mathrm{CTDI}_{\mathrm{vol}}$ estimates, which can be used to adjust the database dose estimates

to reflect realistic scanner output (Eq. 3.6). In this study, the breast and lung dose per $CTDI_{vol}$ estimated by the database were compared to those reported by Turner et al. from Monte Carlo simulations of a different voxelized phantom. The Turner study found that organ dose per $CTDI_{vol}$ is generally scanner-independent [69]. However, the entire breast and lung were irradiated in the Turner study, while only a portion of the breast and lung were irradiated in our system geometry. Therefore, the organ dose per $CTDI_{vol}$ estimated from the database was scaled by the fraction of irradiated organ volume (57.7% for breast, 49.7% for lung) prior to comparison to Turner's values.

3.2.9 Obtaining Patient Attenuation Data

Analytical ray-tracing was performed to determine the attenuation at each incident photon energy and projection angle for the anthropomorphic head, tilted head, and chest phantoms. The attenuation was defined as the inverse of the transmission (i.e., $A = e^{\mu \cdot L}$) averaged over the central 100 pixels (2.5 cm) of the detector. The attenuation data can be used in modeling attenuation-based tube-current modulation schemes, as will be demonstrated in Sec. 3.2.10.

3.2.10 Example 1: Using the Dose Database to Investigate Change in Dose to Breast

In this section, we demonstrate how to use the dose database to calculate the change in dose to the breast for three protocols commonly used to reduce breast dose - reduced kV, partial scanning, and angular tube current modulation. Because acquisition techniques designed to reduce breast dose may increase lung dose (for example, during partial angle protocols, which typically increase dose during posterioanterior (PA) views for which the lung is less shielded by the rib cage and

thus more directly exposed to incident radiation), we also estimate the subsequent change in dose to the lung for each protocol. Changes in organ dose are reported relative to a 120 kV reference protocol.

Reference 120 kVp Protocol

The total dose to the breast for the reference protocol was calculated using Eq. 3.5 and $Q_{\text{breast}}(\theta, E)$. $\Phi(\theta, E)$ was set equal to a normalized 120 kV spectrum for all θ. Since we are interested only in change in dose, the absolute number of emitted photons used in Eq. 3.5 is irrelevant. Therefore, we set the number of emitted photons per view, $N_0(\theta)$, equal to one for all θ (Figure 3.2). Similarly, we used Eq. 3.5 with $Q_{\text{lung}}(\theta, E)$ to calculate total dose to the lung.

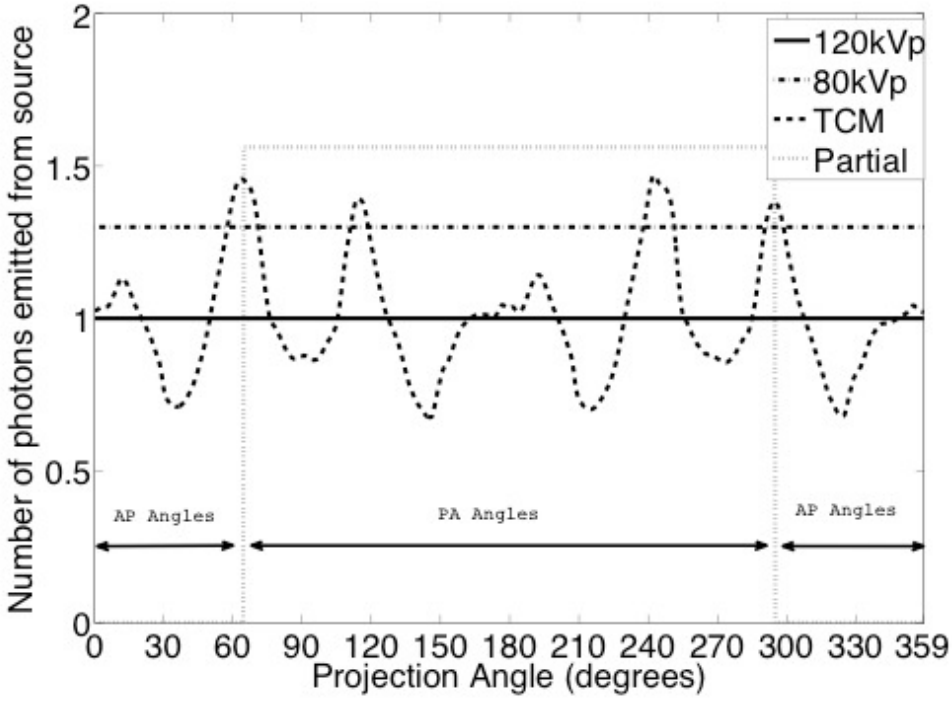

Figure 3.2: $N_0(\theta)$ for the protocols listed in Sec. 3.2.10. The area under the curve (i.e., $N_0(\theta)$ summed across all angles) is equal for the 120 kV, tube-current modulation, and partial scan protocols, while the 80 kV protocol has 1.3 times the number of emitted photons from the source.

Reduced kVp Protocol

The total dose to the breast for the 80 kV protocol was calculated using Eq. 3.5 and $Q_{\text{breast}}(\theta, E)$. $\Phi(\theta, E)$ was set equal to a normalized 80 kV spectrum for all θ. We had previously determined that to obtain a noise variance similar to that of the 120 kV protocol, the number of emitted photons at each angle of the 80 kV protocol should be increased by a factor of 1.3 relative to the 120 kV protocol [74]. Thus we set $N_0(\theta)$ equal to 1.3 for all θ (Figure 3.2). Similarly, we used Eq. 3.5 with $Q_{\text{lung}}(\theta, E)$ to calculate total dose to the lung.

Tube Current Modulation Protocol

The total dose to the breast for this protocol was calculated using Eq. 3.5 and $Q_{\text{breast}}(\theta, E)$. $\Phi(\theta, E)$ was set equal to a normalized 120 kV spectrum for all θ. Using the patient attenuation data, an optimal attenuation based tube-current modulation scheme was modeled in which the number of emitted photons at each angle, $N_0(\theta)$, was proportional to the square root of the attenuation at that angle, $\sqrt{A(\theta)}$ [75], while the total number of emitted photons for the scan remained the same as in the reference protocol (Figure 3.2). Similarly, we used Eq. 3.5 with $Q_{\text{lung}}(\theta, E)$ to calculate total dose to the lung.

Partial Angle Protocol

The total dose to the breast for this protocol was calculated using Eq. 3.5 and $Q_{\text{breast}}(\theta, E)$. $\Phi(\theta, E)$ was set equal to a normalized 120 kV spectrum for all θ. We set $N_0(\theta)$ equal to zero during the 360 projections (130°) centered about anterioposterior (AP) and to 1.56 during the remaining 640 projections (230°). These factors were chosen to represent the x-ray tube giving no output during the AP views and increased output during the PA views such that the total number of

emitted photons for the entire 360° scan remained the same as in the reference protocol (Figure 3.2). Similarly, we used Eq. 3.5 with $Q_{\text{lung}}(\theta, E)$ to calculate total dose to the lung.

3.2.11 Example 2: Using the Dose Database to Investigate Change in Dose to Eye Lens

In this section, we demonstrate how to use the dose database to calculate the change in dose to the eye lens for a tilted head scan relative to a non-tilted scan.

Reference (Non-tilted) Protocol

The total dose for the reference protocol was calculated using Eq. 3.5 and $Q_{\text{eye}}(\theta, E)$ for non-tilted head phantom. We set $\Phi(\theta, E)$ equal to a normalized 80 kV spectrum for all θ, and we set the number of emitted photons per view, $N_0(\theta)$, equal to one for all θ.

Tilted Protocol

The same method used for the non-tilted protocol was used to calculate the total dose except that in Eq. 3.5 we used the table of normalized dose deposition, $Q_{\text{eye}}(\theta, E)$, for the tilted head phantom.

3.3 Results

3.3.1 Dose Tables

Our simulations resulted in a table of normalized dose deposition, $Q_{\text{O}}(\theta, E)$, for each of the organs (or CTDI_{vol}) of the phantoms listed in Table 3.1, quantifying

the dose per emitted photon (mGy/emitted photon) for each incident photon energy, E, and projection angle, θ. Head [65] and body [66] bowtie filters were modeled for the simulations. Examples of tables of normalized dose deposition for the breast, lung, eye lens, and brain (grey matter) are shown in Figure 3.3. Viewing the tables graphically may provide insight for designing new protocols, since the projection angles and energies that deposit the most dose can be visualized. The uncertainty of the normalized dose deposition values varied across photon energy, projection angle, and organ. For example, the uncertainty in breast dose for the PA projection was 2.92% at 20 keV and 0.16% at 120 keV. When calculating the organ dose using Eq. 3.5, the individual statistical uncertainties at each incident photon energy and projection angle propagate such that the total statistical uncertainty for a calculated total organ dose or $\mathrm{CTDI}_{\mathrm{vol}}$ for a given spectrum and number of emitted photons is on the order of 0.0005%, indicating that the dose estimates have a high degree of certainty.

For each of the studied phantoms, it took approximately 7–10 days for the dose simulations to complete on our cluster of 500 CPUs, including simulation set-up time.

The tables of normalized dose deposition are saved as ASCII formatted files and are freely available for download at `http://www.eng.mu.edu/medicalimaging/dose_database` and as supplemental material for Rupcich et. al [76]. In addition, the patient attenuation data for the head, tilted head, and chest phantoms are also made available for use in designing attenuation-based tube current modulation schemes.

3.3.2 Validation

The percent differences between total organ doses obtained from the 120 kV polyenergetic Monte Carlo simulations and those calculated using Eq. 3.5 varied

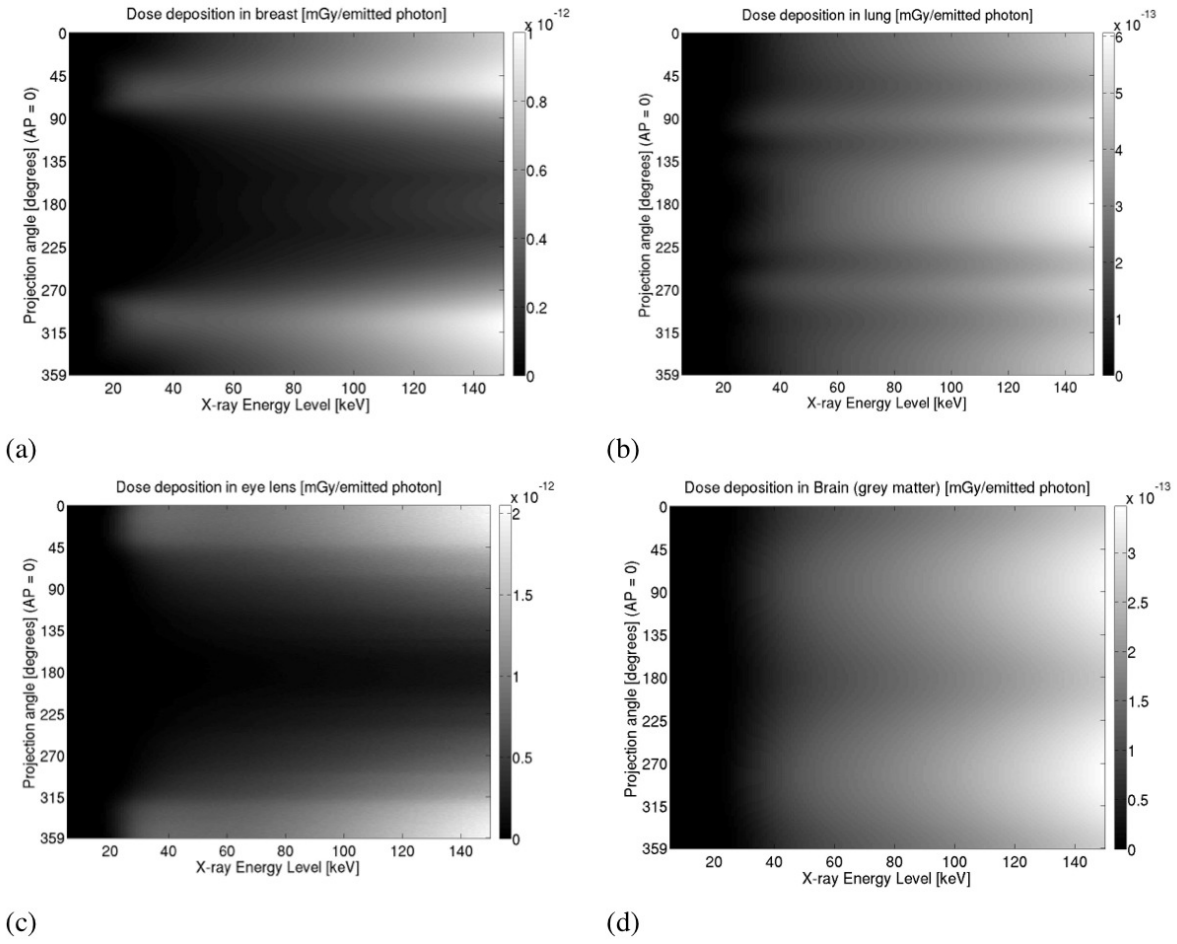

Figure 3.3: Examples of tables of normalized dose deposition. Table of normalized dose deposition $Q_{\mathrm{O}}(\theta, E)$ for (a) breast, (b) lung, (c) eye lens, and (d) brain (grey matter), quantifying organ dose per emitted photon (mGy/emitted photon) at each incident photon energy, E and projection angle, θ. Note that 0° and 180° correspond to AP and PA projections, respectively, and 90° and 270° correspond to left lateral and right lateral incidence, respectively.

between -0.91% and 0.15% for all organs except the red bone marrow, which yielded a percent difference of 6.1% for coronary angiography simulation and 4.3% for the brain perfusion simulation. These results demonstrate that the database yields dose estimates comparable to those calculated using conventional Monte Carlo simulations. The larger percent differences in the red bone marrow estimates may be due to the errors involved in estimating the mass energy absorption coefficient for an energy spectrum (as is done in the case of the Monte Carlo simulation) as

opposed to using the monoenergetic coefficient values (as is done when using the dose tables). The smaller percent differences for the other organs are expected due to the statistical variation inherent in results obtained via Monte Carlo simulations. The lung and breast organ dose per $CTDI_{vol}$ estimated from the database were 1.24 and 1.59, respectively (after scaling by the fraction of irradiated organ mass), compared to 1.59 and 1.77 as estimated by Turner et al. [69]. The differences in dose per $CTDI_{vol}$ (-22% for breast and -10% for lung) are reasonable considering the anatomical differences between the phantoms used in the two studies.

3.3.3 Example of Estimating Change in Dose to Breast

There was a 2.1%, 1.1%, and -32% difference in dose to the breast and a 2.1%, 0.6% and 4.7% difference in dose the lung for the reduced kV, tube current modulated, and partial angle scan protocols, respectively, relative to the 120 kV reference protocol, where a negative percentage indicates a decrease in dose (Table 3.3). The percent increase in dose to the lung for the partial angle scanning (as compared to the percent decrease in breast dose) is likely due to the increased tube-current during the PA views for which the lung is less shielded by the the rib cage than it is during the AP views and thus more directly exposed to the incident photons.

3.3.4 Example of Estimating Change in Dose to Eye Lens

There was a -19.2% difference in dose to the eye lens for tilted head scan relative to the non-tilted reference protocol, where the negative percentage indicates a decrease in dose.

Table 3.3: Percent change in breast and lung dose for dose-reduction protocols. The percent change in breast and lung dose for reduced kV, TCM and partial angular scanning (Partial) protocols relative to the 120 kV reference scan. A negative percentage indicates a decrease in dose.

Scan Type	Spectrum (kV)	$N_0(\theta)$	Change in Breast Dose (%)	Change in Lung Dose (%)
Reference	120	1.00	-	-
Reduced kV	80	1.30	2.1%	2.1%
TCM	120	$\propto \sqrt{A(\theta)}$	1.1%	0.6%
Partial	120	0.0 (130° AP) 1.56 (230° PA)	-32%	4.7%

3.4 Discussion

The presented database allows investigation of numerous dose reduction techniques with various scan parameters and protocols (e.g., x-ray spectrum, filtration, and tube-current modulation) for a specific scan geometry and voxelized phantom model without Monte Carlo simulations. Compared to available organ dose estimators [53], our database can model novel coronary angiography and brain perfusion acquisition techniques for the scan geometry presented, thus facilitating the development and optimization of new acquisition protocols. For example, a variety of dual-kV techniques can be modeled by changing $N_0(\theta)$ and $\Phi(\theta, E)$. The database may enable researchers with limited access to high-performance computing resources to develop novel acquisition methods. The presented method of calculating tables of normalized dose deposition could also be applied to other CT applications. For example, several studies evaluated the impact of spectral shape on dose and image quality in breast CT [20, 21]. Future work could develop dose deposition databases for phantoms and geometries specific to breast CT to enable efficient optimization of acquisition techniques.

The estimated organ dose results presented in this paper reflect changes in dose without quantifying image quality. The purpose of our examples is not to make

claims with respect to dose reduction for any of the studied protocols, but to illustrate how our method can be used to estimate changes in organ dose between protocols. To determine the optimal protocol from our examples, the reported changes in dose would need to be evaluated alongside a corresponding image quality study.

Because the data we have collected for each phantom are specific to the simulated geometries, dose estimates for helical trajectories, longitudinal tube-current modulation schemes, and FOVs other than those shown in Figure 3.1 cannot be obtained directly with our database. One strength of other dose databases, including those used by ImPACT's CTDosimetry Calculator [77, 78], is that organ dose coefficients are given for each of several 5 or 10 mm thick cross-sectional slabs that together constitute a large portion of the phantom (e.g., thigh to head). With the data organized in this fashion, one can obtain the total organ dose for a particular FOV by summing all of the organ coefficients for the slabs included in that FOV. The database presented in this paper enables organ dose estimation for coronary angiography and brain perfusion scans in particular, as these applications are of recent concern with regard to dose [7, 8, 79–81]. Future studies could aim to extend our database to include tables of normalized dose deposition for a number of thin cross-sectional slabs that together comprise the entire length of the phantom, in which case it would be possible to estimate total organ dose to all organs of the body for arbitrary FOVs and trajectory types as well as longitudinal tube-current modulation schemes.

Several studies have shown that absorbed organ dose tends to increase with decreasing patient size [41, 73, 82, 83]. Our database presents organ dose deposition tables for one average-sized female phantom. Thus, results for relative dose reduction between protocols obtained using our database are limited to a patient of similar size. Future studies could expand the database to include smaller and larger

patients, as well as pediatric and adult male phantoms, so that the effects of patient size on organ dose reduction for novel protocols may be investigated. Alternatively, coefficients for scaling organ dose estimates based on patient size have been investigated [73]. These scaling factors could be combined with a full-phantom database to enable more patient-size specific dose estimates from a single-phantom database.

The CTDI_{vol} normalization and multiplication method proposed in Sec. 3.2.7 provides an approximate conversion to scanner-specific dose estimates. At present, however, the method has not been fully validated for partially irradiated organs or a wide range of exam protocols [69, 73]. This does not limit the databases ability to quantify relative organ dose differences between protocols.

Despite these limitations, the proposed database and method of estimating organ dose (Eq. 3.5) can be used in conjunction with image quality studies to determine which dose reduction protocols provide the best ratio of image quality to dose. Since the database provides quantification and visualization of dose deposition across energy and projection angle, it may aid in determining optimal spectra and tube current modulation parameters. The database may be useful in understanding the dose implications of novel spectral, partial scanning, and few-view techniques, and may be particularly beneficial for developing dual kV techniques [84–87], for which the kV, filtration, and mA must be optimized for both the low and high energy acquisitions with respect to image quality and dose. This optimization may require numerous combinations of scan parameters, which can be easily modeled with the proposed database by modifying the spectra, $\Phi(\theta, E)$, and number of emitted photons, $N_0(\theta)$, in Eq. 3.5.

Chapter 4

Simulation Study Comparing CT Coronary Angiography Breast Dose Reduction Techniques using an Unknown-Location Signal-Detectability Metric

4.1 Introduction

Several studies have reported reduction in adult female breast dose during chest CT scans using dose reduction techniques such as breast shielding (29 – 57% reduction in breast dose) [33, 35–39] , angular tube current modulation (10 – 64%) [33, 35, 36, 41], partial-angle scanning (50%) [35], and reduced x-ray kV (27 – 50%) [33, 34]. When assessing the resultant image quality, however, these studies performed a subjective analysis [33, 37–39] and/or quantified task-independent metrics such as noise (pixel standard deviation) or contrast-to-noise ratio (CNR) [34–36, 39]. In medical diagnostic imaging, image quality must express the effectiveness with which the image can be used for a specific diagnostic task (e.g., detection of a lesion or estimation of the degree of stenosis). Accordingly, the International Commission on Radiological Units (ICRU) recommends the objective assessment of image quality, and more specifically, the use of task-dependent metrics over task-independent metrics, as the latter may not always be directly indicative of the diagnostic performance of the intended task and thus may not accurately

represent the true "quality" of an image [42].

As discussed in Chapter 2, the AUC ROC figure of merit can be used as a signal-detectability metric for signal detection tasks consisting of a single signal for which the location is known. For tasks for which the signal location is unknown, which are often more clinically relevant, we can estimate the localization ROC (LROC) curve, which plots the fraction of true positive images with a correctly localized signal versus the fraction of false positive images. The area under the LROC curve (AUC LROC), may then be used as a detectability metric instead of AUC ROC for tasks in which the signal location is unknown [88]. For cases in which there are multiple signals with unknown locations, we may use the free-response operating characteristic (FROC) method, which allows the observer to mark and score all potentially suspicious locations. The FROC curve plots the ratio of true signals detected versus the average number of false signals reported per image. As such, the FROC graph does not have a well-defined right side limit, and so the area under the FROC curve is undefined and cannot be used as a performance index. Popescu recently introduced an exponential transformation of the FROC curve (EFROC) that maps the infinite interval of the abscissa to a finite one and then shows that the area under the EFROC curve (AUC EFROC), can be used as a detectability metric [89]. Moreover, this method is nonparametric in that AUC EFROC is estimated directly from the confidence scores reported by the observer, thereby avoiding the reliance on specific models or assumptions typically required when estimating an area under the curve metric via direct integration under its associated ROC curve.

In general, image quality metrics can be plotted as a function of a physical parameter of the imaging process (e.g., radiation dose) to summarize the effect of that parameter on signal detectability [42]. Such plots can then be obtained for several different imaging systems, reconstruction algorithms, or techniques to

determine which ranks the highest with respect to the chosen parameter. For example, a recent study compared CT images reconstructed using filtered backprojection to those reconstructed using an iterative algorithm by plotting AUC LROC vs. dose (mAs) curves for the two algorithms and observing which produced a higher detectability at a given radiation dose [90].

The purpose of this study was to compare the signal detectability, as quantified by the AUC EFROC estimator, $\hat{A}_{FE}$, of several dose reduction techniques over a range of breast dose levels. Because the lung is also considered a highly radiosensitive organ [91] and lung dose may be affected by breast dose reduction methods, we further investigated AUC EFROC versus lung dose. We estimated other commonly used image quality metrics, including noise, contrast, and CNR, to assess their relationship to AUC EFROC and determine whether they may serve as accurate predictors of signal detectability or are sufficient quantifiers of image quality. We studied two tasks —detection and localization of small diameter/high contrast and large diameter/medium contrast signals — to investigate how the dose savings potential may vary depending on the task, where "detection and localization" refers to the case in which the signal location is unknown, and thus the signal must be both detected and have its location correctly identified.

4.2 Materials and Methods

We performed analytical raytracing of x-rays across an anthropomorphic female thorax phantom for a 120 kV reference protocol, as well as five "dose reduction" protocols intended to reduce dose to the breast during CT coronary angiography (CTCA) acquisitions, including 120 kV posteriorly-centered partial angle, 120 kV angular tube-current modulated (TCM), 120 kV breast-shielded, 80 kV, and 80 kV posteriorly-centered partial angle protocols. Images were then

reconstructed using filtered backprojection. The first image quality task was detection and localization of 4-mm diameter, 3.25 mg/mL ($\approx$ 34 HU contrast at 120 kV) iodine signals randomly located in the heart region, chosen to loosely represent detection of iodine uptake during a CTCA scan. A second task, the detection and localization of 1-mm, 6.0 mg/mL ($\approx$ 55 HU contrast at 120 kV) iodine signals, was chosen to investigate if and how task variability may affect potential dose savings. For each protocol, we calculated the AUC EFROC estimator, $\hat{A}_{FE}$, and plotted it versus breast dose to investigate the potential of that protocol to reduce dose to the breast without affecting the image quality as quantified by $\hat{A}_{FE}$, i.e., the detectability of the signals. Because noise, contrast, and CNR are often used in assessing image quality, we also plotted these metrics against breast dose. We further investigated each of the metrics versus lung dose. The following subsections describe in further detail the phantom and task design, CT simulation geometry, and our methods for simulating the images, estimating dose, and calculating $\hat{A}_{FE}$ for each protocol and task.

4.2.1 Unknown-Location Signal-Detectability Metric Estimation

This study estimated image quality using a task-based procedure that detected signals at unknown locations in the image region of interest (cardiac region). The procedure comprises (1) a signal searching algorithm that produces free response data, i.e., the scores of all suspicious locations (either true or false signals) and their respective location marks, and (2) a nonparametric free response data analysis method [89]. The signal searching and the data analysis have been applied as recently presented by Popescu and Myers [92]. The signal searching algorithm was initially presented in Popescu and Lewitt [93].

For a given (signal-absent or signal-present) image region of interest (ROI), signal detection is performed using a signal search algorithm with two main steps.

The first step generates an auxiliary scan image by cross-correlating the image ROI with a series of shifted signal templates. We assume that an image ROI consists of M pixels and is represented in vectorized form by $\mathbf{f}$. A signal template, $\mathbf{w}_i$, consists of M pixels, all with a value of zero except those located within the disk of radius R_t centered at point i, which have a value of one. The value of the scan image at the ith pixel location, z_i is given by Equation 4.1:

$$z_i = \sum_{i=1}^{M} \mathbf{w}_i^{\mathrm{T}} \mathbf{f} \tag{4.1}$$

In other words, z_i is the sum of the pixel values within the disk of radius R_t centered at point i, providing a measure of the match between the signal template and the pixels around that location. z_i is the *scan score* for the ith pixel in $\mathbf{f}$, and $\mathbf{z}$ is referred to as the *scan image*. The second step involves marking all suspicious locations of the image. We first determine the maximum scan score of the scan image, $\mathbf{z}$. The scan score is recorded, and the pixels within a disk of radius twice that of the signal radius around this point are masked (i.e., set to zero). This step is then repeated with the remaining unmasked pixels of $\mathbf{z}$ until the local maximum scan score is less than a chosen stopping limit, z_0. The output of this step is a descending list of scan scores for all suspicious locations of the image with a value above z_0.

Using this procedure, we obtain $\{X_i\}$, the scan scores for I true signals present, and $\{Y_j\}$, the scan scores of a total of J false signals retrieved from N signal-absent image ROIs. From these two sets of data, we can estimate AUC EFROC as:

$$\hat{A}_{FE} = \frac{1}{I} \sum_{i=1}^{I} e^{-\frac{1}{N}\sum_{j=1}^{J} H(Y_j - X_i)} \tag{4.2}$$

where $H(k)$, the Heaviside equation, is equal to 1 if $k > 0$; $\frac{1}{2}$ if $k = 0$; or 0 if $k < 0$.

The statistical properties of this signal-detectability estimator and its relations with ROC, LROC, and alternative FROC (AFROC) metrics have been studied in detail in [89]. In addition, nonparametric equations for the variance calculations are provided.

4.2.2 Simulation Setup

The raytracing and Monte Carlo simulations described in this study were performed with the penEasy_Imaging software package [54, 55] which relies on the previously validated PENELOPE Monte Carlo radiation transport routines and material attenuation database [57]. The raytracing software did not model x-ray scatter.

This study used the 0.5 mm voxelized anthropomorphic phantom, Ella, from the Virtual Family [58, 94], representing an average-sized 26 year old female (height: 1.63 m, weight: 58.7 kg). To relax computational memory requirements during simulations, we cropped the phantom to the thorax, measuring 31 cm by 22 cm in the lateral and anteroposterior directions, respectively, and 30 cm in the axial direction. Topograms of the whole body and cropped phantom are shown in Figure 4.1.

The breast was modeled as two separate parts: an internal glandular mass and an external 1 cm thick surrounding layer of adipose. Thus, voxels representing the internal glandular mass were modeled as 100% glandular tissue, while the surrounding layer of voxels were modeled as 100% adipose. As such, "dose to breast" in the context of this study refers to dose to the 100% glandular material. Voxels representing the following organs/tissues were modeled according to their respective atomic compositions and densities as given by ICRP publication 110 [59]: fat (adipose), glandular tissue, blood, cartilage, esophagus, stomach, heart, kidney, liver, muscle, pancreas, skin, spleen, thyroid, and soft tissue. Voxels representing the

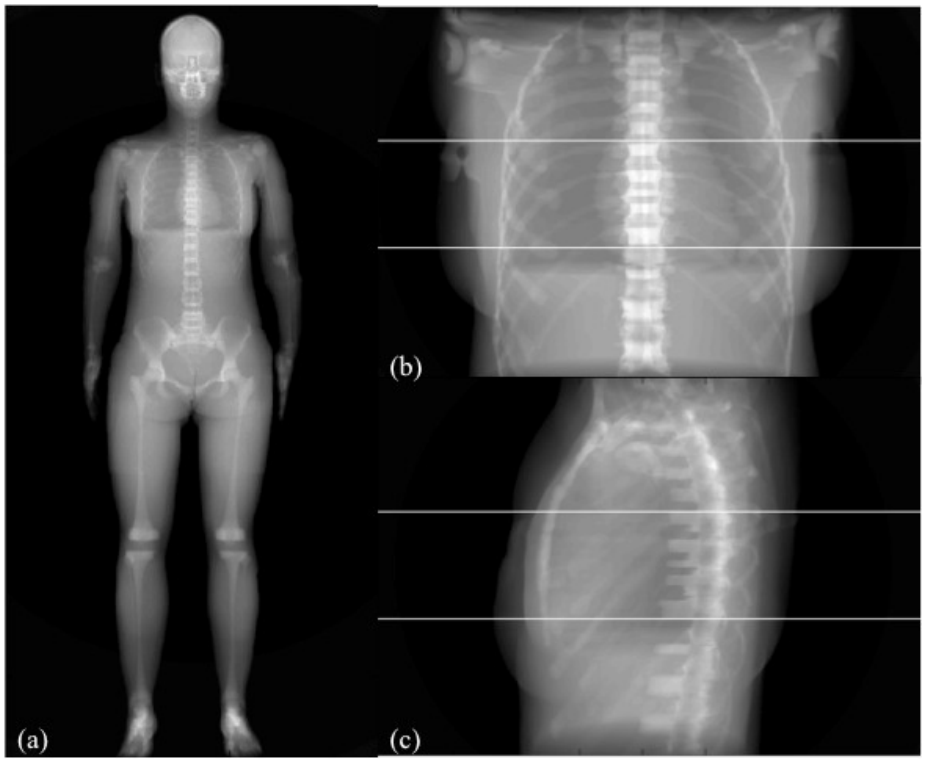

Figure 4.1: (a) Topogram of the whole body (non-cropped) female phantom. (b) Anterioposterior and (c) lateral topograms of the cropped phantom. The scan field-of-view is represented by the space between the white horizontal lines and corresponds to a CTCA scan.

following organs/tissues were modeled according to their respective atomic compositions and densities as given by Woodard & White [60]: lung (blood filled, 50% inflated, 50% deflated, density: 0.655 g/cm^3), cerebrospinal fluid, and connective tissue. The diaphragm was modeled as muscle. All skeletal voxels were modeled as homogenous bone (density: 1.4 g/cm^3) as given by Cristy & Eckerman [61].

The image quality tasks were detection and localization of 4-mm, 3.25 mg/mL and 1-mm, 6.0 mg/mL iodine contrast signals located within the heart region (Figure 4.2a). As was explained in subsection 4.2.1, the signal search algorithm and method for calculating $\hat{A}_{FE}$ requires a set of signal-absent ROIs, which were obtained by simulating images of the phantom with no iodine contrast elements present, as well as a set of signal-present ROIs, which were obtained by

simulating images of the phantom with either five 4-mm, 3.25 mg/mL (Figure 4.2b) or five 1-mm, 6.0 mg/mL (Figure 4.2c) cylindrical iodine contrast elements located in a single axial plane within the heart region.

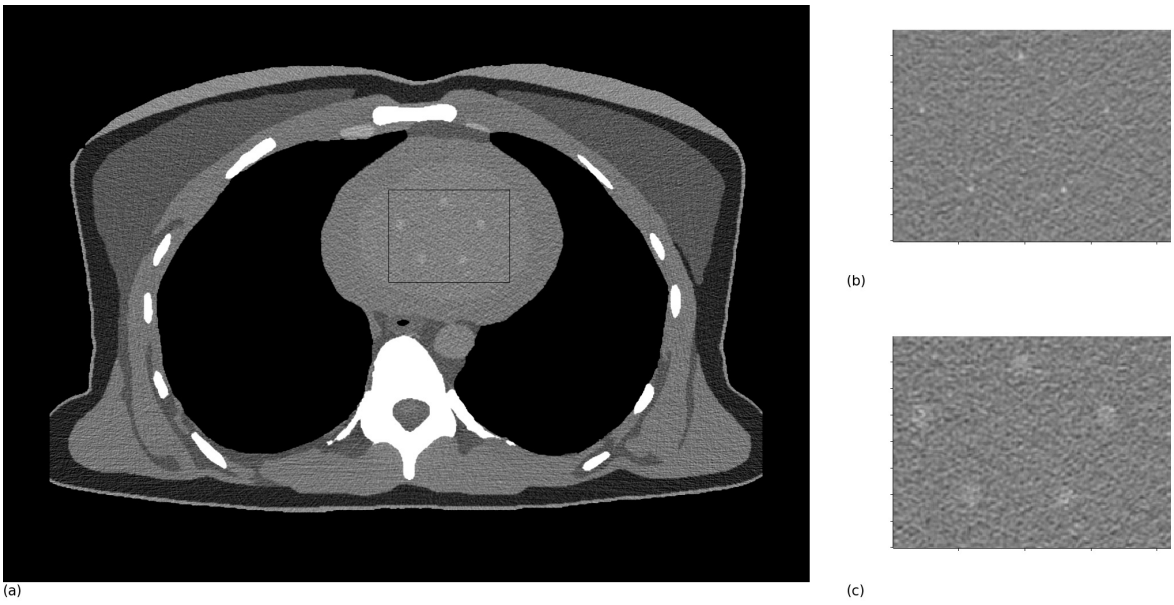

Figure 4.2: (a) A full field-of-view reconstructed image of the phantom (4-mm, 3.25 mg/mL signal-present). The black box in the heart region indicates the signal search ROI (52.5 × 40 mm^2) used for calculating $\hat{A}_{FE}$ for both tasks. (b) An example of a signal-present ROI with the 1-mm, 6.0 mg/mL signals. (c) An example of a signal-present ROI with the 4-mm, 3.25 mg/mL signals.

4.2.3 Simulation geometry

The source-to-detector distance for each simulation was 100 cm, with a source-to-isocenter distance of 50 cm. We modeled a single-rotation stationary cone-beam system with a flat-panel detector, no table translation, and a beam width at isocenter of 8 cm (Figure 4.1b and 4.1c), which was chosen to represent the scanning capabilities of volumetric CT scanners during CTCA scans [63, 64]. We modeled a point source with a fan angle of 53.13°, which was wide enough to cover the entire width of the cropped phantom. A bowtie filter corresponding to that used for the body protocols of a Siemens AS+ scanner [66] was modeled during all

simulations and dose estimations.

4.2.4 Investigated protocols

We simulated six CT protocols for each of the two tasks, including one reference and five dose reduction protocols:

1. 120 kV (reference)
2. 120 kV partial angle (232° posteriorly centered)
3. 120 kV angular TCM (proportional to square root of attenuation [75])
4. 80 kV
5. 80 kV partial angle (232° posteriorly centered)
6. 120 kV breast shielded

Both the 120 kV and 80 kV spectra used in this study were generated using the IPEM Report 78 software [72] (tungsten target, 12° anode angle, 0% voltage ripple, and 6 mm aluminum filtration).

One thousand projections were collected over 360° for the four non-partial angle protocols: 120 kV, 120 kV TCM, 80 kV, and 120 kV shielded. The two partial angle protocols reduce direct exposure to the breast by applying tube-current only during the posteriorly-centered 232°; thus only the posteriorly-centered 645 projections were collected for these protocols.

For the 120 kV angular TCM protocol, the number of photons emitted from the source (i.e., tube-current) at each projection angle was modulated proportionally to the square root of the attenuation at that angle. This modulation scheme is theoretically optimal with respect to noise (pixel standard deviation) within a homogenous phantom [75].

For the 120 kV shielded protocol, a 6 mm thick lead shield with density 0.1134 g/cm^3 (1% the actual density of lead) with an approximate length of 42 cm was created using mathematical quadrics and positioned approximately 1 cm above the chest (Figure 4.3). Commercially available bismuth shields are typically composed of a bismuth mixture. Due to the proprietary nature of this mixture, we instead modeled the shield using the abovementioned thickness and density of lead, which has been shown to provide attenuation equivalent to commonly used bismuth breast shields (56% attenuation at 120 kVp)[35, 38].

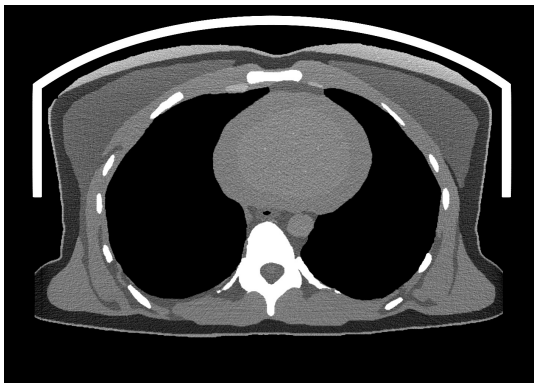

Figure 4.3: An image of the phantom with the breast shield.

4.2.5 Dose Estimation

We used our previously proposed dose database [76] to estimate protocol-specific "dose conversion factors," which quantified the breast dose and lung dose per photon emitted from the source for each protocol. Because our dose database cannot model shielded scans, we performed Monte Carlo simulations (following the methods of Rupcich et. al [76]) of the female phantom with the shield described in subsection 4.2.4 to estimate the dose per photon emitted from the source for the shielded protocol. These conversion factors were then multiplied by the number of photons emitted from the source during raytracing simulations to calculate the breast and lung dose.

4.2.6 Image Generation

Ray-traced images with added Poisson noise were generated for each of the studied protocols assuming the scan parameters described in subsection 4.2.4. CT projection data was simulated for the 4-mm, 3.25 mg/mL task for the reference 120 kV protocol at 14 different breast dose levels ranging from approximately 1 to 81 mGy, corresponding to a number of photons emitted from the source ranging from approximately 4.0e9 to 4.0e11. Similarly, projection data was simulated for the 1-mm, 6.0 mg/mL task for 18 different breast dose levels ranging from approximately 1 to 254 mGy, corresponding to a number of photons emitted from the source ranging from approximately 5.7e9 to 1.3e12. These photon numbers were selected empirically to provide corresponding values of $\hat{A}_{FE}$ that spanned the full performance range (i.e., from very poor to virtually certain signal detectability). The breast dose resulting from the reference 120 kV protocol for each simulated number of photons was calculated by multiplying the breast dose conversion factor of the reference protocol (subsection 4.2.5) by the number of photons emitted from the source. Similarly, each of the five studied breast dose reduction protocols were then simulated at the 14 (4-mm, 3.25 mg/mL task) or 18 (1-mm, 6.0 mg/mL task) different breast dose levels. The simulated CT data was reconstructed using filtered backprojection onto 0.25 mm^2 pixels. The partial-scan data was reconstructed using filtered backprojection with Parker weighting [95]. A water beam-hardening correction algorithm was implemented to reduce cupping artifacts [96].

4.2.7 Assessment of Dose and Image Quality

We assessed task-based objective image quality by comparing $\hat{A}_{FE}$ vs. dose curves of the studied protocols. We also estimated the noise, contrast, and CNR for each protocol.

Signal Detectability, $\hat{A}_{FE}$

For this study, the signal search area for signal-present and signal-absent images for both tasks was a two-dimensional 52.5 × 40 mm^2 ROI located in one axial plane inside the heart (Figure 4.2a). The radius of the disk within each 2D signal template was one pixel larger than that of the signal, i.e., $R_t = 0.75$ mm for the 1-mm diameter signal and $R_t = 2.25$ mm for the 4-mm diameter signal. To assure low statistical uncertainty in $\hat{A}_{FE}$, we used 40 signal-present and signal-absent ROIs for the 1-mm signal task, and 70 signal-present and signal absent ROIs for the 4-mm task. The threshold, z_0, was chosen so that a large enough number of suspicious locations per image were retrieved.

The AUC EFROC estimator is scalable with the search area size. For homogeneous regions, $\hat{A}_{FE}$ can be scaled relative to a given reference image size, Ω, by setting $N = \Omega_T/\Omega$, where Ω_T is the total searched area for false signals (i.e., the signal search area times the number of signal-absent images). We used $\Omega = 3200$ mm^2 (e.g., 56.6 × 56.6 mm^2) for the 4-mm, 3.25 mg/mL task and $\Omega = 312.5$ mm^2 (e.g., 17.7 × 17.7 mm^2) for the 1-mm, 6.0 mg/mL task.

AUC LROC is used for tasks involving detection and localization of a single signal. In theory, the AUC LROC estimator, $\hat{A}_{\mathrm{L}}$ is equivalent to $\hat{A}_{\mathrm{FE}}$ when the latter is expressed for a search area size that is twice the size of the ROI area used in estimating the former[89]. Thus, for the 4-mm task, our values of $\hat{A}_{\mathrm{FE}}$ for a search area size of 3200 mm^2 are equivalent to corresponding $\hat{A}_{\mathrm{L}}$ values for an ROI size of 1600 mm^2 (e.g., 40 × 40 mm^2). Similarly, for the 1-mm task, the search area size of 312.5 mm^2 represents an A_{L} ROI size of 15.7 mm^2 (e.g., 12.5 × 12.5 mm^2).

$\hat{A}_{FE}$ was calculated for each CT protocol for both tasks from images simulated at several equivalent breast dose levels. It is important to quantify the effects of the different CT protocols on dose to organs other than the breast. The lung dose was calculated for each protocol at each breast dose level by multiplying

the lung dose conversion factors described in subsection 4.2.5 by the number of simulated photons emitted from the source. We investigated lung dose because of its high radiosensitivity and presence throughout the thorax for the chosen scan geometry.

Dose Reduction at Equivalent $\hat{A}_{FE}$

The percent change in dose for a given protocol (relative to the reference protocol) was estimated by comparing the doses required to achieve a specified $\hat{A}_{FE}$. An $\hat{A}_{FE}$ value too far outside the operating range of a real imaging system could produce misleading results. We chose a value of 0.96, which is close to a clinically realistic AUC ROC operating point for systems performing multislice CTCA [97]. Thus, for any given "dose reduction" protocol, we quantified dose performance as the percent difference in dose relative to the reference protocol achieved while maintaining an $\hat{A}_{FE}$ of 0.96.

For a given protocol and signal size, we randomly sampled 500 $\hat{A}_{FE}$ vs. breast dose curves assuming a normal distribution of $\hat{A}_{FE}$ at each dose value with the mean and variance of $\hat{A}_{FE}$ as estimated in section 4.2.7. Each realization of the $\hat{A}_{FE}$ vs. breast dose curve was interpolated to estimate the breast dose at $\hat{A}_{FE} = 0.96$. This resulted in 500 estimates of breast dose at $\hat{A}_{FE} = 0.96$, from which we calculated the mean breast dose, $\hat{D}$, and variance, $\hat{\sigma}^2$. The percent change in breast dose for protocol p relative to the reference protocol, ref, was estimated using Equation 4.3:

$$\% \text{ change in dose} = \frac{(\hat{D}_p - \hat{D}_{ref})}{\hat{D}_{ref}} \cdot 100\% \tag{4.3}$$

The variance in the estimate of a percent change in dose was calculated by propagating $\hat{\sigma}^2$ through Equation 4.3. The percent change in lung dose for each

protocol was calculated similarly.

Pixel Noise, Contrast, and Contrast-to-noise Ratio Estimation

Noise was estimated for each protocol by taking the pixel standard deviation of background ROIs across all images collected for that protocol for the given task. The background ROI in each image was a 27.75×19.5 mm^2 rectangle located in the center of the heart region (the background ROIs did not contain signals). Contrast was estimated by calculating the absolute value of the difference between the mean across all images of a background ROI and the mean across all images of an ROI within a signal. The area of the signal ROI for the 1-mm-diameter signal was 0.79 mm^2 and the area of the signal ROI for the 4-mm-diameter signal was 12.6 mm^2. CNR was then calculated by dividing the contrast by the noise. Similar to $\hat{A}_{FE}$, noise and CNR were also plotted against breast dose and lung dose. The pixel noise, contrast, and CNR associated with an $\hat{A}_{FE}$ of 0.96 for protocol p were obtained by interpolating the noise, contrast, and CNR vs. dose curves, respectively, for $\hat{D}_p$.

4.3 Results

Figure 4.4 plots $\hat{A}_{FE}$ versus breast dose and lung dose for each of the studied protocols and for both tasks. Figure 4.4a and Figure 4.4c indicate that for both tasks, the 80 kV, 80 kV partial, and 120 kV partial protocols exhibited better signal detectability than the reference protocol at a given breast dose, while the shielded protocol exhibited poorer detectability. The TCM protocol exhibited comparable performance to the reference protocol. Further, at a given breast dose, performance was better for a partial scan than for a full scan (at the same kV).

Figure 4.4b and Figure 4.4d indicate that for both tasks, the 80 kV and 80 kV partial protocols exhibited better performance per lung dose than the reference

protocol. At a given lung dose, the TCM protocol exhibited comparable performance to the reference protocol, while the 120 kV partial and shielded protocols exhibited poorer performance. Unlike the $\hat{A}_{FE}$ vs. breast dose curves, the $\hat{A}_{FE}$ vs. lung dose curves indicate better performance for full scans than for partial scans (at the same kV). In general, 80 kV protocols showed better performance per breast dose or lung dose than 120 kV protocols.

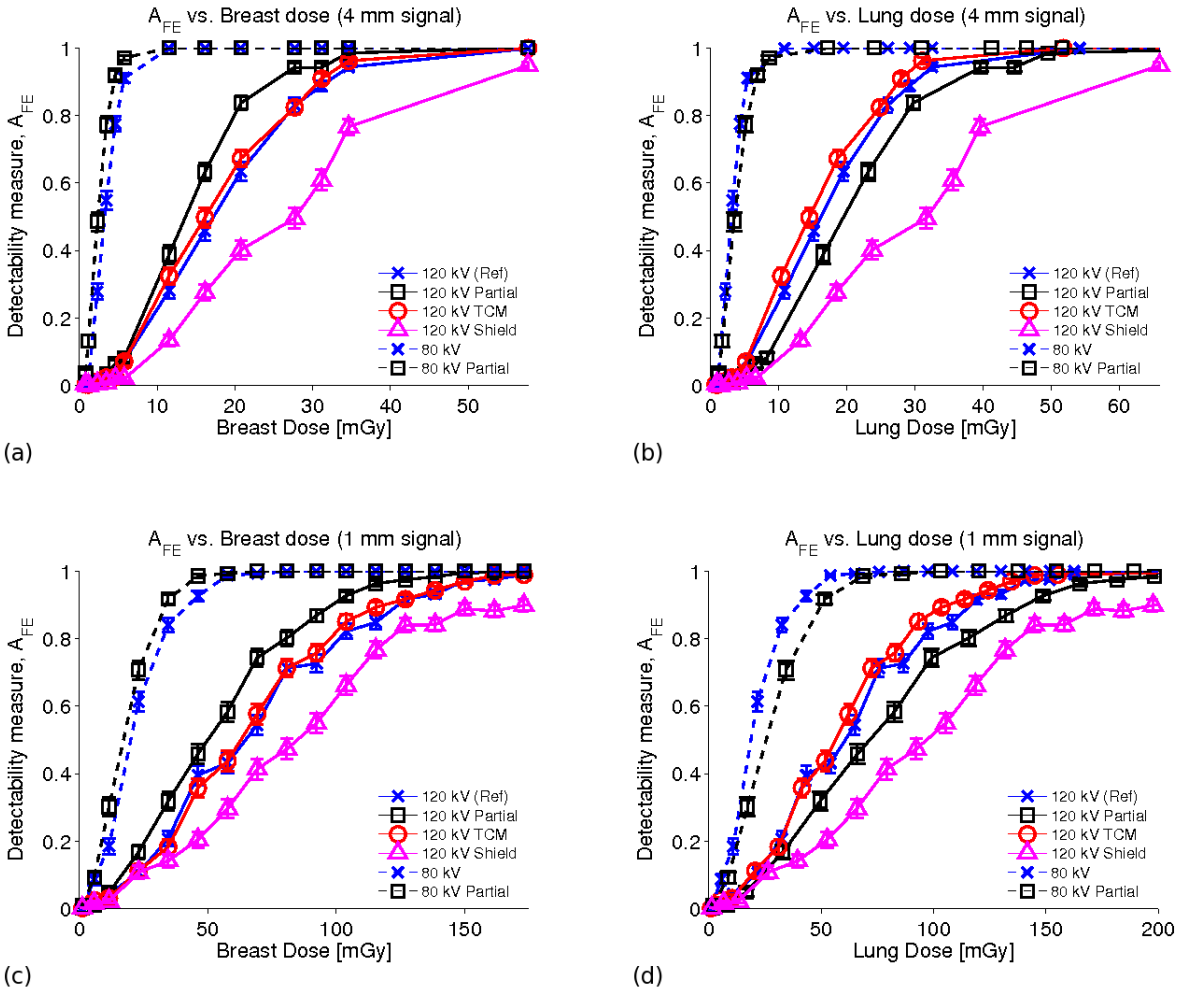

Figure 4.4: (a) $\hat{A}_{FE}$ vs. breast dose and (b) lung dose for the 4-mm, 3.25 mg/mL signals. (c) $\hat{A}_{FE}$ vs. breast dose and (d) lung dose for the 1-mm, 6.0 mg/mL signals. Note that error bars are present in the plots and represent one standard deviation in either direction, but in most cases are too small to see over the plot markers.

Figure 4.5 plots the noise standard deviation versus breast dose and lung dose for each of the studied protocols. Because the signals are small, it is safe to

assume the noise is not dependent on the signal. Thus, the following results apply for both the 4-mm and 1-mm signal sizes. Figure 4.5a indicates higher noise per breast dose for the 80 kV, 80 kV partial, and shielded protocols, and lower noise per breast dose for the 120 kV partial protocol, relative to the reference protocol. The TCM protocol showed comparable noise per breast dose to the reference scan. Figure 4.5b shows relatively higher noise per lung dose for all protocols except the TCM protocol, which exhibited comparable noise per lung dose to the reference protocol. Noise per breast dose was lower for a full scan than for a partial scan (at the same kV), while the opposite was true for noise per lung dose. In general, 80 kV protocols yielded higher noise per breast dose or lung dose than 120 kV protocols.

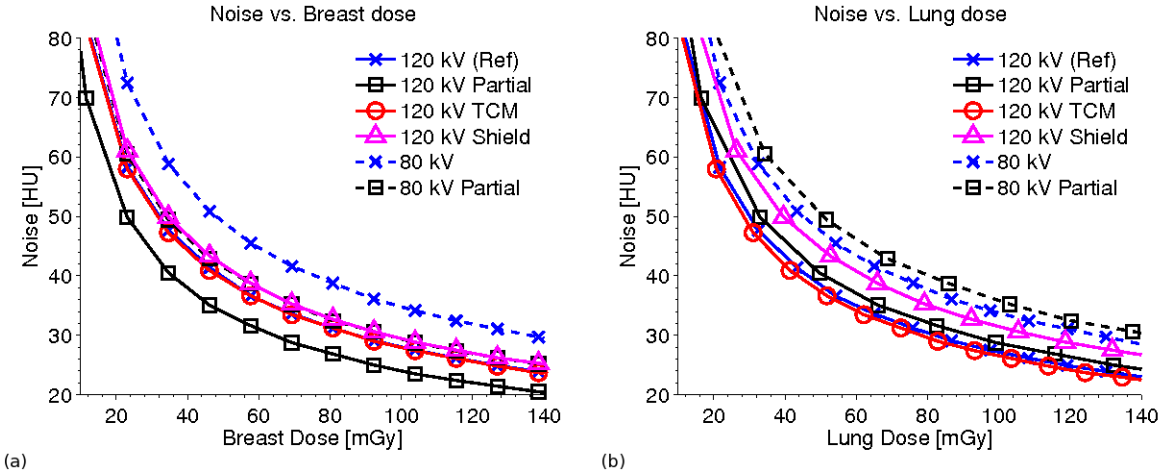

Figure 4.5: (a) Noise vs. breast dose and (b) lung dose. Noise is measured as pixel standard deviation.

Figure 5.4 plots the CNR of the investigated protocols versus breast and lung dose for both tasks. The CNR curves indicate a similar relative ranking of protocol performance as the corresponding $\hat{A}_{FE}$ curves.

Table 4.1 and Table 4.2 list values of $\hat{A}_{FE}$, CNR, contrast, noise, and lung dose for each protocol for the 4-mm, 3.25 mg/mL and 1-mm, 6.0 mg/mL task at equivalent breast dose ($\approx$ 21 mGy for the 4-mm task, and $\approx$ 81 mGy for the 1-mm task). The probability of signal detection for the 80 kV and 80 kV partial protocols

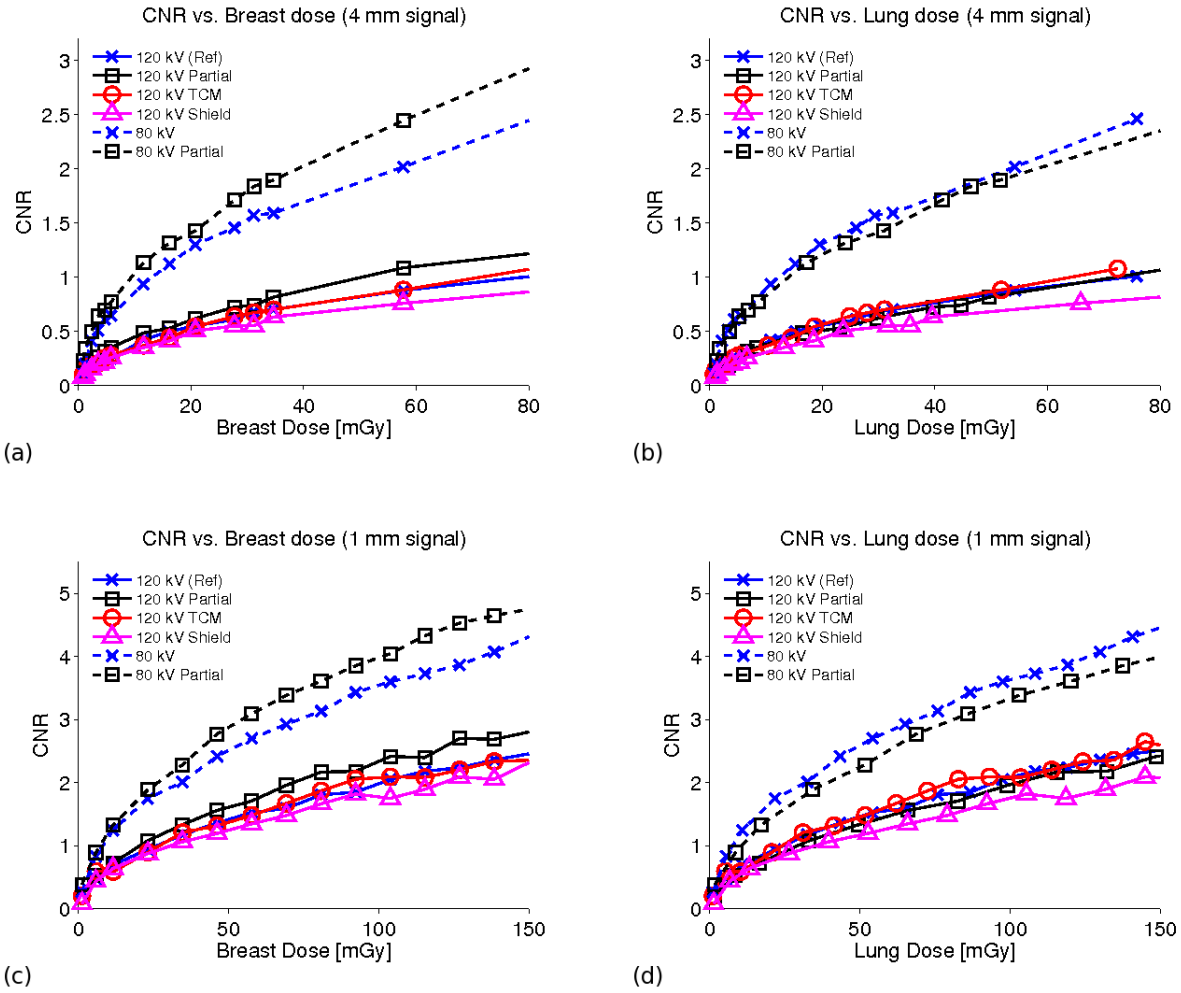

Figure 4.6: (a) CNR vs. breast dose and (b) lung dose for the 4-mm, 3.25 mg/mL signals. (c) CNR vs. breast dose and (d) lung dose for the 1-mm, 6.0 mg/mL signals.

Table 4.1: Image quality metrics and lung doses for each protocol for the 4-mm, 3.25 mg/mL task at equivalent breast dose ($\approx$ 21 mGy).

Protocol	$\hat{A}_{FE}$	CNR	Contrast [HU]	Noise [HU]	Lung dose [mGy]
120 kV (ref)	0.63	0.55	33.8	61.2	19.5
120 kV Partial	0.84	0.62	32.5	52.4	29.7
120 kV TCM	0.67	0.54	33.3	61.2	18.6
120 kV Shield	0.40	0.50	32.4	64.3	23.7
80 kV	1.00	1.30	99.3	76.4	19.5
80 kV Partial	1.00	1.43	91.4	64.1	30.9

is virtually certain ($\hat{A}_{FE} = 1.0$), with lower detectability for the other protocols. Figure 4.7 shows an example of a signal-present image for each protocol at equivalent breast dose for the 4-mm, 3.25 mg/mL task.

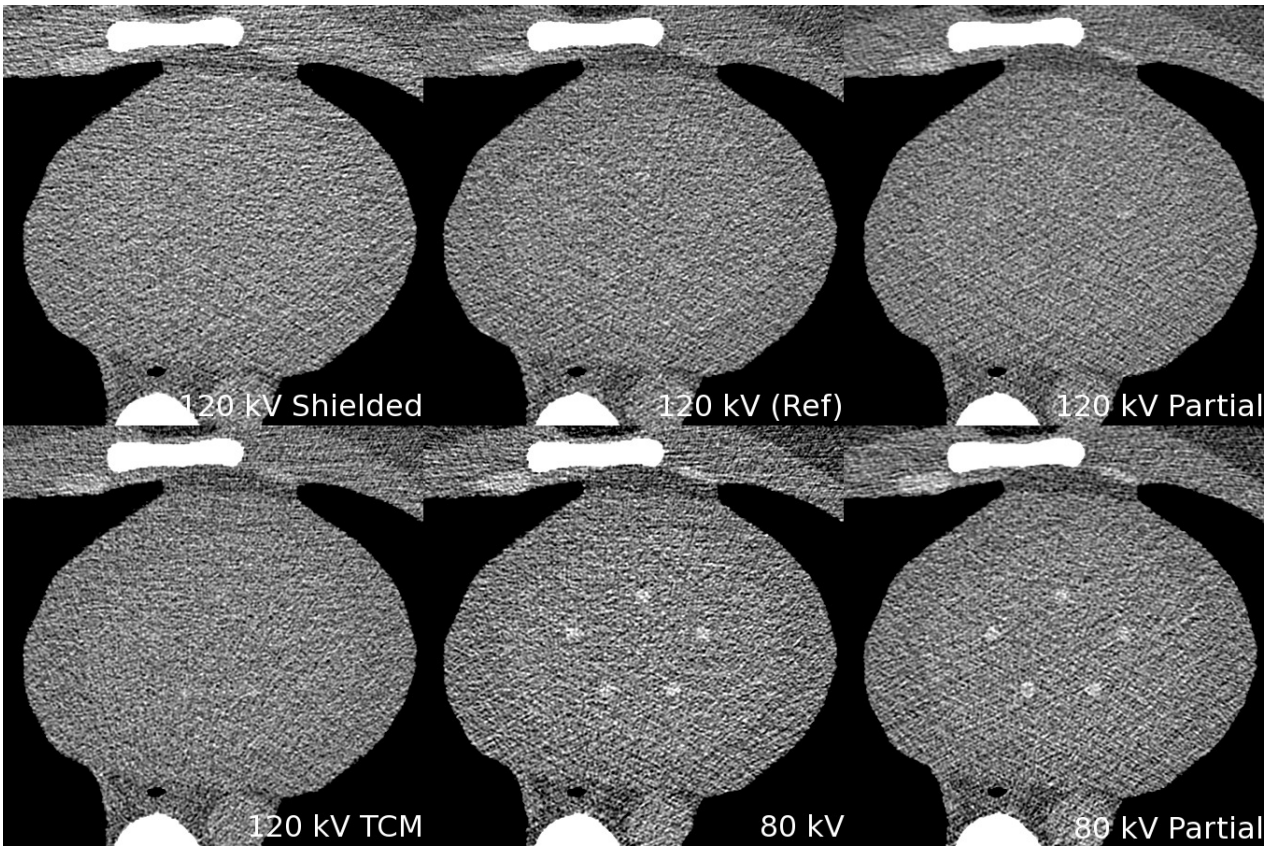

Figure 4.7: Example of a 4-mm, 3.25 mg/mL signal-present image for each protocol at equivalent breast dose (≈ 21 mGy). Window/level is 400/115 HU for the 120 kV images, and 400/280 HU for the 80 kV images.

Table 4.2: Image quality metrics and lung doses for each protocol for the 1-mm, 6.0 mg/mL task at equivalent breast dose (≈ 81 mGy).

Protocol	$\hat{A}_{FE}$	CNR	Contrast [HU]	Noise [HU]	Lung dose [mGy]
120 kV (ref)	0.71	1.81	56.4	31.2	75.9
120 kV Partial	0.80	2.17	58.2	26.9	115.7
120 kV TCM	0.71	1.87	58.4	31.2	72.5
120 kV Shield	0.47	1.67	54.3	32.7	92.3
80 kV	1.00	3.13	121.5	38.8	76.6
80 kV Partial	1.00	3.61	117.1	32.5	120.3

Table 4.3 lists values of CNR, contrast, noise, breast dose and lung dose for each protocol at an equivalent $\hat{A}_{FE}$ of 0.96 for the 4-mm, 3.25 mg/mL task. Figure 4.8a indicates for this task and value of $\hat{A}_{FE}$ that the 120 kV TCM, 120 kV partial, 80 kV, and 80 kV partial protocols reduced dose to the breast by 6.0%, 17.6%, 80.5%, and 85.3%, respectively, while the shielded protocol increased dose to

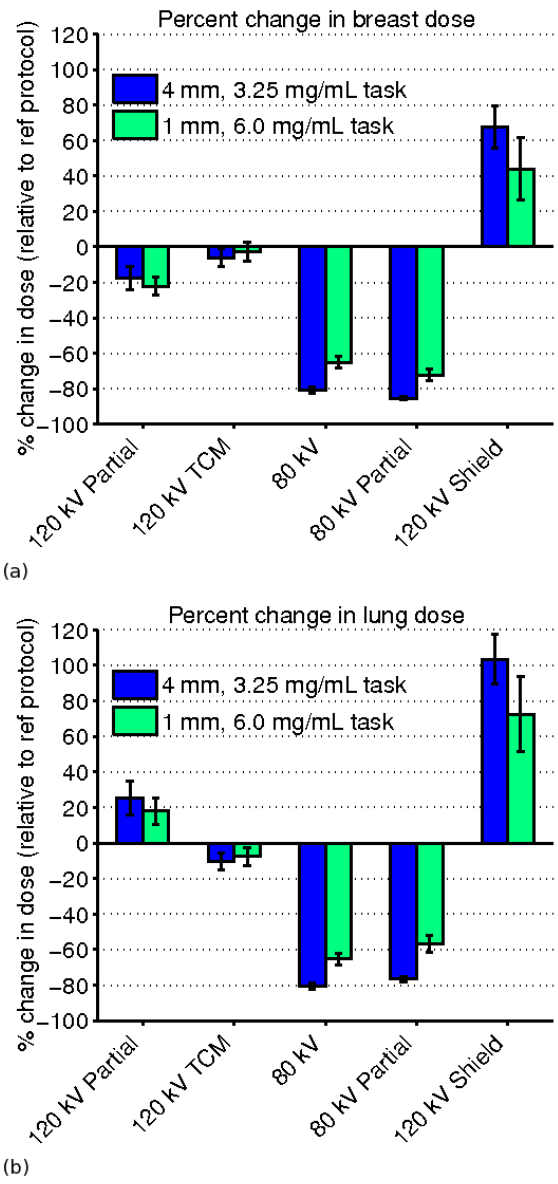

Figure 4.8: Percent change in (a) breast and (b) lung dose for each protocol, relative to the reference protocol, for both tasks.

Table 4.3: Image quality metrics and dose estimates for each protocol at approximately equivalent $\hat{A}_{FE}$ (≈ 0.96) for the 4-mm, 3.25 mg/mL task.

Protocol	CNR	Contrast [HU]	Noise [HU]	Breast dose [mGy]	Lung dose [mGy]
120 kV (ref)	0.72	33.2	46.3	36.8	34.5
120 kV Partial	0.74	31.8	43.3	30.3	43.2
120 kV TCM	0.70	33.1	47.3	34.6	30.9
120 kV Shield	0.78	29.1	37.3	61.8	70.2
80 kV	0.71	94.8	132.6	7.2	6.7
80 kV Partial	0.75	93.9	125.5	5.4	8.0

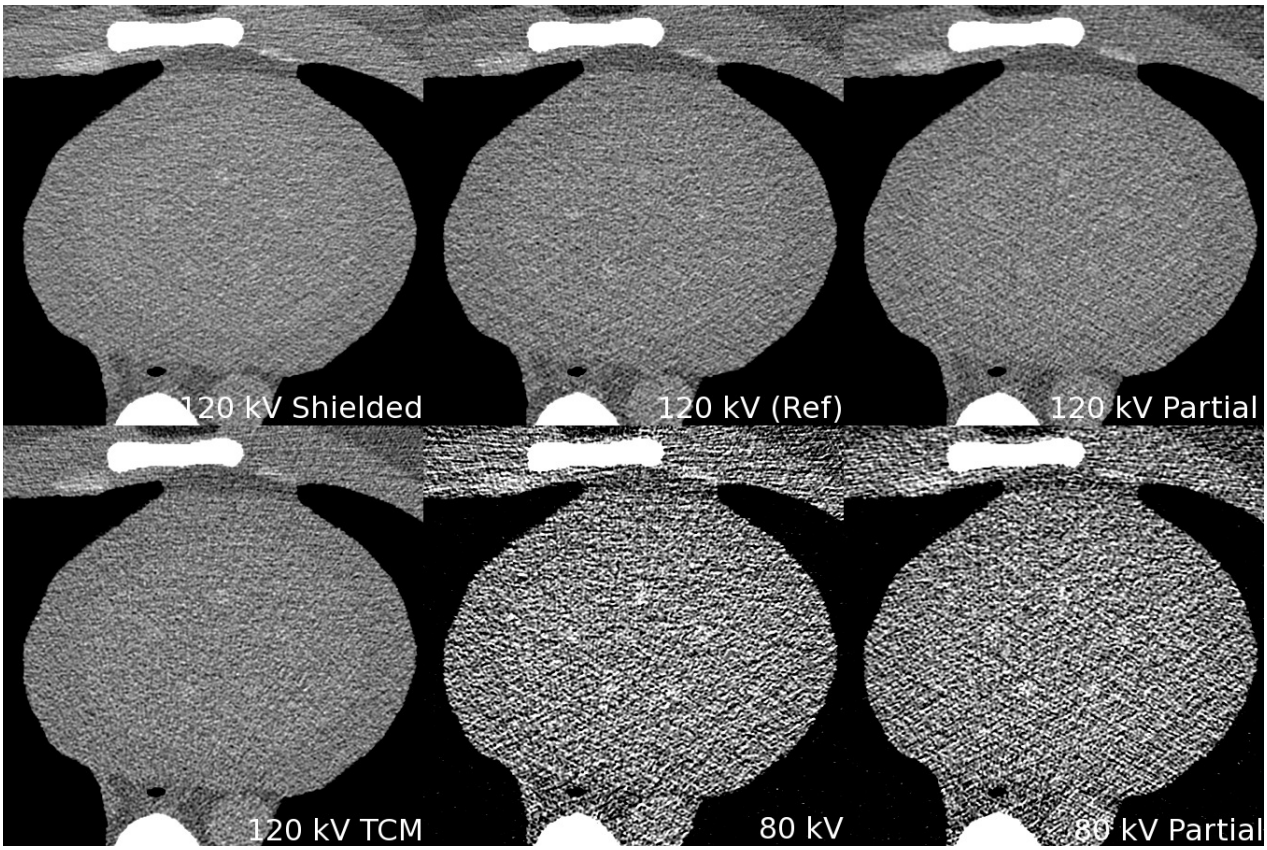

Figure 4.9: Example of a signal-present image for each protocol at equivalent $\hat{A}_{FE}$ (≈ 0.96). Window/level is 400/115 HU for the 120 kV images, and 400/280 HU for the 80 kV images.

Table 4.4: Image quality metrics and dose estimates for each protocol at approximately equivalent $\hat{A}_{FE}$ (≈ 0.96) for the 1-mm, 6.0 mg/mL task.

Protocol	CNR	Contrast [HU]	Noise [HU]	Breast dose [mGy]	Lung dose [mGy]
120 kV (ref)	2.45	56.3	23.0	148.9	140.4
120 kV Partial	2.40	53.7	22.4	115.8	166.0
120 kV TCM	2.35	54.6	23.3	144.9	129.7
120 kV Shield	2.75	56.0	20.0	214.5	242.2
80 kV	2.57	122.9	47.9	52.0	48.7
80 kV Partial	2.56	116.0	45.4	41.1	60.8

the breast by 67.8%. Figure 4.8b indicates that the 120 kV partial and shielded scans increased dose to the lung by 25.3% and 103%, respectively, while the TCM, 80 kV, and 80 kV partial scans reduced dose to the lung by 10.4%, 80.5%, and 76.7%, respectively. At this equivalent $\hat{A}_{FE}$ of 0.96, the 80 kV and 80 kV partial protocols yielded an approximate three-fold increase in both image noise (186% and

171%, respectively) and contrast (186% and 183%, respectively), while CNR across all protocols varied between a 1.4% decrease to an 8.6% increase relative to the reference protocol. An example of a signal-present image for each protocol for the 4-mm, 3.25 mg/mL task at this equivalent $\hat{A}_{FE}$ of approximately 0.96 is shown in Figure 4.9.

Table 4.4 lists values of CNR, contrast, noise, breast dose, and lung dose for each protocol at an equivalent $\hat{A}_{FE}$ of 0.96 for the 1-mm, 6.0 mg/mL task. Similar trends in these values were observed for the 1-mm task as for the 4-mm task, including dose performance, as seen in Figure 4.8. However, the 80 kV and 80 kV partial protocols demonstrated higher breast and lung dose savings for the 4-mm, 3.25 mg/mL task than for the 1-mm, 6.0 mg/mL task, and the shielded protocol showed a higher increase in breast and lung dose for the 4-mm, 3.25 mg/mL task than for the 1-mm, 6.0 mg/mL task, whereas the 120 kV partial and TCM protocols demonstrated more comparable dose savings to the breast and lung across tasks.

4.4 Discussion

Overall, for the 4-mm, 3.25 mg/mL task, the 80 kV and 80 kV partial angle protocols demonstrated the highest dose savings to the breast (80.5% and 85.3%, respectively), as well as to the lung (80.5% and 85.3%, respectively). This is due in large part to the approximate three-fold increase in contrast that resulted from the lowered kV (Table 4.3). We also saw a nearly three-fold increase in image noise (Table 4.3). In theory, equivalent $\hat{A}_{FE}$ across protocols represents equivalent signal detectability, and thus equivalent image quality for the specified (signal detection) task. In practice, certain characteristics of the signal (e.g., size, shape, and contrast) may be unknown a priori or may vary. In such cases, the increased noise that would result when acquiring images with the 80 kV or 80 kV partial protocols at the dose

required to achieve the reported breast dose savings could be deemed clinically unacceptable, as it may hinder the observer's ability to detect signals with characteristics other than those of that presented in this study. Some dose savings may still be realizable with reduced kV protocols even if the tube-current is increased to achieve a more desirable noise level. For example, Figure 4.10 displays an image produced by the 80 kV partial scan with the breast dose level indicated in Table 4.3, as well as an image produced by the 80 kV partial scan with a breast dose level five times greater, which would yield a 26.6% reduction in breast dose, a 21.2% increase in noise, and a 132% increase in CNR relative to the reference protocol, and an $\hat{A}_{FE}$ of 1.0.

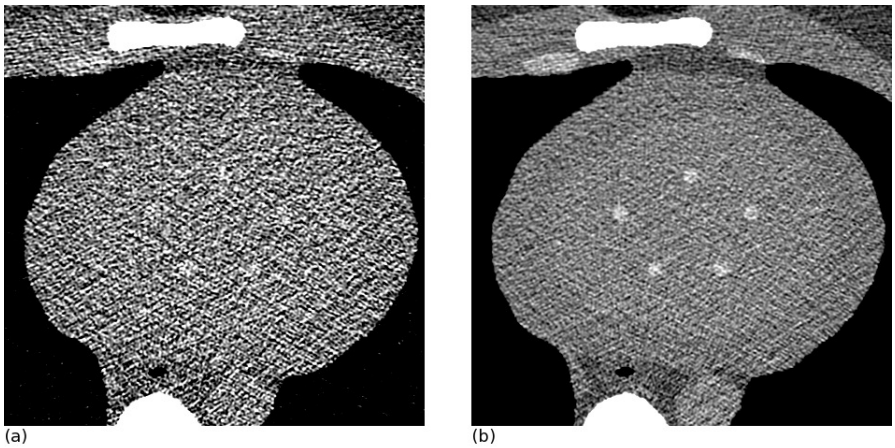

Figure 4.10: (a) A 4-mm, 3.25 mg/mL signal-present image using the 80 kV partial protocol with $\hat{A}_{FE} \approx 0.96$ (the same image as shown in Figure 4.9). This image yields 85.3% dose savings to the breast and 171% increase in noise relative to the reference protocol. (b) A 4-mm, 3.25 mg/mL signal-present image using the 80 kV partial protocol with five times the dose of that shown in (a), resulting in a 26.6% decrease in breast dose and 21.2% increase in noise, relative to the reference protocol, and an $\hat{A}_{FE}$ of 1.0. Both images are shown at a window/level of 400/280 HU.

The 120 kV partial protocol decreased breast dose by 17.6% for the 4-mm, 3.25 mg/mL task, but at the cost of 25.3% increased lung dose. The 120 kV partial protocol resulted in small decreases in both the noise (6.6%) and the contrast (4.3%) when maintaining equivalent $\hat{A}_{FE}$ to the reference protocol (Table 4.3).

Thus, the relative increase in performance versus breast dose was mostly attributable to the lack of direct exposure of the breasts to radiation during the partial scan protocol, for which the tube-current is turned off during the AP projections. Similarly, the increased tube-current during PA projections caused the decreased performance versus lung dose.

The 80 kV and 80 kV partial protocols showed greater reduction in breast and lung dose for the 4-mm task than for the 1-mm task, while the shielded protocol demonstrated increased breast and lung dose for the 4-mm task compared to the 1-mm task. This suggests that estimated percent changes in dose are task-dependent. We also note that the reported increase in breast and lung dose produced by the shielded protocol for both tasks is contrary to the original hypothesis that the breast shield may be used as a dose reduction method.

In general, the CNR curves indicate a similar relative ranking of protocol performance as the corresponding $\hat{A}_{FE}$ curves. At an $\hat{A}_{FE}$ of 0.96, the shielded protocol resulted in a 8.6% higher CNR than the 120 kV reference protocol for the 4-mm task (Table 4.3). If the CNR of the shielded protocol was adjusted to match that of the reference protocol, the shielded protocol would increase breast and lung dose by 42.2% and 72.4%, respectively, compared to the reference scan. In comparison, when both protocols maintained equivalent $\hat{A}_{FE}$ of 0.96, the shielded protocol increased breast and lung dose by 67.8% and 103%, respectively. A similar higher CNR for the shielded protocol relative to the reference protocol was observed for the 1-mm task (12.3%). CNR can be considered an incomplete metric in the sense that it does not account for noise correlations or image artifacts. For example, two signal-present images in which all properties are the same except for differing noise correlations can be shown to have the same CNR [98]. Unlike CNR, $\hat{A}_{FE}$ is a task-based metric, and both noise correlations and image artifacts affect its performance. Although it is not obviously visually apparent from Figure 4.7 or

Figure 4.9, it is possible that the streaking commonly associated with the use of shields [33, 35–37] altered the noise correlations in such a way as to result in a 8.6% (4-mm task) and 12.3% (1-mm task) increase in CNR at equivalent $\hat{A}_{FE}$ compared to the reference protocol. For all other cases, the CNR varied by less than 5.0% across all protocols in images with an $\hat{A}_{FE}$ of 0.96, and so $\hat{A}_{FE}$ and CNR resulted in similar estimates of dose performance (within 8.5% of one another) for these cases.

Although there are differences in signal detectability performance for the 4-mm and 1-mm signal-size tasks, as shown in Figure 4.4 and Figure 4.8, the plots show similar trends. This indicates a robustness of $\hat{A}_{FE}$ with regard to the particular task being investigated.

There are several advantages in using a signal detectability metric for signals at unknown locations compared with SNR calculations obtained for fixed signals with various other model observers (ideal, Hotelling, channelized Hotelling, non-prewhitening, etc.). The unknown-signal-location metrics compare the signal realizations with the extreme occurrences of false signal-like features that randomly occur in the background due to noise. On the other hand, the SNR metrics derived for known signal locations compare signal realizations with the fluctuations of a fixed signal-sized patch of image background, where extreme values are much less likely to occur and hence much less likely to be confounded with a signal. Therefore, the metrics derived for unknown signal locations are more sensitive to differences in noise levels and/or noise patterns. In addition, unlike the fixed signal location metrics, unknown-signal-location metrics take into account the clinically relevant case of correctly identifying the signal location.

By using nonparametric methods to estimate A_{FE}, we avoid the reliance on any specific models of or assumptions about the data. Further, while the calculation of ideal and quasi-ideal observer SNRs can require several hundreds or even thousands of signal-present and signal-absent images, which can be difficult to

obtain experimentally, the nonparametric estimator, $\hat{A}_{FE}$, can be calculated with fairly low statistical uncertainty using relatively few image samples (on the order of tens).

It is important to note that the reported dose and image quality estimates, and thus the reported percent changes in dose for each protocol, are specific to our simulation geometry, patient size, and reconstruction algorithm. For example, the noise increase quantified for the 80 kV protocols is expected to increase with patient size, and so additional work is required to study task-based detectability over a range of patient sizes. In addition, we used the same reconstruction algorithm for each protocol, however, it is unlikely that this algorithm (e.g., reconstruction kernel) was optimal across all protocols. Thus, additional work is required to study task-based detectability over a range of patient sizes, as well as to determine how the performance of such protocols may change when protocol-specific reconstruction kernels are used.

Chapter 5

Experimental Study of Optimal Energy Weighting in Energy-resolved CT using a CZT Detector

5.1 Introduction

In recent years, dedicated breast CT has received attention as a viable breast imaging modality [19–25], due to its expected lower costs than MRI, higher sensitivity than mammography, and lack of compression. One early study demonstrated the potential for obtaining high SNR images using dedicated breast CT at dose levels comparable to those used in mammography [19]. In addition, recent advances in photon-counting detector technology have motivated investigations [22–24] of the ability of energy-resolved CT to produce high-contrast diagnostic images, which could subsequently lead to reduced breast dose.

As discussed in Chapter 2, conventional energy-integrating detectors and photon-counting detectors use sub-optimal photon-weighting schemes. On the other hand, the additional spectral information provided by energy-resolving CT detectors, which are capable of sorting photons into discrete energy bins based on specified energy thresholds, can be used to produce optimally energy-weighted images. Previous work has suggested that optimal energy weighting provides increased CNR for energy-resolved CT compared to photon-counting and

conventional energy-integrating CT [22–24, 99, 100], which suggests the potential for reduced dose during conventional and dedicated breast CT. Improvements in CNR obtained from either optimal projection- or image-based weighting are expected to vary depending on the number of energy bins as well as the energy bin thresholds. This study experimentally investigated the effects of energy-bin selection on the improvement in CNR of projection-based and image-based weighted images relative to photon counting during energy-resolved CT. Further, we performed a preliminary investigation of the effects of spectral tailing on the performance of image-based and projection-based weighting, where spectral tailing is the non-ideal detector spectral response that causes high energy photons to be detected in lower energy bins [101]. The purpose of this study was to quantify the potential for image quality improvement and/or dose reduction for energy-resolved breast CT.

5.2 Materials and Methods

5.2.1 Overview

We acquired multi-energy CT data of a breast phantom containing a calcium contrast agent using our bench top energy-resolving CT system with a cadmium zinc telluride (CZT) detector. Images were obtained using both projection-based and image-based weighting for six different empirically chosen energy-bin combinations, and the CNR for each energy-bin combination for both weighting schemes was compared to that of an image obtained using photon-counting detection.

5.2.2 Bench Top Energy-resolving CT System

Our bench top energy-resolving CT system (Figure 5.1a) consists of a CZT detector (NEXIS, Nova R&D, Riverside, CA) with two pixel rows, each consisting of

128, 1×1 mm pixels. The detector pixel array is read out by the XENA chip (Nova R&D, Riverside, CA), which can sort detected photons above user-selected energy thresholds into a maximum of five bins per acquisition. The system also consists of a microfocal x-ray source (Fein-Focus-100.50, YXLON Intl, Hamburg, Germany) with a 3 micron effective focal spot. Cylindrical phantoms can be affixed to a rotating stage positioned between the x-ray source and CZT detector.

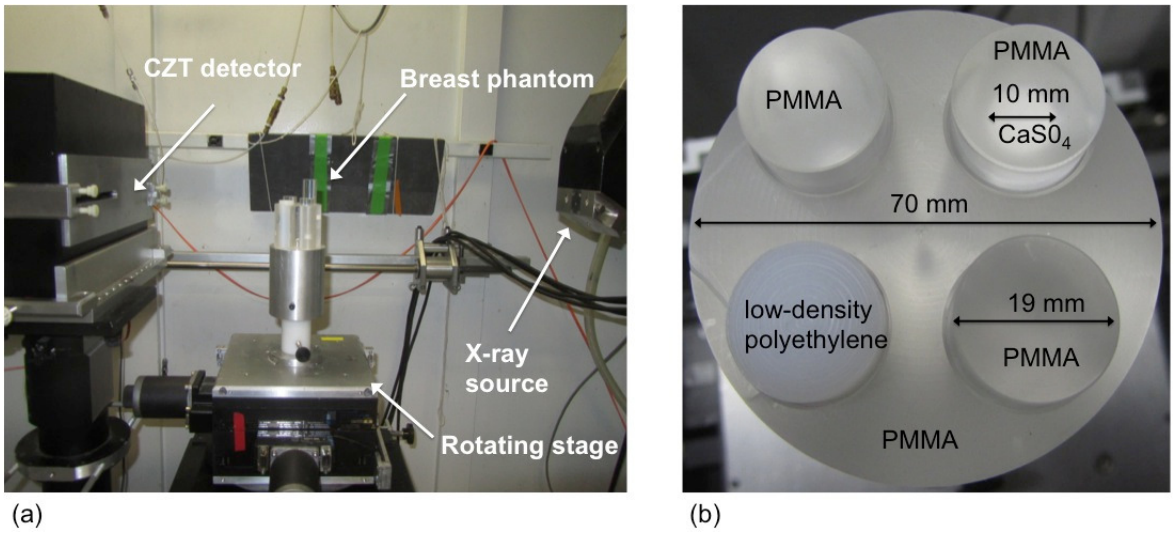

Figure 5.1: Experimental setup. (a) Bench-top system and (b) breast phantom.

5.2.3 Breast Phantom

A phantom representing the breast was constructed from a 70-mm diameter PMMA cylinder containing four, 19-mm-diameter cylindrical inserts composed of the following materials: 1) PMMA (chosen because of its similar density of 1.19 g/mm^2 to breast tissue) embedded with a 10 mm diameter calcium sulfate element, 2) low-density polyethylene (representing adipose tissue), 3) and 4) PMMA (Figure 5.1b).

5.2.4 System Calibration

The detector energy-bin threshold settings were calibrated by sweeping the threshold levels while acquiring transmission measurements through channels containing iodine solution and tungsten film. The k-edges of iodine and tungsten were identified from the transmission measurements and used as reference threshold settings.

Knowledge of the x-ray spectrum is required for calculating the optimal projection-based weights and for investigating the spectral tailing effects. The x-ray spectrum was estimated from transmission measurements through varying thicknesses of acrylic and Teflon. The spectrum was estimated using measurements of all counts above the lowest energy threshold (i.e, photon counting detection), and was therefore unaffected by spectral tailing. An expectation maximization algorithm [102] estimated the spectrum that maximized the likelihood of obtaining the transmission measurements.

5.2.5 Acquiring Projections

Two hundred projections of the phantom were acquired in step-and-shoot mode over 360° (1.8° per projection) at 100 kV and 4.4 mAs. Flat-field projections were collected at 100 kV and 4.4 mAs. The source-to-detector distance was 72 cm, and the source-to-isocenter distance was 40 cm. The raw photon count for each projection was measured using eight detector energy threshold bins: 25, 30, 35, 40, 45, 50, 60, and 70 keV. The total photon count between any two energy thresholds was obtained by calculating the difference in counts between those two threshold bins. Six combinations of energy bins (Table 5.1) were constructed from the raw data.

Table 5.1: Energy-bin combinations investigated for projection-based and image-based weighting

	Energy-bin Cutoff (keV)							
Bin Combination	1	2	3	4	5	6	7	8
A	25-30	30-35	35-40	40-45	45-50	50-60	60-70	>70
B	25-35	35-45	>45	-	-	-	-	-
C	25-35	35-50	>50	-	-	-	-	-
D	25-40	40-60	>60	-	-	-	-	-
E	25-30	30-35	35-40	40-50	50-60	60-70	>70	-
F	25-40	40-50	50-60	60-70	>70	-	-	-

5.2.6 Weighting and Reconstructing Images

For each energy-bin combination in Table 5.1, projections were flat-field corrected and images were obtained using projection-based and image-based weighting. In addition, we reconstructed a reference photon-counting image. All images were reconstructed with filtered backprojection. Details on the implementation of each weighting scheme are provided in the following subsections.

Photon-counting

A photon-counting detector weights each photon equally, independent of its energy. Therefore, the raw projections obtained from the lowest energy threshold (all photons with an energy above 25 keV) were log-normalized and reconstructed to obtain a photon-counting image.

Projection-based Weighting

Projection-based optimal energy weighting linearly combines the energy-bin data prior to log normalization, with the weights proportional to the expected contrast-to-noise variance ratios of the binned projection data[23, 103]. The optimal

energy-dependent weights for maximizing CNR between a projection through background material and a projection through background material with an embedded contrast element of length d are described in Equation 5.1 [104, 105]:

$$w_{\mathrm{PB}}(E) = \frac{1 - e^{-[\mu_{\mathrm{c}}(E) - \mu_{\mathrm{b}}(E)]d}}{1 + e^{-[\mu_{\mathrm{c}}(E) - \mu_{\mathrm{b}}(E)]d}} \tag{5.1}$$

where μ_{b} and μ_{c} are the energy-dependent linear attenuation coefficients of the background and contrast element materials, respectively. For each bin combination, we estimated the projection-based line integrals by weighting, combining, and then log-normalizing the projection data according to Equation 5.2[23]:

$$\tilde{\ell}_{\mathrm{PB}} = -\ln\left(\frac{\sum_{i=1}^{M}(w_{\mathrm{PB}i} \cdot \int_{E_i} N_0(E) e^{-\int \mu(l,E)\mathrm{d}l}\mathrm{d}E)}{\sum_{i=1}^{M} w_{\mathrm{PB}i} \cdot \int_{E_i} N_0(E)\mathrm{d}E}\right) \tag{5.2}$$

where M is the number of energy bins, E_i is the energy range of the ith bin, $N_0(E)$ is the number of incident photons at each energy, E, and $\mu(l, E)$ is the energy-dependent linear attenuation coefficient of the object along ray path, l. The weight of the ith bin, $w_{\mathrm{PB}i}$, was estimated using Equation 5.1 assuming the average attenuation coefficients, $\bar{\mu}_i$ as described in Equation 5.3:

$$\bar{\mu}_i = \int_{E_i} \mu(E) \cdot \Phi(E)\mathrm{d}E \tag{5.3}$$

where $\Phi(E)$ is the estimated normalized spectrum, as described in Section 5.2.4. Once the projection data were weighted, combined, and log-normalized, we used filtered backprojection reconstruction to obtain a projection-based weighted image for each energy-bin combination described in Table 5.1.

Image-based Weighting

Whereas projection-based weighting performs a linear combination of the energy-binned data prior to log normalization and reconstruction, image-based weighting performs a linear combination of the reconstructed energy-bin images[23]:

$$\text{Image}_{\text{combined}} = \sum_{i=1}^{M} w_{\text{IB}i} \cdot \text{Image}_{\text{i}} \tag{5.4}$$

The optimal weights are derived to maximize the CNR in the final reconstructed image. The optimal weight of the ith energy-bin image, $w_{\text{IB}i}$, is proportional to the contrast-to-noise-variance ratio (CNVR) of the binned images, and is calculated using Equation 5.5 [23]:

$$w_{\text{IB}i} = \frac{C_i/\sigma_i^2}{\sum_{n=1}^{M} C_n/\sigma_n^2} \tag{5.5}$$

where σ_i is the noise standard deviation and C_i the contrast in the ith energy-bin image. Image-based weights may also be calculated prior to reconstructing the energy-bin images [23]. Assuming the use of a linear reconstruction algorithm, such as filtered back projection, we can obtain an image equivalent to that described by Equation 5.4 by weighting and combining the energy-bin data after log-normalization but before reconstruction. This method requires only a single reconstruction of the combined energy-bin data, and the estimated image-based weighted line integral is [23]:

$$\tilde{\ell}_{IB} = \sum_{i=1}^{M} -w_{\text{IB}i} \ln \left(\frac{\int_{E_i} N_0(E) e^{-\int \mu(l,E)\mathrm{d}l} \mathrm{d}E}{\int_{E_i} N_0(E) \mathrm{d}E} \right) \tag{5.6}$$

We performed image-based weighting using the first method – linearly combining the reconstructed energy-bin images, as described in Equation 5.4. We

estimated the contrast using the following equation:

$$C_i = |\bar{\mu}_{c,i} - \bar{\mu}_{b,i}| \tag{5.7}$$

where $\bar{\mu}_{c,i}$ and $\bar{\mu}_{b,i}$ are the mean reconstructed attenuation coefficients within regions-of-interest (ROIs) of the calcium contrast element and background material, respectively, in the ith energy-bin image. Similarly, σ_i was estimated as the standard deviation within a background ROI in the ith enegy-bin image. Two reconstructed images for each energy bin were subtracted from one another to obtain an estimate of the standard deviation in images containing only noise, thus preventing ring artifacts, which are caused by discrepancies in the threshold calibrations between adjacent detector pixels, from contributing to the noise estimate. Similarly, the background and calcium ROIs were circular regions with equivalent diameters and at an equivalent radius from the phantom center, thereby assuring the same relative effects of ring artifacts on the means of both ROIs.

5.2.7 Image Quality Assessment

For each energy-bin combination, we measured the contrast, noise, and CNR for the projection-based and image-based weighted images relative to the photon-counting image. Contrast was estimated as the absolute value of the difference between the means of a background ROI and an ROI within the calcium element. Noise was estimated as the standard deviation of a background ROI. For all cases, two reconstructions were performed and the images subtracted to obtain a noise-only image and prevent ring artifacts from contributing to the noise estimate, as described in Section 5.2.6. Similarly, contrast and background ROIs were chosen carefully so that any ring artifacts would have the same effect on the means of both ROIs, also described in Section 5.2.6.

5.3 Results

Figure 5.2 shows the individual energy-binned images for bin combination E. In general, the lower energy bins demonstrate higher contrast and noise, while the higher energy bins demonstrate the opposite.

Table 5.2 lists the contrast, noise, and CNR for each energy-bin combination for projection-based and image-based weighting relative to those of the photon-counting image. The ratios of the CNR of the energy-weighted images over the photon-counting image ranged between 0.85 (bin combinations A and D) and 1.01 (bin combination C) for the projection-based weighted images and between 0.91 (bin combination 2) and 1.43 (bin combination E) for the image-based weighted images. In general, the projection-based weighted images showed relatively higher contrast at the expense of higher noise, resulting in lower CNR compared to the photon counting case for all but one of the six bin combinations. While the image-based weighted images demonstrated relatively lower contrast, they also produced lower noise, resulting in higher CNR than the photon counting case for five of the six bin combinations. These results are visually evident in Figure 5.3, which displays images reconstructed using projection-based and image-based weighting for energy-bin combinations 3 and 5, along with the photon-counting image.

Table 5.2: Results for projection-based and image-based weighted images. Contrast, noise, and CNR are reported relative to the photon-counting case.

Projection-Based Weighting				Image-Based Weighting			
Bin Combination	Contrast	Noise (stdev)	CNR	Bin Combination	Contrast	Noise (stdev)	CNR
A	1.11	1.30	0.85	A	0.82	0.79	1.04
B	0.94	1.06	0.89	B	0.79	0.87	0.91
C	1.01	1.00	1.01	C	0.80	0.67	1.20
D	1.15	1.35	0.85	D	0.92	0.69	1.33
E	1.10	1.18	0.93	E	0.85	0.59	1.43
F	1.01	1.06	0.95	F	0.75	0.65	1.15

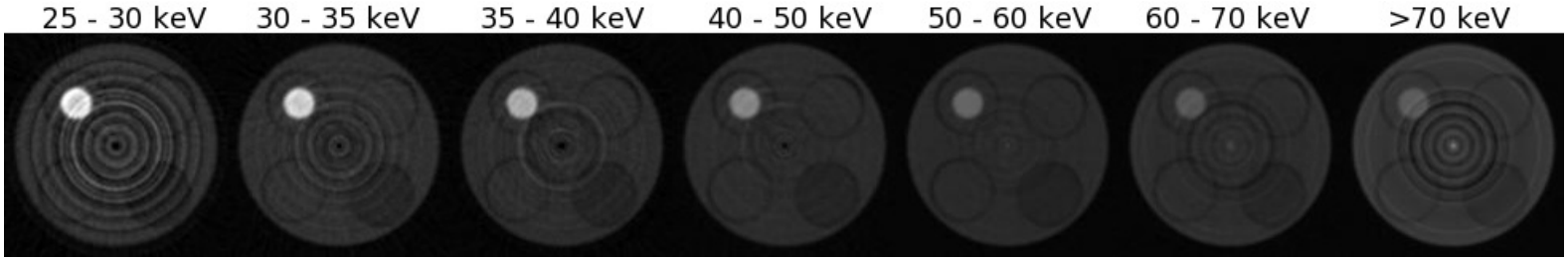

Figure 5.2: Individual energy-binned images for bin combination E. All images are shown at the same window (7800 HU) and level (2700 HU).

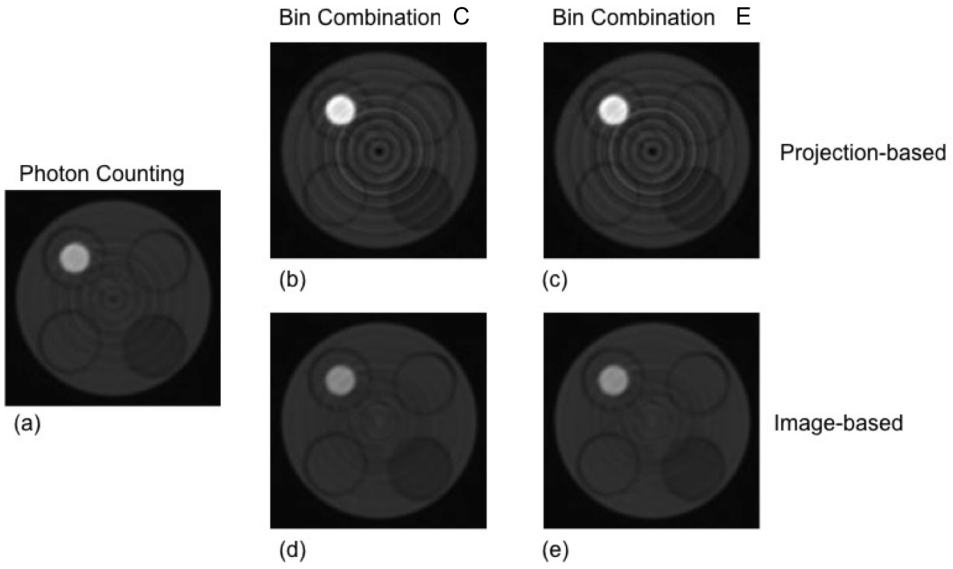

Figure 5.3: Reconstructed energy-weighted image. Shown are images reconstructed using (a) photon-counting; (b) projection-based weighting with bin combination C; (c) projection-based weighting with bin combination E; (d) image-based weighting with bin combination C; (e) image-based weighting with bin combination E. All images have the same window (6000 HU) and level (1800 HU).

Figure 5.4a plots the CNR for each bin combination for projection-based and image-based weighting relative to photon-counting. The differences in the shape of the curves suggests that an optimal bin combination (in terms of CNR) depends on the type of weighting used. Figure 5.4b plots the normalized photon-counting, projection-based, and image-based weights for bin combination E. For this particular bin combination, the projection-based weighting gives more weight to the lower energy photons, whereas the image-based weighting gives more weight to the higher energy photons.

In theory, both image-based and projection-based weighting should provide CNR that is at least as good as photon-counting weighting. As seen in Table 5.2, the CNR was equal to or lower than the photon-counting CNR for all projection-based weighted images and for one image-based weighted image. This discrepancy is likely caused by the fact that the theoretically calculated weights in

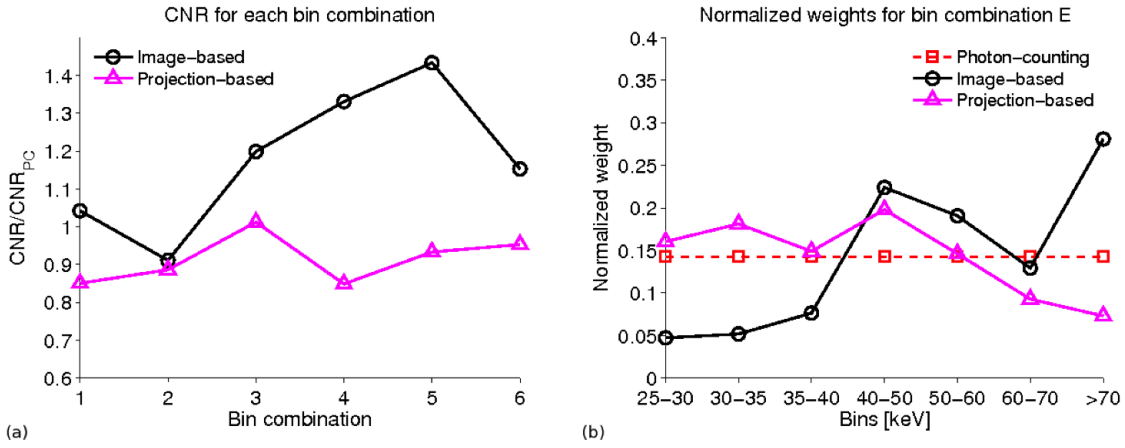

Figure 5.4: CNR and normalized weights. (a) CNR for each bin combination of projection-based and image-based weighting, relative to photon-counting. (b) Normalized photon-counting, image-based, and projection-based weights for bin combination E.

the case of projection-based weighting may not reflect the measured CNVR in the energy-bin projection data. To quantify the magnitude of spectral tailing in the measured data, Figure 5.5 plots the number of photons expected at each energy bin based on the estimated 100 kV spectrum (whose measurement was minimally affected by spectral tailing, as described in Section 5.2.4) and the number of photons measured in each bin of a flat-field projection. The lowest two energy bins detected nearly 4.5 and 2.5 times the number of expected photons, respectively, while the highest three energy bins detected between 0.5 and 0.83 the number of expected photons, indicating the presence of spectral tailing. Due to the presence of more higher energy photons, spectral tailing reduces the contrast in the lower energy bins. On the other hand, the increase in the total number of photons in the bin leads to a reduction in noise. The inverse is true for the higher energy bins.

5.4 Discussion

Previous work suggested similar CNR performance for optimal projection- and image-based weights [23, 24]. Furthermore, previous work also predicted that optimal weighting improves contrast compared to photon-counting weighting, due to the increased weighting of the low-energy bins [22–24, 99]. In our preliminary experimental results, projection-based weighting provided reduced CNR compared to photon-counting, and the images resulting from image-based weighting had increased CNR but reduced contrast compared to photon counting. We believe these discrepancies are due to the non-ideal spectral response in the CZT detector, which leads to spectral tailing effects, i.e., higher energy photons being counted in lower energy bins (Figure 5.5). Results suggest that these spectral tailing effects generally reduce the CNR in images reconstructed with projection-based weighting. On the other hand, image-based weighting was able to produce improved CNR despite the spectral tailing effects. This is likely due to the fact that the projection-based weights estimated in this work were based on the theoretical signal properties, while the image-based weights were estimated from the measured image

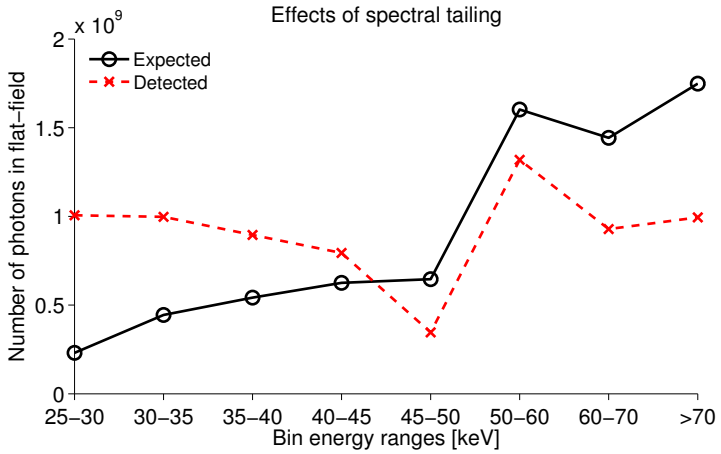

Figure 5.5: Spectral tailing effects. The number of detected photons in the flat-field projection for each energy bin and the number of expected photons in each energy bin for the estimated 100 kV spectrum

data (i.e., noise and contrast estimated directly from the binned images). Thus, the image-based weights may be adjusted to at least partially account for such system non-idealities. The results of the projection-based weighting could be improved by calculating the weights based on estimates of contrast and noise obtained directly from the projection data, although this measurement may be challenging in practice. The reduced ring artifacts in the image-based weighted images are likely caused by the increased weighting of high-energy bins, due to spectral tailing, compared to the projection-based weights. Work is in progress to develop methods to correct the spectral tailing response [24, 101, 106–109] to provide further CNR improvements for energy weighting with energy-resolving detectors.

Overall, the results indicate that image-based weighting during energy-resolved CT improves CNR and thus shows potential for reducing breast dose during procedures such as dedicated breast CT. Further studies are required to investigate the performance of each weighting scheme when combined with spectral tailing correction.

Chapter 6

Conclusions and Future Directions

The two overall goals of this work were (1) to quantify the effectiveness of techniques intended to reduce dose to the breast during CTCA scans with respect to a task-based image quality metric, and (2) to evaluate the effectiveness of optimal energy weighting in improving CNR, and thus the potential for reducing breast dose, during energy-resolved dedicated breast CT.

With respect to the first goal, we used the task-based signal-detectability metric, $\hat{A}_{FE}$, to compare the performance of two signal-detection tasks for five dose reduction protocols over a range of breast dose levels. Our results indicated that for both the small-diameter/high-contrast and large-diameter/medium-contrast tasks, the 80 kV and 80 kV partial protocols demonstrated the greatest reduction to breast dose. However, in clinical applications, due to the more complex nature of the tasks, the subsequent increase in image noise may be considered too large. In these situations, tube output for these protocols can be adjusted to achieve a more desirable noise level at a lesser reduction in dose.

The "quality" of an image used for diagnostic purposes should be assessed in the context of a specified diagnostic task. Because task-based image quality is fundamentally linked to dose, it should not be surprising that dose reduction estimates for a given acquisition protocol vary with the task. Indeed, we have shown that relatively greater dose reduction is achievable for a task involving detection of large-diameter/medium-contras signals compared to small-diameter/high-contrast

signals. An interesting follow-up study would be to investigate how dose reduction estimates vary as a function of both signal size and signal contrast (and perhaps even signal shape). In addition, it would be interesting to investigate how well $\hat{A}_{FE}$ correlates to human observers.

The dose database we developed to facilitate our breast and lung dose estimates can be used for future dose and image quality studies and is already publicly available online. While the dose tables are currently patient- and geometry-specific, similar procedures to those outlined in Chapter 3 can be used to expand the database to include male and female phantoms of various sizes and ages, as well as to include dose tables for cross-sectional slabs to facilitate organ-dose or effective-dose estimates for arbitrary field-of-views and trajectory types.

With respect to our second goal, we found that the non-ideal spectral response of our detector reduced the CNR for the projection-based weighted images, while image-based weighting was able to provide improved CNR for five out of the six investigated bin combinations, despite this non-ideal response. This indicates the potential for image-based weighting to reduce breast dose during dedicated breast CT, even in the presence of some non-ideal effects. Greater improvements in the CNR for both image-based and projection-based weighting are expected in conjunction with methods to reduce spectral tailing. In addition to correcting for non-ideal effects of the detector, further studies can be performed investigating optimizing the x-ray spectrum and corresponding energy bin thresholds with respect to CNR.

One may wonder why after spending a considerable amount of time stressing the importance of using task-based metrics when assessing image quality, we seemingly ignore our own advice through our use of CNR during the experimental portion of this work. While it may be fairly simple on a commercial scanner to experimentally collect the relatively few image samples required to estimate a

metric such as $\hat{A}_{FE}$, it is simply not yet feasible to do so for each bin combination using our bench-top system. Nonetheless, both contrast and noise play a crucial role in task-based image quality, and thus CNR was used in this preliminary study to compare performance of optimal and sub-optimal energy-weighting methods. Future work may consider the use of simulations, or, if possible, experimentally acquiring larger data sets, to investigate task-based image quality for optimal energy-weighting methods used during energy-resolved CT.

Overall, we demonstrated the potential for 80 kV, 80 kV partial, 120 kV partial, and 120 kV tube-current modulated protocols to reduce dose to the breast during CTCA, and we further demonstrated that the magnitude of the dose reduction is task-dependent. Finally, we have demonstrated the ability of optimal image-based weighting to improve CNR compared to photon-counting during energy-resolved dedicated breast CT, thereby demonstrating its potential for reducing breast dose.

BIBLIOGRAPHY

[1] American Cancer Society, *Breast Cancer Facts & Figures 2011-2012*, American Cancer Society, Atlanta, GA, 2011.

[2] American Cancer Society, *Cancer Facts & Figures 2013*, American Cancer Society, Atlanta, GA, 2013.

[3] Committee on Breast Cancer and the Environment: The Scientific Evidence, Research Methodology, and Future Directions, Board on Health Care Services, Board on Health Sciences Policy, Institute of Medicine of The National Academies, *Breast Cancer and the Environment: A Life Course Approach*, The National Academies Press, Washington, DC, 2011.

[4] R. Smith-Bindman, "Is computed tomography safe?," *New England Journal of Medicine* **363**(1), pp. 1–4, 2010.

[5] H. E. Davies, C. G. Wathen, and F. V. Gleeson, "Risks of exposure to radiological imaging and how to minimise them," *British Medical Journal* **342**, pp. 589–593, 2011.

[6] M. Tokunaga, C. E. Land, T. Yamamoto, M. Asano, S. Tokuoka, H. Ezaki, and I. Nishimori, "Incidence of female breast cancer among atomic bomb survivors, hiroshima and nagasaki, 1950-1980," *Radiation Research* **112**, pp. 243–272, 1987.

[7] Committee to Assess Health Risks from Exposure to Low Levels of Ionizing Radiation, Board on Radiation Effects Research, Division of Earth and Life Sciences, National Research Council of The National Academies, *Health Risks from Exposure to Low Levels of Ionizing Radiation: BEIR VII Phase 2*, The National Academies Press, Washington, DC, 2006.

[8] A. J. Einstein, M. J. Henzlova, and S. Rajagopalan, "Estimating risk of cancer associated with radiation exposure from 64-slice computed tomography coronary angiography," *Journal of the American Medical Association* **298**(3), pp. 317–323, 2007.

[9] R. Smith-Bindman, J. Lipson, R. Marcus, K.-P. Kim, M. Mahesh, R. Gould, A. Berrington de Gonzalez, and D. L. Miglioretti, "Radiation Dose Associated With Common Computed Tomography Examinations and the Associated Lifetime Attributable Risk of Cancer," *Archives of Internal Medicine* **169**(22), p. 2078, 2009.

[10] J. D. Boice and M. R. R, "Breast cancer in women after repeated fluoroscopic examinations of the chest," *Journal of the National Cancer Institute* **59**, pp. 823–832, 1977.

[11] R. E. Shore, L. H. Hempelmann, E. Kowaluk, P. S. Mansur, B. S. Pasternack, R. E. Albert, and G. E. Haughie, "Breast neoplasms in women treated with x-rays for acute postpartum mastitis," *Journal of the National Cancer Institute* **59**, pp. 813–822, 1977.

[12] International Commission on Radiological Protection, *ICRP Publication 103: The 2007 Recommendations of the International Commission on Radiological Protection*, vol. 37 of *Annals of the ICRP*, Elsevier, Oxford, UK, 2007.

[13] F. A. Mettler Jr, B. R. Thomadsen, M. Bhargavan, D. B. Gilley, J. E. Gray, J. A. Lipoti, J. McCrohan, T. T. Yoshizumi, and M. Mahesh, "Medical Radiation Exposure in the U.S. in 2006: Preliminary Results," *Health Physics* **95**(5), pp. 502–507, 2008.

[14] D. B. Kopans, "The positive predictive value of mammography," *American Journal of Roentgenology* **158**, pp. 521–526, 1992.

[15] S. J. Lord, W. Lei, P. Craft, J. N. Cawson, I. Morris, S. Walleser, A. Griffiths, S. Parker, and N. Houssami, "A systematic review of the effectiveness of magnetic resonance imaging (MRI) as an addition to mammography and ultrasound in screening young women at high risk of breast cancer," *European Journal of Cancer* **43**, pp. 1905–1917, 2007.

[16] E. Warner, D. Plewes, and R. Shumak, "Comparison of Breast Magnetic Resonance Imaging, Mammography, and Ultrasound for Surveillance of Women at High Risk for Hereditary Breast Cancer," *Journal of Clinical Oncology* **19**, pp. 3524–3531, 2001.

[17] Q. Fang, J. Selb, S. Carp, and G. Boverman, "Combined Optical and X-ray Tomosynthesis Breast Imaging," *Radiology* **258**(1), pp. 89–97, 2011.

[18] I. Andersson, D. M. Ikeda, S. Zackrisson, M. Ruschin, T. Svahn, P. Timberg, and A. Tingberg, "Breast tomosynthesis and digital mammography: a comparison of breast cancer visibility and BIRADS classification in a population of cancers with subtle mammographic findings," *European radiology* **18**(12), pp. 2817–2825, 2008.

[19] J. M. Boone, T. R. Nelson, K. K. Lindfors, and J. A. Seibert, "Dedicated breast CT: radiation dose and image quality evaluation," *Radiology* **221**, pp. 657–667, 2001.

[20] R. L. McKinley, M. P. Tornai, E. Samei, and M. L. Bradshaw, "Simulation study of a quasi-monochromatic beam for x-ray computed mammotomography," *Medical Physics* **31**, pp. 800–813, 2004.

[21] S. J. Glick, S. Thacker, X. Gong, and B. Liu, "Evaluating the impact of x-ray spectral shape on image quality in flat-panel CT breast imaging," *Medical Physics* **34**, pp. 5–24, 2007.

[22] P. M. Shikhaliev, "Energy-resolved computed tomography: first experimental results," *Physics in Medicine and Biology* **53**(20), pp. 5595–5613, 2008.

[23] T. G. Schmidt, "Optimal "image-based" weighting for energy-resolved CT," *Medical Physics* **36**, pp. 3018–3027, 2009.

[24] K. Kalluri, S. J. Glick, and M. Mahd, "SNR Improvement in Dedicated Breast CT using Energy Weighting with Photon Counting Detectors," in *37th Annual Northeast Bioengineering Conference (NEBEC)*, pp. 1–2, IEEE, 2011.

[25] P. M. Shikhaliev and S. G. Fritz, "Photon counting spectral CT versus conventional CT: comparative evaluation for breast imaging application," *Physics in Medicine and Biology* **56**, pp. 1905–1930, 2011.

[26] D. Chesler, S. Riederer, and N. Pelc, "Noise due to photon counting statistics in computed X-ray tomography," *Journal of computer assisted tomography* **1**(1), pp. 64–74, 1977.

[27] J. H. Hubbell and S. M. Seltzer, "Tables of x-ray mass attenuation coefficients and mass-energy absorption coefficients." `http://physics.nist.gov/PhysRefData/XrayMassCoef/tab3.html`, 1996.

[28] C. H. McCollough and B. A. Schueler, "Calculation of effective dose," *Medical Physics* **27**(5), p. 828, 2000.

[29] D. Schauer, ed., *Report No. 160: Ionizing Radiation Exposure of the Population of the United States*, National Council on Radiation Protection and Measurements (NCRP), Bethesda, MD, 2009.

[30] L. M. Hurwitz, R. E. Reiman, T. T. Yoshizumi, P. C. Goodman, G. Toncheva, G. Nguyen, and C. Lowry, "Radiation dose from contemporary cardiothoracic multidetector CT protocols with an anthropomorphic female phantom: implications for cancer induction," *Radiology* **245**(3), pp. 742–750, 2007.

[31] L. Yu, X. Liu, S. Leng, J. M. Kofler, J. C. Ramirez-Giraldo, M. Qu, J. Christner, J. G. Fletcher, and C. H. McCollough, "Radiation dose reduction in computed tomography: techniques and future perspective," *Imaging in Medicine* **1**(1), pp. 65–84, 2009.

[32] M. S. Pearce, J. A. Salotti, M. P. Little, K. McHugh, C. Lee, K.-P. Kim, N. L. Howe, C. M. Ronckers, P. Rajaraman, A. W. Craft, L. Parker, and A. Berrington de Gonzalez, "Radiation exposure from CT scans in childhood and subsequent risk of leukaemia and brain tumours: a retrospective cohort study," *The Lancet* , 2012.

[33] L. M. Hurwitz, T. T. Yoshizumi, P. C. Goodman, R. C. Nelson, G. Toncheva, G. B. Nguyen, C. Lowry, and C. Anderson-Evans, "Radiation Dose Savings for Adult Pulmonary Embolus 64-MDCT Using Bismuth Breast Shields, Lower Peak Kilovoltage, and Automatic Tube Current Modulation," *American Journal of Roentgenology* **192**(1), pp. 244–253, 2009.

[34] S. V. Vollmar and W. A. Kalender, "Reduction of dose to the female breast as a result of spectral optimisation for high-contrast thoracic CT imaging: a phantom study," *British Journal of Radiology* **82**, pp. 920–929, 2009.

[35] S. V. Vollmar and W. A. Kalender, "Reduction of dose to the female breast in thoracic CT: a comparison of standard-protocol, bismuth-shielded, partial and tube-current-modulated CT examinations," *European Radiology* **18**(8), pp. 1674–1682, 2008.

[36] J. Wang, X. Duan, J. A. Christner, S. Leng, L. Yu, and C. H. McCollough, "Radiation dose reduction to the breast in thoracic CT: Comparison of bismuth shielding, organ-based tube current modulation, and use of a globally decreased tube current," *Medical Physics* **38**(11), pp. 6084–6092, 2011.

[37] J. Geleijns, M. Salvado Artells, W. J. H. Veldkamp, M. López Tortosa, and A. Calzado Cantera, "Quantitative assessment of selective in-plane shielding of tissues in computed tomography through evaluation of absorbed dose and image quality," *European Radiology* **16**(10), pp. 2334–2340, 2006.

[38] K. D. Hopper, S. H. King, M. E. Lobell, T. R. TenHave, and J. S. Weaver, "The breast: in-plane x-ray protection during diagnostic thoracic CT–shielding with bismuth radioprotective garments.," *Radiology* **205**(3), pp. 853–858, 1997.

[39] B. L. Fricke, L. F. Donnelly, D. P. Frush, T. Yoshizumi, V. Varchena, S. A. Poe, and J. Lucaya, "In-Plane Bismuth Breast Shields for Pediatric CT: Effects on Radiation Dose and Image Quality Using Experimental and Clinical Data," *American Journal of Roentgenology* **180**, pp. 407–411, 2003.

[40] A. B. of Directors, "Use of Bismuth Shielding for the Purpose of Dose Reduction in CT Scanning." (Available at `http://www.aapm.org/publicgeneral/BismuthShielding.pdf`), 2012.

[41] E. Angel, N. Yaghmai, C. M. Jude, J. J. Demarco, C. H. Cagnon, J. G. Goldin, A. N. Primak, D. M. Stevens, D. D. Cody, C. H. McCollough, and M. F. McNitt-Gray, "Monte Carlo simulations to assess the effects of tube current modulation on breast dose for multidetector CT.," *Physics in Medicine and Biology* **54**(3), pp. 497–512, 2009.

[42] International Commission on Radiation Units and Measurements, *ICRU Report 54: Medical Imaging - The Assessment of Image Quality*, ICRU, 1996.

[43] H. H. Barrett, "Objective assessment of image quality: effects of quantum noise and object variability," *Journal of the Optical Society of America A* **7**(7), pp. 1266–1278, 1990.

[44] H. H. Barrett and K. J. Myers, *Foundations of Image Science*, Wiley, 2004.

[45] S. Richard, X. Li, G. Yadava, and E. Samei, "Predictive models for observer performance in CT: applications in protocol optimization," in *Proceedings of SPIE - Medical Imaging 2011: Physics of Medical Imaging*, N. J. Pelc, E. Samei, and R. M. Nishikawa, eds., **7961**, SPIE, (Lake Buena Vista, FL), 2011.

[46] R. Zeng, N. Petrick, M. A. Gavrielides, and K. J. Myers, "Approximations of noise covariance in multi-slice helical CT scans: impact on lung nodule size estimation.," *Physics in Medicine and Biology* **56**(19), pp. 6223–6242, 2011.

[47] A. R. Pineda and J. H. Siewerdsen, "Analysis of image noise in 3D cone-beam CT: Spatial and Fourier domain approaches under conditions of varying stationarity," *Proceedings of SPIE* **6913**, 2008.

[48] A. R. Pineda, D. J. Tward, A. Gonzalez, and J. H. Siewerdsen, "Beyond noise power in 3D computed tomography: The local NPS and off-diagonal elements of the Fourier domain covariance matrix," *Medical Physics* **39**(6), pp. 3240–3252, 2012.

[49] C. C. Brunner, S. F. Abboud, C. Hoeschen, and I. S. Kyprianou, "Signal detection and location-dependent noise in cone-beam computed tomography using the spatial definition of the Hotelling SNR," *Medical Physics* **39**(6), pp. 3214–3228, 2012.

[50] C. Brunner, S. Hurowitz, S. Abboud, C. Hoeschen, and I. Kyprianou, "Noise characterization of computed tomography using the covariance matrix," *Proceedings of SPIE* **7622**, 2010.

[51] K. H. Chang, W. Lee, D. M. Choo, C. S. Lee, and Y. Kim, "Dose reduction in CT using bismuth shielding: measurements and Monte Carlo simulations," *Radiation Protection Dosimetry* **138**(4), pp. 382–388, 2010.

[52] C. Coursey, D. P. Frush, T. Yoshizumi, G. Toncheva, G. Nguyen, and S. B. Greenberg, "Pediatric Chest MDCT Using Tube Current Modulation: Effect on Radiation Dose with Breast Shielding," *American Journal of Roentgenology* **190**(1), pp. W54–W61, 2008.

[53] Imaging Performance Assessment of CT Scanners Group, "ImPACT CT patient dosimetry calculator." (Available at `http://www.impactscan.org`), 2006.

[54] "penEasy software." (Available at `http://inte.upc.edu/downloads`), 2010.

[55] "penEasy Imaging software." (Available at `http://code.google.com/p/peneasy-imaging`), 2010.

[56] J. Sempau, A. Badal, and L. Brualla, "A PENELOPE-based system for the automated Monte Carlo simulation of clinacs and voxelized geometries-application to far-from-axis fields.," *Medical Physics* **38**(11), pp. 5887–5895, 2011.

[57] Nuclear Energy Agency, Organization for Economic Co-operation and Development, *PENELOPE-2006: A code system for Monte Carlo simulation of electron and photon transport*, (Barcelona, Spain), 2006.

[58] A. Christ, W. Kainz, E. G. Hahn, K. Honegger, M. Zefferer, E. Neufeld, W. Rascher, R. Janka, W. Bautz, J. Chen, B. Kiefer, P. Schmitt, H.-P. Hollenbach, J. Shen, M. Oberle, D. Szczerba, A. Kam, J. W. Guag, and N. Kuster, "The Virtual Family–development of surface-based anatomical models of two adults and two children for dosimetric simulations.," *Physics in Medicine and Biology* **55**(2), pp. N23–N38, 2010.

[59] International Commission on Radiological Protection (ICRP), *Annals of the ICRP, Publication 110: Adult Reference Computational Phantoms*, vol. 39, Elsevier, 2009.

[60] H. Woodard and D. White, "The composition of body tissues," *British Journal of Radiology* **59**(708), pp. 1209–1219, 1986.

[61] M. Cristy and K. F. Eckerman, *Specific absorbed fractions of energy at various ages from internal photon sources*, vol. I-VII, ORNL Report No. TM-8381, Oak Ridge National Laboratory, Oak Ridge, TN, 1987.

[62] Food and Drug Administration (FDA), "Code of Federal Regulations 21 CFR 1020.33(b)(6)." `http://www.accessdata.fda.gov/scripts/cdrh/cfdocs/cfcfr/CFRSearch.cfm?FR=1020.33`, April 2011.

[63] A. J. Einstein, C. D. Elliston, A. E. Arai, M. Y. Chen, R. Mather, G. D. N. Pearson, R. L. DeLaPaz, E. Nickoloff, A. Dutta, and D. J. Brenner, "Radiation Dose from Single-Heartbeat Coronary CT Angiography Performed with a 320-Detector Row Volume Scanner," *Radiology* **254**(3), pp. 698–706, 2010.

[64] E. J. Salomon, J. Barfett, P. W. A. Willems, S. Geibprasert, S. Bacigaluppi, and T. Krings, "Dynamic CT Angiography and CT Perfusion Employing a 320-Detector Row CT," *Clinical Neuroradiology* **19**(3), pp. 187–196, 2009.

[65] S. Abboud, R. J. Jennings, S. H. Stern, M. Mahesh, and I. Kyprianou, "A method to characterize the shaped filtration associated with angle-dependent spectra of clinical computed tomography (ct) systems," *Submitted to Medical Physics* , 2011.

[66] S. E. McKenney, A. Nosratieh, D. Gelskey, K. Yang, S.-y. Huang, L. Chen, and J. M. Boone, "Experimental validation of a method characterizing bow tie filters in CT scanners using a real-time dose probe," *Medical Physics* **38**(3), pp. 1406–1415, 2011.

[67] C. Lee, C. Lee, A. P. Shah, and W. E. Bolch, "An assessment of bone marrow and bone endosteum dosimetry methods for photon sources," *Physics in Medicine and Biology* **51**, pp. 5391–5407, 2006.

[68] M. Rosenstein, *Organ Doses in Diagnostic Radiology*, HEW Publication, FDA 76-8030, Food and Drug Administration, Rockville, MD, 1976.

[69] A. C. Turner, M. Zankl, J. J. DeMarco, C. H. Cagnon, D. Zhang, E. Angel, D. D. Cody, D. M. Stevens, C. H. McCollough, and M. F. McNitt-Gray, "The feasibility of a scanner-independent technique to estimate organ dose from MDCT scans: Using CTDI to account for differences between scanners," *Medical Physics* **37**(4), pp. 1816–1825, 2010.

[70] J. Boone, "The trouble with CTDI100," *Medical Physics* **34**(4), pp. 1364–1371, 2007.

[71] International Electrotechnical Commission, *IEC Publication 60601: Medical Electrical Equipment, part 2-44: particular requirements for the safety of x-ray equipment for computed tomography*, International Electrotechnical Commission, Geneva, Switzerland, 2002.

[72] K. Cranley, B. Gilmore, G. W. A. Fogarty, and L. Desponds, *Report 78: Catalogue of Diagnostic X-ray Spectra and Other Data*, The Institute of Physics and Engineering in Medicine (IPEM), 1997.

[73] A. C. Turner, D. Zhang, M. Khatonabadi, M. Zankl, J. J. DeMarco, C. H. Cagnon, D. D. Cody, D. M. Stevens, C. H. McCollough, and M. F. McNitt-Gray, "The feasibility of patient size-corrected, scanner-independent organ dose estimates for abdominal CT exams," *Medical Physics* **38**(2), pp. 820–829, 2011.

[74] F. Rupcich, I. Kyprianou, A. Badal, and T. Gilat-Schmidt, "Energy deposition in the breast during CT scanning: quantification and implications for dose reduction," in *Proceedings of SPIE - Medical Imaging 2011: Physics of Medical Imaging*, N. J. Pelc, E. Samei, and R. M. Nishikawa, eds., **7961**, SPIE, (Lake Buena Vista, FL), 2011.

[75] M. Gies, W. Kalender, H. Wolf, and C. Suess, "Dose reduction in CT by anatomically adapted tube current modulation. I. Simulation studies," *Medical Physics* **26**(11), pp. 2235–2247, 1999.

[76] F. Rupcich, A. Badal, I. Kyprianou, and T. G. Schmidt, "A database for estimating organ dose for coronary angiography and brain perfusion CT scans for arbitrary spectra and angular tube current modulation," *Medical Physics* **39**(9), pp. 5336–5346, 2012.

[77] D. Jones and P. Shrimpton, *Survey of CT practice in the UK Part 3; normalised organ doses calculated using the Monte Carlo techniques, NRPB-R250*, National Radiological Protection Board, Oxon, United Kingdom, 1991.

[78] M. Zankl, W. Panzer, and G. Drexler, *The calculation of Dose from external photon exposures using reference human phantoms and Monte Carlo methods. Part VI: Organ doses from computed tomographic examinations, GSF-Bericht 30/91*, GSFForschungszentrum fur Umwelt und Gesundtheit, Institut fur Strahlenschutz, Neuherberg, Germany, 1991.

[79] G. Chodick, N. Bekiroglu, M. Hauptmann, B. H. Alexander, D. M. Freedman, M. M. Doody, L. C. Cheung, S. L. Simon, R. M. Weinstock, A. Bouville, and A. J. Sigurdson, "Risk of Cataract after Exposure to Low Doses of Ionizing Radiation: A 20-Year Prospective Cohort Study among US Radiologic Technologists," *American Journal of Epidemiology* **168**(6), pp. 620–631, 2008.

[80] E. Nakashima, K. Neriishi, and A. Minamoto, "A Reanalysis of atomic-bomb cataract data, 2000-2002: a threshold analysis," *Health Physics* **90**(2), pp. 154–160, 2006.

[81] Food and Drug Administration (FDA), "Safety Investigation of CT Brain Perfusion Scans." `http://www.fda.gov/MedicalDevices/Safety/AlertsandNotices/ucm185898.htm`, May 2011.

[82] J. J. DeMarco, C. H. Cagnon, D. D. Cody, D. M. Stevens, C. C. McCollough, M. Zankl, E. Angel, and M. F. McNitt-Gray, "Estimating radiation doses from multidetector CT using Monte Carlo simulations: effects of different size voxelized patient models on magnitudes of organ and effective dose," *Physics in Medicine and Biology* **57**, pp. 2583–2597, 2007.

[83] J. M. Boone, E. M. Geraghty, J. A. Seibert, and S. L. Wootton-Gorges, "Dose Reduction in Pediatric CT: A Rational Approach," *Radiology* **228**(2), pp. 352–360, 2003.

[84] T. R. C. Johnson, B. Krauß, M. Sedlmair, M. Grasruck, H. Bruder, D. Morhard, C. Fink, S. Weckbach, M. Lenhard, B. Schmidt, T. Flohr,

M. F. Reiser, and C. R. Becker, "Material differentiation by dual energy CT: initial experience," *European Radiology* **17**(6), pp. 1510–1517, 2006.

[85] M. M. Goodsitt, E. G. Christodoulou, and S. C. Larson, "Accuracies of the synthesized monochromatic CT numbers and effective atomic numbers obtained with a rapid kVp switching dual energy CT scanner," *Medical Physics* **38**(4), pp. 2222–2232, 2011.

[86] A. N. Primak, J. C. Ramirez Giraldo, X. Liu, L. Yu, and C. H. McCollough, "Improved dual-energy material discrimination for dual-source CT by means of additional spectral filtration," *Medical Physics* **36**(4), pp. 1359–1369, 2009.

[87] A. N. Primak, J. C. R. Giraldo, C. D. Eusemann, B. Schmidt, B. Kantor, J. G. Fletcher, and C. H. McCollough, "Dual-Source Dual-Energy CT With Additional Tin Filtration: Dose and Image Quality Evaluation in Phantoms and In Vivo," *American Journal of Roentgenology* **195**(5), pp. 1164–1174, 2010.

[88] R. G. Swensson, "Unified measurement of observer performance in detecting and localizing target objects on images," *Medical Physics* **23**, pp. 1709–1725, 1996.

[89] L. M. Popescu, "Nonparametric signal detectability evaluation using an exponential transformation of the FROC curve," *Medical Physics* **38**(10), pp. 5690–5702, 2011.

[90] S. Leng, L. Yu, L. Chen, J. C. R. Giraldo, and C. H. McCollough, "Correlation between model observer and human observer performance in CT imaging when lesion location is uncertain," in *Proceedings of SPIE - Medical Imaging 2012: Physics of Medical Imaging*, N. J. Pelc, E. Samei, and R. M. Nishikawa, eds., **8313**, pp. 83131M–1 – 83131M–7, SPIE, (San Diego, CA), 2012.

[91] International Commission on Radiological Protection, *ICRP Publication 103: The 2007 Recommendations of the International Commission on Radiological Protection*, vol. 37 of *Annals of the ICRP*, Elsevier, Oxford, UK, 200 7.

[92] L. M. Popescu and K. J. Myers, "CT image assessment by low contrast signal detectability evaluation with unknown signal location," The Second International Conference on Image Formation in X-Ray Computed Tomography, (Salt Lake City, Utah), 2012.

[93] L. M. Popescu and R. M. Lewitt, "Small nodule detectability evaluation using a generalized scan-statistic model," *Physics in Medicine and Biology* **51**, pp. 6225–6244, 2006.

[94] S. Gu, R. Gupta, and I. Kyprianou, "Computational high-resolution heart phantoms for medical imaging and dosimetry simulations," *Physics in Medicine and Biology* **56**(18), pp. 5845–5864, 2011.

[95] D. L. Parker, "Optimal short scan convolution reconstruction for fan beam CT," *Medical Physics* **9**(2), pp. 254–257, 1982.

[96] J. Hsieh, *Computed Tomography: Principles, Design, Artifacts, and Recent Advances*, SPIE Press, Bellingham, WA, 2003.

[97] M. H. K. Hoffmann, H. Shi, B. L. Schmitz, F. T. Schmid, M. Lieberknecht, R. Schulze, B. Ludwig, U. Kroschel, N. Jahnke, W. Haerer, H. J. Brambs, and A. J. Aschoff, "Noninvasive coronary angiography with multislice computed tomography," *Journal of the American Medical Association* **293**(20), pp. 2471–2478, 2005.

[98] K. Boedeker and M. McNitt-Gray, "Application of the noise power spectrum in modern diagnostic MDCT: part II. Noise power spectra and signal to noise," *Physics in Medicine and Biology* **52**, pp. 4027–4046, 2007.

[99] H. Q. Le, J. L. Ducote, and S. Molloi, "Radiation dose reduction using a CdZnTe-based computed tomography system: Comparison to flat-panel detectors," *Medical Physics* **37**(3), pp. 1225–1236, 2010.

[100] P. M. Shikhaliev, "The upper limits of the SNR in radiography and CT with polyenergetic x-rays," *Physics in Medicine and Biology* **55**(18), pp. 5317–5339, 2010.

[101] J. Schlomka, E. Roessl, and R. Dorscheid, "IOPscience - Experimental feasibility of multi-energy photon-counting K-edge imaging in pre-clinical computed tomography," *Physics in Medicine and Biology* **53**, 2008.

[102] E. Y. Sidky, L. Yu, X. Pan, Y. Zou, and M. Vannier, "A robust method of x-ray source spectrum estimation from transmission measurements: Demonstrated on computer simulated, scatter-free transmission data," *Journal of Applied Physics* **97**(12), pp. 124701–124701–11, 2005.

[103] J. Giersch, D. Niederlöhner, and G. Anton, "The influence of energy weighting on X-ray imaging quality," *Nuclear Instruments and Methods in Physics Research A* **531**(1-2), pp. 68–74, 2004.

[104] M. Tapiovaara and R. F. Wagner, "SNR and DQE analysis of broad spectrum X-ray imaging," *Physics in Medicine and Biology* **30**(6), pp. 519–529, 1985.

[105] P. M. Shikhaliev, "Computed tomography with energy-resolved detection: a feasibility study," *Physics in Medicine and Biology* **53**(5), pp. 1475–1495, 2008.

[106] H. Ding and S. Molloi, "Image-based spectral distortion correction for photon-counting x-ray detectors," *Medical Physics* **39**(4), p. 1864, 2012.

[107] T. G. Schmidt, "An empirical method for correcting the detector spectral response in energy-resolved CT," in *Medical Imaging 2012: Physics of Medical Imaging*, N. J. Pelc, R. M. Nishikawa, and B. R. Whiting, eds., *Proceedings of SPIE* **8313**, pp. 831312–1–831312–6, 2012.

[108] S. Srivastava, J. Cammin, G. S. K. Fung, B. M. W. Tsui, and K. Taguchi, "Spectral response compensation for photon-counting clinical x-ray CT using sinogram restoration," in *Medical Imaging 2012: Physics of Medical Imaging*, N. J. Pelc, R. M. Nishikawa, and B. R. Whiting, eds., *Proceedings of SPIE* **8313**, pp. 831311–1 – 831311–7, 2012.

[109] X. Wang, D. Meier, S. Mikkelsen, G. E. Maehlum, D. J. Wagenaar, B. M. W. Tsui, B. E. Patt, and E. C. Frey, "MicroCT with energy-resolved photon-counting detectors," *Physics in Medicine and Biology* **56**(9), pp. 2791–2816, 2011.

Appendix A

Code for Generating Scan Image

The following MATLAB code generates and writes to a file the auxiliary scan image required for calculating the scan-scores that are then used for estimating $\hat{A}_{FE}$.

```
% Author: Franco Rupcich
% Date: 18 December 2012
% Filename: create_scan_images.m
% Description: creates the auxiliary scan images used in
    calculating
% A_EFROC


%%% Test signal locations 6
% signal_loc = {[765 341], [728 441], [798 441], [830 381],
    [690 381]} for

% args:

% basename_image_noisy_signal_present
% basename_image_noisy_signal_absent
```

```
% nrows --> number of rows in image
% ncols --> number of cols in image
% nimgs --> number of images w/ signal (same as for w/o
    signal, so just use one arg)
% nitr --> number of iterations per image (how many times
    should we select an ROI from each image?)
% signal_loc --> center coord of each signal in entire image.
     This should be a cell array, where each cell is [x0_sig
    y0_sig];
% signal_diam --> diameter of each signal [cm]. We assume all
     signals are equal diameter (and contrast for that matter)
% varargin(1): roi_size --> default is 10 * signal_diam

%%% DeBuG - comment out function and use these to debug
% nrows_full_img = 1400;
% ncols_full_img = 1000;
% img_filename = '~/iq/roc/test_signal_locations/slices/
    test_signal_locations_6.0.slice';
% scan_img_filename = '~/iq/roc/scan/test_signal_locations_6.
    signal_present.0.scan';
% signal_radius = 0.05; %[cm]
% signal_search_bbox =[668.745967741936 321.266129032258
    208.51814516129 159.475806451613];   % ~21sqcm rectangle
    inside heart
% pixres = 0.025;
```

```
function z = create_scan_image(img_filename,
    scan_img_filename, nrows_full_img,ncols_full_img,
    signal_radius, signal_search_bbox, pixres)

% Check nargs
if (nargin ~= 7)

    fprintf(2,'\nError: At least 7 arguments required\n');
    fprintf(2,'1) img_filename --> filename of image to be
       scanned\n');
    fprintf(2,'2) scan_img_filename --> name of auxiliary
       scan image\n');
    fprintf(2,'3) nrows_full_img --> number of rows in image\
       n');
    fprintf(2,'4) ncols_full_img --> number of cols in image\
       n');
    fprintf(2,'5) signal_radius --> radius of signal [cm]\n')
       ;
    fprintf(2,'6) signal_search_bbox --> takes the form [xmin
        ymin width height]. Use imrect\n');
    fprintf(2,'7) pixres --> pixel resolution of image [cm]\n
       \n');

    return
end
```

```
%%% Takes the form [XMIN YMIN WIDTH HEIGHT]
xmin = round(signal_search_bbox(1));
ymin = round(signal_search_bbox(2));
xmax = xmin + round(signal_search_bbox(3));
ymax = ymin + round(signal_search_bbox(4));

nrows_roi = length(ymin:ymax);
ncols_roi = length(xmin:xmax);
npix_roi = nrows_roi * ncols_roi;

%%% NOTE: Signal template radius should be slightly larger
    than the
%%% signal radius. This is Rt in Popescu & Myers. We'll go
    with 1 pixel
%%% size larger (e.g., 0.025cm)
template_radius = (signal_radius + pixres)/pixres; % [pixels]

% auxiliary scan image
z = zeros(nrows_roi,ncols_roi);

% read in img
img  = loadReconSliceMu(img_filename,nrows_full_img,
    ncols_full_img);      % use mu values instead of HU, since
    we want only positive values
%img  = loadReconSliceHU(img_filename,nrows_full_img,
    ncols_full_img);      % try using HU values
img_roi = img(ymin:ymax,xmin:xmax);
```

```
% be careful to use cols first and rows second for meshgrid!
[xx yy] = meshgrid(1:ncols_roi,1:nrows_roi);

%%% scanning algorithm
for y0 = 1:nrows_roi
    for x0 = 1:ncols_roi

        C = sqrt( (xx - x0).^2 + (yy - y0).^2) <=
            template_radius;

        z(y0,x0) = sum(img_roi(C));

    end
end


%%% write scan-image to binary file
writeFloat(z,scan_img_filename);
```

Appendix B

Code for Generating Scan Scores

The following MATLAB code reads in scan images created using $create_scan_image.m$ and outputs a signal-present scan-score file, a signal-absent scan-score file, and a file containing other relevant information. These files are then read in by $calc_AefROC.c$ and used to calculate $\hat{A}_{FE}$.

```
% Author: Franco Rupcich
% Date: 19 December 2012
% Filename: read_scan_images_write_scan_scores.m
% Description: reads in a set of scan images (for signal
    present and signal
% absent images) and writes the corresponding scores.


%%% [x_coord y_coord]
%%% Coords w/r/t entire image: signal_loc = {[765 341], [728
    441], [798 441], [830 381], [690 381]}
%%% Coords w/r/t ROI above:    signal_loc = {[97 21], [162
    61], [129 121], [60 121], [22 61]}
```

```
%%% output
%%% X --> scan scores of true signals present
%%% Y --> scan scores of false positives
%%% I --> number of true signals present
%%% J --> number of false positives

%%%%%%%%%%%%%%%%%%%%%%%% DeBuG %%%%%%%%%%%%%%%%%%%%%%

% scan_image_signal_present_basename = '~/iq/roc/scan/
    ella_chest_hb_contrast5x4mm3.25mgmL_120kvp_1.5e9photons';
% scan_image_signal_absent_basename = '~/iq/roc/scan/
    ella_chest_hb_nocontrast_120kvp_1.5e9photons';
%
% nimgs = 1;
% nrows=160;
% ncols=210;
% pixres = 0.025; % [cm]
% signal_radius = 0.2; %[cm]
% signal_loc = {[97 21], [162 61], [129 121], [60 121], [22
    61]};
% z0 = 56.53;
%
% search_area = 21;



%%% z0 values for 1mm signal
%% z0 = 6.60 --> 15 false positives for 1.5e9 photons
```

```
%% z0 = 6.60 --> 127 false positives for 7.0e8 photons
%% z0 = 6.67 --> 11 false positives for 7.0e8 photons
%% z0 = 6.63; --> 55 false positives for 7.0e8 (use this per
    Lucretiu)

%%% z0 values for 4mm signal
%% z0 = 56.63; 34 false positives for 1.0e9 photons
%% z0 = 56.53; 50 false positives for 1.6e9 photons

%%%%%%%%%% END DEBUG
   %%%%%%%%%%%%%%%%%%%%%%%%%%%%%%%%%%%%%%%%%%%%%%%%%%%%

function read_scan_images_write_scan_scores(
   scan_image_signal_present_basename,
   scan_image_signal_absent_basename, output_base_fn, nimgs,
   nrows, ncols,pixres, signal_radius,signal_loc,z0,
   search_area)

% Check nargs
if (nargin ~= 11)

    fprintf(2,'\nError: 11 input args required\n');
    fprintf(2,'1) scan_image_signal_present_basename --> base
        filename of signal-present scan image (e.g.,
       ella_contrast_120kvp). The function will automatically
        append .scan\n');
```

```
    fprintf(2,'2) scan_image_signal_absent_basename --> base
       filename of signal-absent scan image (e.g.,
       ella_nocontrast_120kvp). The function will
       automatically append .scan\n');
    fprintf(2,'3) output_base_fn --> base filename of files
       that will contain scan scores\n');
    fprintf(2,'4) nimgs --> number of scan images\n');
    fprintf(2,'5) nrows --> nrows in image\n');
    fprintf(2,'6) ncols --> ncols in image\n');
    fprintf(2,'7) pixres --> pixel resolution [cm]\n');
    fprintf(2,'8) signal_radius --> radius of signal [cm] \n
       ');
    fprintf(2,'9) signal_loc -->center coords of each signal
       in ROI. Should be cell array, where each cell is [
       x0_sig y0_sig]. Use loadReconSlice() to find
       coordinates.\n');
    fprintf(2,'10) z0 --> stopping limit for recording local
       maxima\n');
    fprintf(2,'11) search_area --> area of search region of
       one image [cm^2] \n');


    return
end
```

```
%%% initialize scan-score vectors. Their size will change
    later
X = -99999*ones(nimgs*length(signal_loc),1);
Y = -99999*ones(1e6,1);

%%% index into X and Y vectors
x_ind = 1;
y_ind = 1;


%%% mask radius is twice that of signal
mask_radius_pix =  (signal_radius * 2)/pixres;  % [pixels]

%%% mask radius is a few pixels larger than signal radius
%mask_radius_pix =  signal_radius/pixres + 2;  % [pixels]

% be careful to use cols first and rows second for meshgrid!
[xx yy] = meshgrid(1:ncols,1:nrows);


for i = 0:(nimgs - 1)


    %%%%%%%%%%%%%%%% signal-present scan image
       %%%%%%%%%%%%%%%%%%%%%%%%%%
    fn = strcat(scan_image_signal_present_basename,'.',
       num2str(i),'.scan');
```

```
    z  = readFloat(fn,nrows,ncols);

    %%%% for signal present images, just score the true
        signals, don't search
     for j = 1:length(signal_loc)

         x_sig = signal_loc{j}(1);
         y_sig = signal_loc{j}(2);
         X(x_ind) = z(y_sig,x_sig);
         x_ind = x_ind + 1;

%          %%% DeBuG - create mask over signals %%%
%          C = sqrt( (xx - x_sig).^2 + (yy - y_sig).^2) <=
   mask_radius_pix;
%          z(C) = 0;
%          %%% end debug %%%

     end

%      %%% debug %%%
%      figure; imagesc(z); axis image;
%      %%% end debug %%%

%%%% The commented out code searches for the maxima
%     %%% Find only the first max
%     [y_local_max, x_local_max] = find(z==max(z(:)),1,'first
   ');
```

```
%     local_max = z(y_local_max,x_local_max);
%
%     %%% keep going while max is greater than z0
%     while( local_max > z0 )
%
%         % check if this is a true signal location
%         for j = 1:length(signal_loc)
%
%             x_sig = signal_loc{j}(1);
%             y_sig = signal_loc{j}(2);
%             r = sqrt( (x_sig -x_local_max)^2 + (y_sig -
    y_local_max)^2);   % distance between true signal and
    located signal [pixels]
%
%             % if distance between true sig and locate sig
    is within one
%             % signal radius of the signal center, than
    count it as a
%             % correctly located signal and add the scan-
    score to X vector
%             if r <= signal_radius_pix
%                 X(x_ind) = local_max;
%                 x_ind = x_ind+1;
%                 break;
%             else
%                 % do nothing - we don't care about the
    false positives from
```

```
%                 % signal-present images.
%             end
%
%         end
%
%
%         %%% mask pixels within double the signal radius
   around this point
%         C = sqrt( (xx - x_local_max).^2 + (yy - y_local_max
   ).^2) <= mask_radius_pix;
%         z(C) = 0;
%
%         %%% find next maximum
%         [y_local_max, x_local_max] = find(z==max(z(:)),1,'
   first');
%         local_max = z(y_local_max,x_local_max);
%
%     end
%
%     %%% debug %%%
%     figure; imagesc(z); axis image;
%     %%% end debug %%%


    %%%%%%%%%%%%%%%%%% signal-absent scan image
        %%%%%%%%%%%%%%%%%%%%%%%%%%
```

```
    fn = strcat(scan_image_signal_absent_basename,'.',num2str
        (i),'.scan');
    z  = readFloat(fn,nrows,ncols);

%     %%% debug %%%
%      figure; imagesc(z); axis image;
%     %%% end debug %%%

    %%% Find only the first max
    [y_local_max, x_local_max] = find(z==max(z(:)),1,'first')
        ;
    local_max = z(y_local_max,x_local_max);

    %%% keep going while max is greater than z0
    while( local_max > z0 )

        Y(y_ind) = local_max;
        y_ind = y_ind+1;

    %%% mask pixels within double the signal radius around
        this point
    C = sqrt( (xx - x_local_max).^2 + (yy - y_local_max).^2)
        <= mask_radius_pix;
    z(C) = 0;

    %%% find next maximum
```

```
    [y_local_max, x_local_max] = find(z==max(z(:)),1,'first')
        ;
    local_max = z(y_local_max,x_local_max);

    end

end

%%% debug %%%
% figure; imagesc(z); axis image;
%%% end debug %%%

%%% reshape X and Y vectors using X = X(X~=-99999);
X = X(X~=-99999);
Y = Y(Y~=-99999);

I = length(X);
J = length(Y);
omega_t = search_area * nimgs;

%%% write INJO file (I, nimgs, J, and omega_t)
fn = strcat(output_base_fn,'.injo');
fid = fopen(fn,'w');
fprintf(fid,'%d\t%d\t%d\t%f',I,nimgs,J,omega_t);
fclose(fid);

%%% write scan score files (.sscr == scan score)
```

```
fn = strcat(output_base_fn,'.signal_present.sscr');
fid = fopen(fn,'w');

for i = 1:I
    fprintf(fid,'%.6f\n',X(i));
end
fclose (fid);

fn = strcat(output_base_fn,'.signal_absent.sscr');
fid = fopen(fn,'w');

for j = 1:J
    fprintf(fid,'%.6f\n',Y(j));
end
fclose (fid);
```

Appendix C

Code for Calculating $\hat{A}_{FE}$

The following C code calculates the AUC EFROC estimator, $\hat{A}_{FE}$ and its variance, based on the signal-present and signal-absent scan-score files output by $read_scan_images_write_scan_scores.m$.

```
/*********************************************
* Author: Franco Rupcich
* Filename: calc_Aefroc.c
* Last Modified: 12/19/12
* Description: calculates estimate for A_EFROC and its
   variance. See Popescu paper "Nonparametric ROC and LROC
   analysis"
*
*****************************************************************



/* input args */

// 1) signal_present_scan_scores_filename --> name of file
   containing Xi (scan scores for true positivies)
```

```
// 2) signal_absent_scan_scores_filename --> name of file
   containing Yj (scan scores for false positives)

// 3) injo_filename --> name of file containing the variables
    I (total # true signals present), J
//    (total # false positives), n (# signal absent images),
   and O (total area scanned for a single image)

// 4) out_filename --> name of output file containing
   estimate for A_EFROC and its variance


/* Standard includes */
#include <stdio.h>
#include <stdlib.h>
#include <string.h>
#include <math.h>


/* Function Prototypes */
int readINJOFile(FILE *,int *, int *, int *, float *);
int readScanScoreFile(FILE *, float *, int);
float heaviside(float);
float calcS11(int, float, int, float *, float *, float);
float calcS12(int, float, int, float *, float *, float);
```

```
float calcS21(int, float, int, float *, float *, float, float
   );
float calcA(int, float, int, float *, float *);

/**
* Main Function
**/

int main(int argc, char **argv)
{

    char  *signal_present_scan_scores_filename; /* name of
       file containing signal-present scan scores, Xi
            */
    char  *signal_absent_scan_scores_filename;  /* name of
       file containing signal-absent scan scores, Yj
            */
    char  *injo_filename;                       /* name of
       file containing I,N,J, and Omega_total
            */
    char  *out_filename;                        /* name of
       output file containing A_EFROC and standard deviation
            */

    float S11, S12, S21;        /* variables used to
       calculate error bar (see Popescu paper) */
```

```
float c1,c2,c3;              /* variables used to
   calculate error bar (see Popescu paper) */
float ebar;                  /* error bar (one standard
   deviation)   */
float A;                     /* area under EFROC curve
                  */

/* pointers to I, N, J, and Omega */
int *ptrI = (int *) malloc(sizeof(int));          /*
   pointer to total number true signals present */
int *ptrn = (int *) malloc(sizeof(int));          /*
   pointer to number of signal absent images    */
int *ptrJ = (int *) malloc(sizeof(int));          /*
   pointer to number of false positives         */
float *ptrO = (float *) malloc(sizeof(float));    /*
   pointer to total scanned area                */

float omega_total;           /* total area scanned (for
   all images combined) [cm^2]  */
float omega_ref;             /* reference area scanned (
   for a single image), used to scale EFROC to desired
   search area [cm^2]        */
int I,n,J;

float N;                     /* N = omega_t/omega_ref */

int RC;                      /* Return Code */
```

```
/* Read args         */
if (argc != 6)
{

    fprintf(stderr,"\nERROR in %s: 5 args required!",argv
       [0]);
    fprintf(stderr,"\n1)
       signal_present_scan_scores_filename --> name of
       file containing Xi");
    fprintf(stderr,"\n2)
       signal_absent_scan_scores_filename --> name of
       file containing Yj");
    fprintf(stderr,"\n3) injo_filename --> name of file
       containing I,N,J, and omega_total");
    fprintf(stderr,"\n4) out_filename --> name of output
       file containing A_EFROC and standard deviation");
    fprintf(stderr,"\n5) omega_ref --> reference area (
       for a single image) [cm^2]. NOTE: To scale A_EFROC
        to A_LROC results, use omega_ref = twice the area
        of an ROI from the LROC study (e.g., if ROI is
       1.5625 cm^2, use 3.125 cm^2)\n\n");

    return 1;
}

else
```

```
    {
        signal_present_scan_scores_filename      = argv[1];
        signal_absent_scan_scores_filename       = argv[2];
        injo_filename                            = argv[3];
        out_filename                             = argv[4];
        omega_ref                                = atof(argv
            [5]);
    }

    // Read in I,N,J,O
    FILE *fp_injo = fopen(injo_filename,"r");

    RC = readINJOFile(fp_injo, ptrI, ptrn, ptrJ, ptrO);

    I = *ptrI;  free(ptrI);
    n = *ptrn;  free(ptrn);
    J = *ptrJ;  free(ptrJ);

    omega_total = *ptrO; free(ptrO);

//     fprintf(stdout,"\n\n I: %d, N: %d, J: %d, O: %f\n",I,N,
   J,omega_total);

    if ( RC != 0)
    {
        fprintf(stderr,"\n\nERROR reading from %s\n",
            injo_filename);
```

```
    return 2;
}

fclose(fp_injo);

N = omega_total/omega_ref;

// Read in x and y
float *x = (float *)malloc(I * sizeof(float));
float *y = (float *)malloc(J * sizeof(float));


FILE *fp_xss = fopen(signal_present_scan_scores_filename
   ,"r");
RC = readScanScoreFile(fp_xss,x,I);

if ( RC != 0)
{
    fprintf(stderr,"\n\nERROR reading from %s\n",
       signal_present_scan_scores_filename);
    return 3;
}

fclose(fp_xss);
```

```
    FILE *fp_yss = fopen(signal_absent_scan_scores_filename,"
       r");

    RC = readScanScoreFile(fp_yss,y,J);

    if ( RC != 0)
    {
        fprintf(stderr,"\n\nERROR reading from %s\n",
           signal_absent_scan_scores_filename);
        return 3;
    }

    fclose(fp_yss);
/*
    // DeBuG - print values
    int dirka;
    for (dirka=0; dirka<J; dirka++)
    {
        fprintf(stdout,"\ny[%d]: %f",dirka,y[dirka]);
    }
*/

    // calculate c terms from Popescu paper
    c1 = N * ( 1.0 - exp(-1.0/N) );
    c2 = (N/2.0) * ( 1.0 - exp(-2.0/N) );
    c3 = N * ( exp(-1.0/N) - exp(-2.0/N) );
```

```
    // calculate S terms from Popescu paper
    S11 = calcS11(I, N, J, x, y, c1);
    S12 = calcS12(I, N, J, x, y, c2);
    S21 = calcS21(I, N, J, x, y, c1, c3);

    // calculate A
    A = calcA(I, N, J, x, y);

    // calculate error bar (standar deviation of A)
    ebar = sqrt( S12*(1.0/I) + S21*( (I-1.0)/I) - (S11 * S11)
        );

/*
    // DeBuG code - print out some values
    float var;
    var = ( S12*(1.0/I) + S21*( (I-1.0)/I) - (S11 * S11) );
    fprintf(stdout,"\n\nA: %f\n", A);
    fprintf(stdout,"ebar: %f\n",ebar);
    fprintf(stdout,"I: %d\nN: %f\nJ: %d\nO: %f\n",I,N,J,
       omega_ref);
    fprintf(stdout,"c1: %f\nc2: %f\nc3: %f\n",c1,c2,c3);
    fprintf(stdout,"S11: %f\nS12: %f\nS21: %f\n",S11,S12,S21)
       ;
    fprintf(stdout,"var: %f\n",var);
    fprintf(stdout,"1/I*S12: %f\n",(1.0/I)*S12);
    fprintf(stdout,"I-1/I * S21: %f\n", S21* ( (I-1.0)/I));
    fprintf(stdout,"S11^2: %f\n\n",S11 * S11);
```

```
*/

    // output error bar (standard deviation) to file
    FILE *fp_out = fopen(out_filename,"w");
    fprintf(fp_out,"%f\t%f",A,ebar);
    fclose(fp_out);

    // free allocated memory
    free(x);
    free(y);

}

/**
 * Reads a column of scan scores from file
 *
 * @param fp
 * A file pointer to the input file
 *
 * @param buffer
 * A pointer to the buffer that will hold max-scan values for
     signal present images
 *
 * @param n
 * Number of data points in file
 *
 * @return
```

```
 * Returns 0 upon success
 */
int readScanScoreFile(FILE *fp, float *buffer, int n)
{

    if (fp == (FILE *) NULL)
    {
        return 1;
    }

    int i;

    /* read in values */

    while ( fscanf(fp,"%f",&buffer[i]) != EOF )
    {
        i++;
    }

    if (i != n)
    {
        fprintf(stderr,"ERROR: Expected %d data points in
            file but read %d\n",n,i);
        return 2;
    }

/*
```

```
    for (i=0; i<n; i++)
    {
        fscanf(fp,"%f",&buffer[i]);
    }
*/
    return 0;
}



/**
 * Reads I,N,J, and Omega_total from fiel
 *
 * @param fp
 * A file pointer to the input file
 *
 * @param ptrI
 * A pointer to the buffer that will hold the number of true
    signals present scores
 *
 * @param ptrn
 * A pointer to the buffer that will hold the number of
    signal absent images
 *
 * @param ptrJ
 * A pointer to the buffer that will hold the number of false
     positive scores
 *
```

```
 * @param ptrO
 * A pointer to the buffer that will hold the total area
    scanned (for a single image)
 *
 * @return
 * Returns 0 upon success
 */

int readINJOFile(FILE *fp, int *ptrI, int *ptrn, int *ptrJ,
   float *ptrO)
{

    if (fp == (FILE *) NULL)
    {
        return 1;
    }

    fscanf(fp,"%d%d%d%f",&ptrI[0],&ptrn[0],&ptrJ[0],&ptrO[0])
       ;

    return 0;
}

/**
* The heaviside function. Reads in a value and returns
   heaviside(z)
*
```

```
* @param z
* Value to return heaviside fn for
*
* @return
* returns H = H(z)
**/
float heaviside(float z)
{

    float h;

    if ( z > 0)
    {
        h=1.0;
    }
    else if ( z == 0)
    {
        h=0.5;
    }
    else // z<0
    {
        h=0.0;
    }

    return h;

}
```

```
/**
* Calculates S11 (see Popescu paper)
*
*/
float calcS11(int I, float N, int J, float *x, float *y,
   float c1)
{

    float H;
    float S11;
    double inner_sum;
    double outer_sum = 0;

    int i,j;

    for (i=0; i<I; i++)
    {
        inner_sum = 0;

        for (j=0; j<J; j++)
        {
            H = heaviside(y[j] - x[i]);
            inner_sum = inner_sum + H*c1;
        }

        outer_sum = outer_sum + exp( (-1.0/N) * inner_sum);
```

```
    }

    S11 = outer_sum * ( 1.0/I );

    return S11;

}

/**
* Calculates S12 (see Popescu paper)
*
*/
float calcS12(int I, float N, int J, float *x, float *y,
   float c2)
{

    float H;
    float S12;
    double inner_sum;
    double outer_sum = 0;

    int i,j;

    for (i=0; i<I; i++)
    {
        inner_sum = 0;
        for (j=0; j<J; j++)
```

```
        {
                H = heaviside(y[j] - x[i]);
                inner_sum = inner_sum + H*c2;
        }

        outer_sum = outer_sum + exp( (-2.0/N) * inner_sum);

    }

    S12 = outer_sum * (1.0/I );

    return S12;

}

/**
* Calculates S21 (see Popescu paper)
*
*/
float calcS21(int I, float N, int J, float *x, float *y,
   float c1, float c3)
{

    float H1,H2;
    float S21;
    double outer_sum1 = 0;
    double outer_sum2 = 0;
```

```
double inner_sum1, inner_sum2;

int i1, i2, j;

for (i1=0; i1<I; i1++)
{
    for (i2=0; i2<I; i2++)
    {
        inner_sum1 = 0;
        if (x[i1] >= x[i2] )
        {
            for (j=0; j<J; j++)
            {

                H1 = heaviside(y[j] - x[i1]);
                H2 = heaviside(y[j] - x[i2]);

                inner_sum1 = inner_sum1 + H1*c3 + H2*c1;
            }

            outer_sum1 = outer_sum1 + exp( (-1.0/N) *
               inner_sum1);
        }

    }
}
```

```
    for (i1=0; i1<I; i1++)
    {
        for (i2=0; i2<I; i2++)
        {
            inner_sum2 = 0;
            if (x[i1] < x[i2] )
            {
                for (j=0; j<J; j++)
                {
                    H1 = heaviside(y[j] - x[i1]);
                    H2 = heaviside(y[j] - x[i2]);

                    inner_sum2 = inner_sum2 + H1*c1 + H2*c3;
                }
                outer_sum2 = outer_sum2 + exp( (-1.0/N) *
                   inner_sum2);
            }

        }
    }


    S21 = (1.0/(I*I)) * outer_sum1 + (1.0/(I*I)) * outer_sum2
       ;

    return S21;
}
```

```
/*******
* Calculates A, the area under EFROC curve. (See Popescu)
*
*/

float calcA(int I, float N, int J, float *x, float *y)
{

    float H;
    float A;
    double inner_sum;
    double outer_sum = 0;

    int i,j;

    for (i=0; i<I; i++)
    {
        inner_sum = 0;

        for (j=0; j<J; j++)
        {
            H = heaviside(y[j] - x[i]);
            inner_sum = inner_sum + H;
        }

        outer_sum = outer_sum + exp( (-1.0/N) * inner_sum);
```

```
        }

        A = (1.0/I) * outer_sum;

        return A;
    }
```